Summer 8-11-2015

From Copper Zinc Tin Sulfur to Perovskites: Fabrication and Characterization of New Generation of Solar Cells

Sarah Wozny
University of New Orleans, woznysarah@hotmail.fr

From Copper Zinc Tin Sulfur to Perovskites: Fabrication and Characterization of New Generation of Solar Cells

A Dissertation

Submitted to the Graduate Faculty of the
University of New Orleans
in partial fulfillment of the
requirements for the degree of

Doctor of Philosophy
in
Chemistry

by

Sarah Wozny

D.U.T. Université de Poitiers, 2009
B.S. Heriot-Watt University, 2010
M.S. University of New Orleans, 2014

August 2015

“À ma famille”

Acknowledgements

I would like to first and foremost express my gratitude and appreciation to my family.

To my parents, Fredou and Moumine, for their love and unconditional support along this journey. For always believing in me and helping me to reach my goals. “À mes parents, Fredou et Moumine, pour leur amour et support inconditionnel pendant ce voyage. Pour toujours croire en moi et m’aider à atteindre mes objectifs.”

To my sister, Anne-Sophie (boubou), for always being present, motivating me and helping me through the good and difficult times. For waking up an hour earlier every day to drive me to school, for correcting my French, doing my high school homework, and simply for taking such good care of me. “À ma sœur, Anne-Sophie, pour toujours avoir été présente, m’avoir motivée et aidée dans les bons, comme mauvais moments. Pour s’être réveillée une heure plus tôt tous les jours, pour me conduire à l’école, pour corriger mon français, faire mes devoirs et tout simplement pour avoir pris soins de moi.”

To my grandparents, Alphonse and Huguette, for their love and their almost punctual Sunday morning phone calls. “À mes grand-parents, Alphonse et Huguette, pour leur amour et presque ponctuelle appel téléphonique du Dimanche matin.”

To my uncle Jean-Marie, thank you for your kindness.

To my second family, Christine, Patrice, Paul and Sébastien Estrade, thank you for the yearly dinners and sweet treats. “À ma seconde famille, Christine, Patrice, Paul et Sébastien Estrade, merci pour les dîners annuels et les tartes pomme-praline.”

Thank you for your support, no words can express my gratitude and tell you how much I love you. “Merci pour votre support, il n’y a pas de mot pour exprimer ma gratitude et combien je vous aimes.”

To Arjun Sharma, thank you for spending all of these years with me, being able to bear my changing moods, cheering me up and always caring about me.

To Shiva Adireddy, thank you for convincing me to do PhD and helping me to get into the program, for your moral support and tremendous help along this journey..

I gratefully thank my advisor, Dr. Weilie Zhou, who gave me the opportunity to come to UNO for graduate studies and for always knowing how to push me beyond my limits, in order to get the most of my aptitudes.

I wish also to express my gratitude to my committee members, Dr. Leszek Malkinski, Dr. Mark Trudell and Dr. John Wiley, for their helpful discussions and their availability when I needed advice. I would also like to express my sincere thank you to Dr. Leonard Spinu, Poncho De Leon and Jennifer Tickle their financial and moral support and for their kindness as well.

I gratefully acknowledge my officemates: Dr. Kai Wang, for being the kindest and hardest working person. You are a real mentor and friend. Dr. Hui Ma and Satish Rai, you made my days at AMRI brighter, and I am glad to have you as my friends.

I would like to extend my appreciation to my past and current group members: Dr. Jiajun Chen, Dr. Baobao Cao, Dr. Kun Yao, Dr. Haiqiao Su, Nooraldeen Alkurd, Zhi Zheng, Shuke Yan for their help and kindness, and for those wonderful tea times. It is a pleasure to express my appreciation to my friends in AMRI and the Chemistry department: Parisa Pirani, John Gaffney, Nicolas Vargas, Kirsten Williams, Richie Prevost, Maria Lindsey, Dr. Elisha Josepha and last, but not least Léa Gustin. Léa, thank you for being my friend for the last 8 years, through the many countries we travelled and lived in together.

I would like to express my deep gratitude to my friends Marion Gay, Aurélien Rivière, Laurent Jouanine, Damien Tardieu, and Clement Sanchez for their great friendship. I always look forward to the rare Skype conversations and great weekends we spend together.

I would like to acknowledge the people at NREL who made my stay in Colorado amazing. Dr. Mengjin Yang, Dr. Helio Moutinho, Dr. Candy Mercado, Dr. Harvey Guthrey, and Dr. Alexandre Nardes, thank you for helping me in the device and characterization lab. Dr. Alexandra Dubini, Dr. Melissa Cano and Shuting Zhang, thank you for giving me shelter and for those wonderful days spent together.

An immense thank you also goes to Dr. Jeffery Aguiar for making this *in-situ* project a reality. No words can express how deeply I am grateful for your daily help and kindness, for all those trips you made to make our project a success, and for all the great people you introduce me to.

I also want to thank my NREL mentor, Dr. Mowafak Al-Jassim, who supported my project and offered me the chance to come back working at NREL. Finally, I would like to record my greatest gratitude to my NREL advisor Dr. Kai Zhu, who made my time at NREL one of the best. In this last year, Dr. Zhu helped me to reach my goals and mature in my PhD work, with his endless kindness toward me, and his continuous encouragement, help, valuable guidance and respect.

Table of Contents

List of Figures

List of Tables

Abstract

In 2013, the worldwide production of renewable electricity accounted for 22.1% of the total energy production with 0.9% coming from solar photovoltaics (PVs). Recently, there has been a growing interest for Cu_2ZnSnS_4 (CZTS) quaternary semiconductor due to the abundance and low cost of its precursors. Moreover, this chalcopyrite material has an ideal direct band gap around 1.5 eV, high absorption coefficient ($\alpha > 10^4$ cm^{-1}) and high conductivity, making it suitable for nanostructured and dye-sensitized solar cell (DSSC) applications. Here, CZTS nanoparticles have been synthesized by pulsed laser deposition (PLD) and simultaneously deposited in the interstitial space of ZnO nanowire arrays to form bulk heterojunction 3D nanostructured solar cells. Secondly, vertically oriented CZTS nanoplates have been synthesized by PLD and used as counter electrode in platinum-free dye-sensitized solar cells. These CZTS nanostructures proved to be suitable in achieving workable solar cells, which could significantly cut down the cell cost and provide environmentally friendly photovoltaic devices. Alternately, hybrid organic–inorganic perovskite solar cells have become one of the most attractive photovoltaic technologies with easy solution fabrication and high conversion efficiencies. However, the devices remain unstable under certain processing and environmental conditions. Herein, formamidinium lead tri-halide perovskite ($FAPbI_3$) planar heterojunction solar cells have been fabricated under a controlled environment. The fabrication parameters (precursor concentration, annealing, etc) and the effect of humidity on the structural, optical, and electrical properties of $FAPbI_3$ thin films and devices have been investigated and proved to be critical in the processing of efficient devices. Solar cells with conversion efficiency of 16.6% have been obtained. Furthermore, *in-situ* techniques such as *in-situ* (scanning) transmission electron microscopy and *in-situ* XRD were performed to understand the crystallization and degradation

mechanisms of $FAPbI_3$ thin films. The *in-situ* data were correlated with planar heterojunction $FAPbI_3$ devices efficiency data in order to improve the device fabrication process.

Keywords: solar cells, nanomaterials, emerging absorber material, cooper zinc tin sulfur, perovskite, synthesis, characterization, *in-situ*, high efficiency.

Chapter 1 Introduction and background

1.1 Renewable energy

With the energy crisis of the 21st century and a constantly increasing energy demand, a sustainable energy production is one of the most important issues for the preservation of our planet. Currently, our society relies heavily on the use of fossils fuel (80%) for its energy production.[1,2] However, the power supply acquired from fossil fuel remains low compared to the release of carbon dioxide in the atmosphere, which engenders greenhouse effect.[3-5] In addition to the greenhouse effect, fossil fuel resources will also be depleted in the near future because of their limited amount.[5,6] Renewable energies are the key in achieving a sustainable energy society. They are generally defined as energy that comes from naturally replenishing resources in a human timescale.[7]

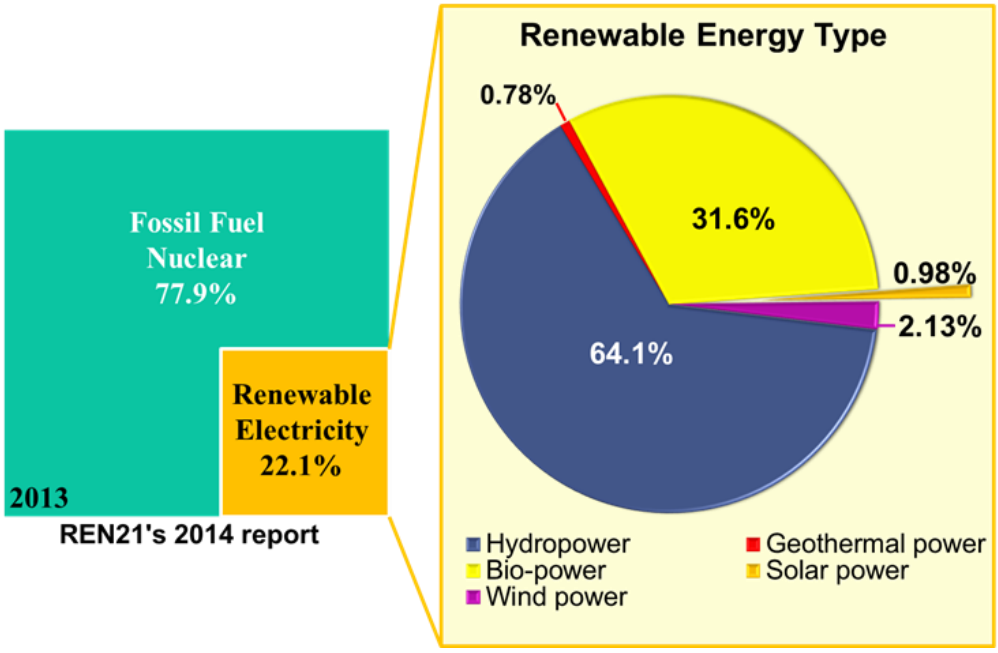

Figure 1. 1. Worldwide energy production adapted from REN21's 2014 report.

In 2013, the worldwide production of renewable electricity accounted for 22.1% of the total energy production. The renewable electricity was produced from hydropower (16.4%), wind (2.9%), bio-power (1.8%), solar photovoltaic (0.7%) and geothermal (0.4%) methods.[8] Figure 1.1 is a schematic summarizing the different type of energy production.[8] The advantages of renewable energies rely on

(i) their abundance,[7-9]

(ii) and their presence over wide geographical areas. Other energy sources are concentrated in a limited number of countries.[8,9]

(iii) Renewable energies are clean energy sources, resulting in no contribution to the greenhouse effect through environmental pollution.[4,9,10]

1.2 Solar cells

Among renewable energies, solar energy is of particular interest due to its abundance, geographic availability and environmentally friendly nature. Solar cells also known as photovoltaic cells are devices that convert the energy from sun light into electrical energy. Currently, solar energy production accounts for less than 1% of the total energy production, however, photovoltaics market attracted significant investments (53%) for clean energy production.[6,8] The large investment relies on clean and low-cost energy production in solar cells. To achieve these goals, an effort needs to be focused on using lower cost and more abundant materials, decreasing the overall production cost and increasing the energy pay-back time.[11,12] So far, solar cells have been divided in to four generations:[12]

(i) The first generation is based on "crystalline silicon" (c-Si).[13-17] This includes cells made of silicon or germanium which are doped with elements such as phosphorus or boron to

form *pn*- junctions. Crystalline silicon semiconducting wafers currently dominate the commercial market (15%–21% efficiency), thanks to the absorber material (Silicon) which can be integrated into green, efficient, and extremely reliable solar cells. However, this technology requires the use of thick and brittle wafers which necessitate expensive manufacturing processes making their price comparatively higher to their power output. [13-17]

(ii) The second generation of solar cells is based on "thin film technology"[11] such as cadmium telluride (CdTe),[18-24] copper indium gallium diselenide (CIGS)[25-30] and hydrogenated amorphous silicon (a-Si:H).[31-36] These types of absorber materials show 10-100 times enhanced light absorption compared to c-Si light absorption and thus require less material consumption and ultimately decreasing the cost. However, these solar cells have demonstrated low efficiencies (12%–15%) due to the complexity of their stoichiometry or sensitivity to moisture and oxygen. Further, commercial development will be hindered by the scarcity and toxicity of precursor materials such as indium and cadmium.

(iii) The third generation of solar cells relies on "multi-junction" solar cells.[37-41] These cells demonstrate record efficiency at laboratory scale (46%). However, their development at the industrial scale will be limited by their elevated cost and complicated manufacturing process.

(iv) The fourth generation of solar cells, referred to as "emerging photovoltaics" is built on several technologies such as nanostructures instead of bulk material. They include nanocrystal solar cells,[42-45] dye sensitized solar cells,[46-49] polymer solar cells,[50-54] inorganic solar cells,[55-59] perovskite solar cells,[60-64] and others. The main advantages are the low cost of the precursor materials which can be solution processed for industrial applications, and their environmentally friendly composition. However their efficiency remains low compared to the first and second generation of solar cell devices.

1.2.1 Fundamentals of solar cells

Most of the solar cells depend on semiconductor material. Upon illumination, electron-hole pairs are generated in the semiconductor materials. When a load is applied to the device, the charge carriers can move and electricity can be produce. General working process of solar cell will be discussed below.

1.2.2 Semiconductor materials

A semiconductor material is defined by its conductivity which value is between that of a non-conductive insulator and highly conductive metals either due to the addition of an impurity or because of temperature effects.[65,67] The addition of impurity is referred to as doping with *n*- and *p*-type semiconductor doping as shown in Figure 1.2.

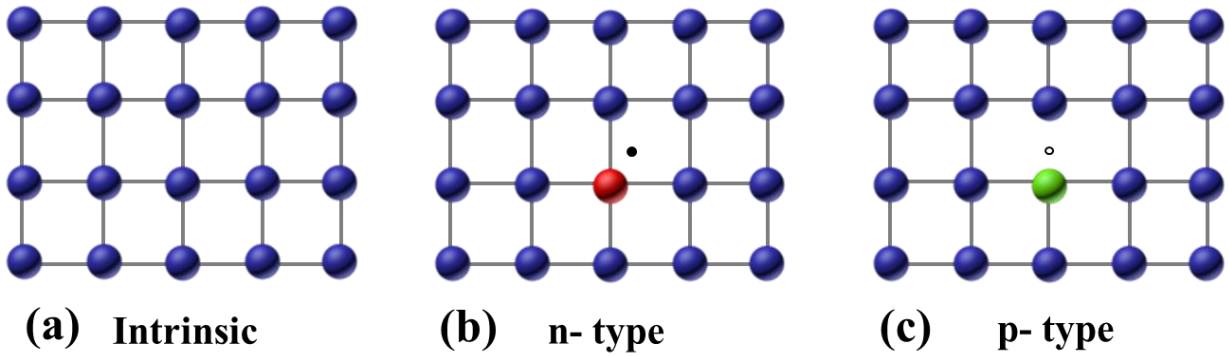

Figure 1. 2. Schematic of an (a) intrinsic, (b) *n*-type and (c) *p*-type semiconductor material. Tetravalent silicon (blue balls) was used as a model. The red and green balls represent pentavalent and trivalent atoms, respectively.

To illustrate this concept, tetravalent silicon with four bonding sites is used. In the case of *n*-type doping (Figure 1.2b), the silicon crystal is replaced by a pentavalent atom, resulting in an electron which cannot form a covalent bond. The electron is then easily removed from the atoms.

In the case of *p*-type doping (Figure 1.2c), silicon is replace by a trivalent atom, leading to a hole formation because of the missing electron. This material is considered as an acceptor. When no doping is carried out, the semiconductor material is considered "intrinsic".[67]

1.2.3 *pn*-junction

A crystal is defined as an interconnected sequence of unit cells leading to a formation of bands.[66] The conduction and valence bands are the most relevant in semiconductor materials and are defined as the highest and lowest band above and below the fermi level, respectively. The distance between these two bands is defined as the band gap (Eg) and has values in the energy range from 0.5 to 4eV for semiconductor materials. For *n*-type doping, electrons are the majority charge carriers and located mainly in the conduction band while holes are majority carriers for *p*-type materials in the valence band. The position of the fermi level depends on the nature of the semiconductor material. When *n*- and *p*-type materials are connected, a *pn*-junction is formed as shown in Figure 1.3. The Fermi level of each doped materials will align themselves, inducing a band bending at the interface between the two materials.

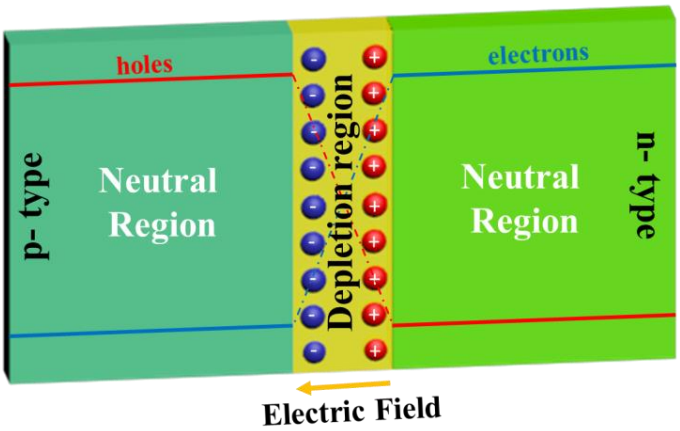

Figure 1. 3. Formation of depletion region by contact between *p*- and *n*-type semiconductor materials.

Upon contact, charge carriers start diffusing electrons toward the *p*-type and holes toward the *n*-type, thus creating a depletion region at the interface between the two semiconductor materials.

1.2.4 *pn*-junction under bias

When a bias (forward or reverse) is applied to a *pn*-junction, the electric field at the depletion region is modified. Forward bias refers to a positive voltage applied to the *p*-type and negative voltage to the *n*-type and vice versa for the reverse bias. With forward bias, the electric field applied to the device is opposite and higher than the one in the depletion region.[67] As a consequence, the electric field drops in the depletion region, leading to a reduced barrier for the charge carriers to overcome and diffuse from one side to the other as presented in Figure 1.4. With reverse bias, the electric field applied to the device is in the same direction as the one in the depletion region. As a consequence, the electric field is increased in the depletion region leading to a higher barrier for the charge carriers to overcome and thus cannot diffuse from one side to the other side of the junction.[67]

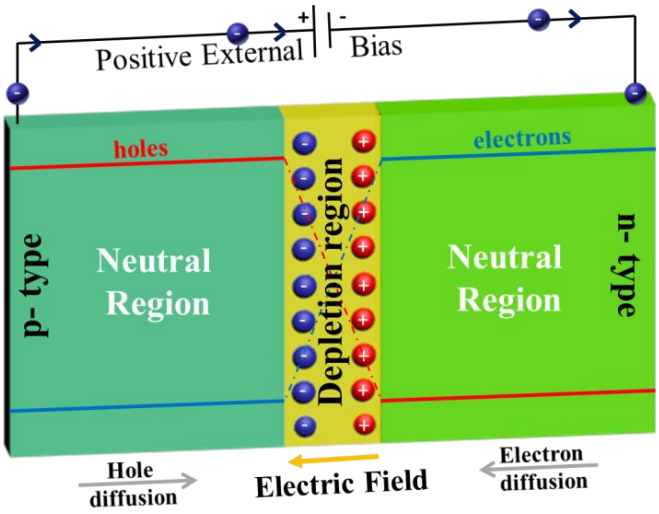

Figure 1. 4. Operation mechanism of a *pn*-junction under applied positive external bias

1.2.5 *pn*-junction under illumination

A solar cell is a photodiode with a *pn*-junction. When a photon of sufficient energy irradiates the device, an electron-hole pair is created. When absorption occurs next to the depletion region, the charge carriers can either drift or diffuse toward the other side of the junction. Thus holes move toward the anode, and electrons toward the cathode. If the holes and electrons reach the depletion region, photocurrent will be produced.[65]

1.2.6 Key photovoltaic parameters

Solar cells are generally characterized by current-density versus voltage (*JV*) plots in dark and under illuminated environments. The key photovoltaic parameters (Figure 1.5) are defined by the short circuit current (J_{sc}), the open circuit voltage (V_{oc}), the maximum power point (P_m), the fill factor (FF) and the efficiency (η).[67-69] J_{sc} is the current going through the solar cell when the applied voltage is equal to zero. It corresponds to the intercept of the *JV* curve with the y-axis. V_{oc} is the voltage going through the device when the measured current is equal to zero. It corresponds to the maximum voltage produced by the device and is located at the intercept of the *JV* curve with the x- axis. P_m is defined as the maximum power produced by the solar cell, where the current (I_m) and voltage (V_m) value are both maximized. It is represented by the maximum square area under the *JV* curve (blue dashed area in Figure 1.5). The FF determines the maximum power from a solar cell. The FF is defined as the available power at P_m in the solar cell. It is calculated by dividing P_m by the product of the J_{sc} and V_{oc}. Graphically; the FF is represented by the "squareness" of the curve. Finally, the efficiency of a solar cell represents the percentage of energy absorbed by the cell converted into electrical energy. It is calculated by dividing the power coming out of the cell by the power going in (P_{in}).

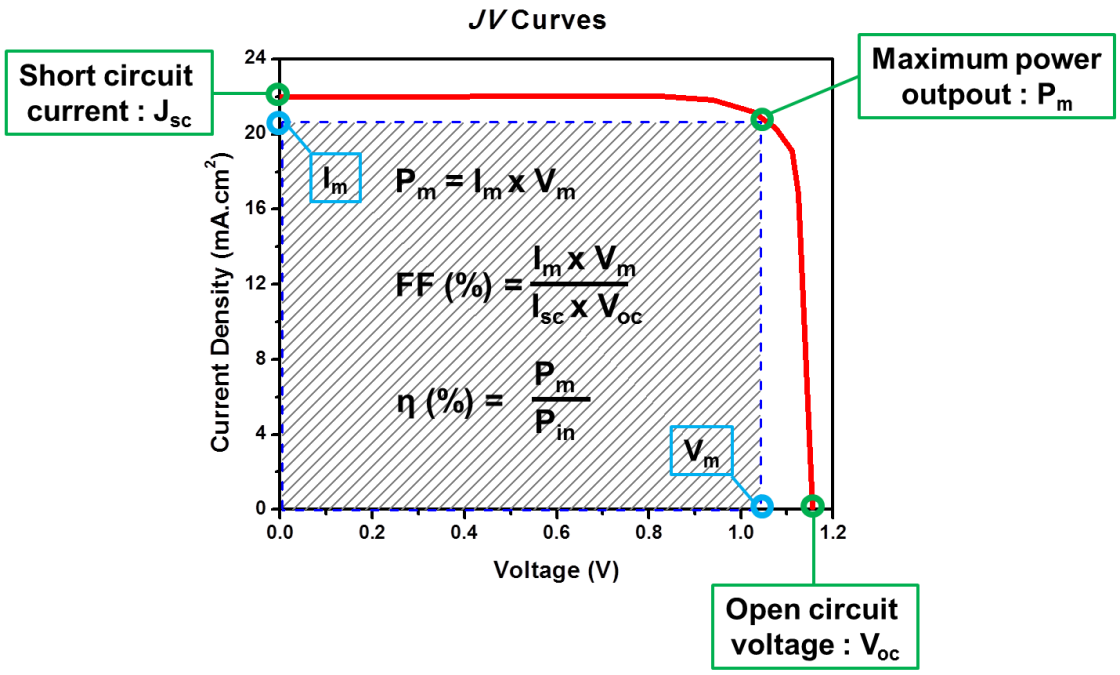

Figure 1. 5. Typical current-density versus voltage curve under illumination. The key photovoltaic parameters (J_{sc}, V_{oc}, P_m) are shown on the plot.

1.3 Emerging photovoltaic materials

The fourth generation of solar cells relies on emerging materials. These materials are called emerging due to their advantageous properties such as broad light absorption over the whole solar spectrum, while having environmentally friendly composition or abundant and low cost precursor materials used for their synthesis. Among these emerging technologies, CZTS and perovskite materials are of broad interest. On one hand, CZTS offers access to low cost and abundant materials with tunable optical properties due to its quaternary composition. On the other hand, perovskite absorber material relies on easy solution process, which require extremely small amount of materials for high efficiency devices. The two materials will be discussed in greater details below.

1.3.1 Cu_2ZnSnS_4 absorber materials

Cu_2ZnSnS_4 often abbreviated as CZTS is a p-type and environmentally friendly semiconductor absorber material with abundant and low cost precursor materials. It has two principals structures: the stannite type ($I\bar{4}2m$) and the kesterite type ($I\bar{4}$).[70] The two structures are defined by a 1x1x2 tetragonal expansion of the zinc blende where only the arrangement between the copper and zinc atoms differ.[57,70-74] Moreover, CZTS (I_2-II-IV-VI_4) has an ideal direct band gap around 1.5 eV and high absorption coefficient ($\alpha > 10^4$ cm^{-1}).[58,59,74-77] CZTS crystals were reported for the first time in 1967 by Nistche et al.[72] The iodine vapor transfer method was used to grow single crystals of the type $A_2^{I}B^{II}C^{IV}X_4$ (where A = Cu; B = Zn, Cd, Fe, Mn, Ni; C = Si, Ge, Sn and X = S, Se). Two decades later, Ito and Nakazawa fabricated a stannite type CZTS thin film semiconductor on heated glass substrates using atom beam sputtering. The films demonstrated a direct optical band gap of 1.45 eV and a large absorption coefficient ($\alpha > 10^4$ cm^{-1}) in the visible wavelength range.[78] Figure 1.6 shows the typical construction for a CZTS thin film device. The solar cell relies on the stacking of several metallic and semiconducting layers.

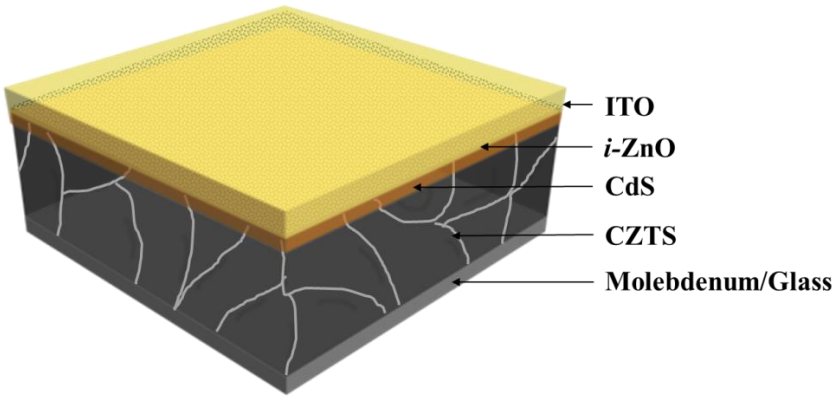

Figure 1. 6. Schematic of a typical CZTS thin film device with the standard configuration of glass-molybdenum/CZTS/cadmium sulfide/intrinsic zinc oxide/indium tin oxide.

From bottom to top, the device contains molybdenum on glass (Mo, ~1µm), CZTS (0.6-2 µm), cadmium sulfide (CdS, 20-70nm), intrinsic zinc oxide (*i*-ZnO, 100-150nm) and indium tin oxide (ITO, ~200 nm). In this configuration, the light is irradiated from the top of the device, where CZTS (*p*-type) is the absorber material forming a *pn*-junction with *i*-ZnO (*n*-type). CdS acts as a buffer layer between the *p*- and *n*-type materials to enhance the band alignment in the *pn*-junction and limit recombination mechanisms. Mo and ITO are the respective bottom and top charge carriers collection electrodes. Following this work, CZTS has been synthesized using various physical and chemical techniques. The best cell efficiencies for each technique are summarized in Table 1.1.

Table 1. 1. Summary of best CZTS solar cell efficiency synthesized using vacuum and non-vacuum based techniques. The * denotes the devices which have been selenized, and thus reflects CZTSSe solar cell efficiencies.

Method	Efficiency	References
e-beam evaporation	5.4%*	Katagiri et al. [79]
thermal evaporation	12.0%*	Winkler et al. [58]
thermal evaporation	8.4%	Shin et al. [85]
RF magnetron sputtering	6.8%*	Katagiri et al. [88]
pulsed laser deposition	2.0%*	Moholkar et al. [94]
electrodeposition	7.3%	Ahmed et al. [95]
blade coating of inks	7.2%*	Guo et al. [71]
spin coating of inks	10.1%*	Aaron et al. [96]

Among the physical techniques, vacuum-based deposition processes such as e-beam evaporation, [79-81] thermal evaporation, [82-85] radio-frequency (RF) magnetron sputtering, [86-88] and

pulsed laser deposition (PLD)[89-94] were widely used to fabricate thin film devices. Another approach was to use chemical techniques such as electrodeposition of CZTS thin film, [95] spin coating[96] or blade coating[71] of inks synthesized by hot injection, [71,75,76,97,98] solvothermal[99-102] and hydrothermal methods.[103-106]The advantages in using chemical approaches rely on tunable optical and electrical properties of the nanocrystals by varying their composition and size. However, CZTS is not limited to spherical shape nanoparticles. A wide range of morphologies has been investigated such has nanorods,[107] nanowires,[108-110] nanotubes,[109] nanoplates,[91,111,112] nanoprism,[113] microspheres,[111,114-116] and quantum dots,[98,117,118] etc. Currently, Mitzi et Al. at IBM holds the record for selenized thin film CZTS solar cell with efficiency up to 12% by vacuum deposition techniques.[58]

1.3.2 Perovskite absorber materials

Perovskites are naturally occurring minerals with ABX_3 structure such as calcium titanate ($CaTiO_3$), which were first discovered in 1839 by G. Rose.[119] Three dimensional organic-inorganic hybrid perovskites with ideal Pm3m cubic structure[3] were synthesized by replacing an inorganic cation (A, cesium) with methyl ammonium (MA = $CH_3NH_3^+$) or formamidinium (FA = $CH(NH_2)_2^+$) cations, conferring semiconducting properties to these new materials.[120] Further, a wide variety of compositions is possible, where B cations can be Pb or Sn and the halide (X) can be any of F, Cl, Br, or I, conferring highly tunable properties to perovskite absorber material. Both MA and FA-based perovskite possess good optical and electrical properties with ideal direct band gaps at 1.55 and 1.47 eV and an absorption edge at 800 and 850 nm, respectively.[119,121-124] This allows them to absorb photons in both the visible and near-infrared solar spectrum. The first perovskite solar cell (PSC) was fabricated in 2009 by Kojima et al.[125]

Unfortunately, the devices were unstable and demonstrated poor performance. The breakthrough for PSCs came in 2012, where devices with efficiencies higher than 10% were reached.[126-129] The reason of this success was based on the use of solid-state planar heterojunction architecture rather than using liquid electrolyte in a sensitized configuration. Over the last 3 years, the interest of PSCs using MA and FA precursors grew, due to unprecedented record efficiencies in a short time span.[12]

Figure 1.7 shows the typical architecture for a planar heterojunction perovskite solar cell. The solar cell relies on stacking of several metallic, organic and semiconducting layers. From bottom to top, the device contains fluorine-doped tin oxide on glass (FTO, ~1µm), compact titanium dioxide (c-TiO_2, 20-50 nm), perovskite (200-600 nm), hole transporting material (HTM, 100 nm), and silver (Ag, 100-150 nm).

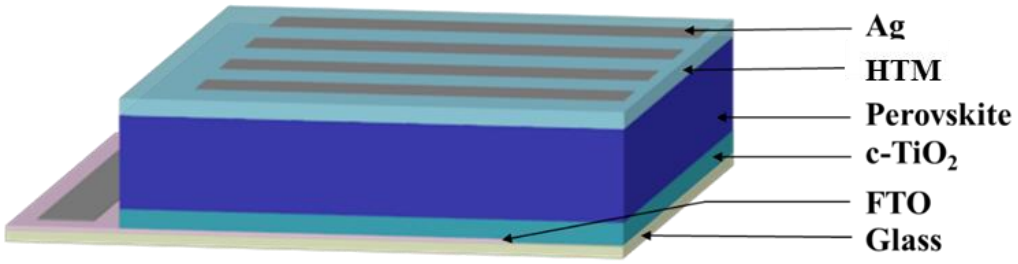

Figure 1. 7. Schematic of a typical perovskite planar heterojnunction device with the standard configuration of glass-FTO/ c-TiO_2/perovskite/hole transporting material/silver.

In this configuration, the light is irradiated from the top of the device, where the perovskite is the absorber material and can form and electron-hole pair. c-TiO_2 acts as a blocking layer to avoid recombination of the charger carriers and the HTM is used to collect the holes which are diffusing upon illumination. FTO and Ag are the electrons and holes collecting electrodes, respectively. Perovskite absorber materials have been synthesized by a vast range of

physical and chemical techniques which are summarized in Table 1.2. Among them vacuum evaporation techniques such as co-evaporation of the precursor materials was proposed,[130] however physical techniques are not suitable for evaporation of organic materials and future mass production.[131]

Table 1. 2. Summary of best perovskite solar cell efficiencies synthesized using vacuum and non-vacuum based techniques. Only published power conversion efficiency data are recorded in this table.

Method	Efficiency (%)	References
co-evaporation	15.5%	Liu et al. [130]
vapor-assisted solution process (VASP)	12.1%	Chen et al. [134]
aerosol-assisted chemical vapor deposition (AACVD)	No device	Lewis et al. [135]
two-step dipping	10.8%	Bi et al. [133]
two-step sequential solution deposition	11.7%	Ma et al. [136]
fast deposition crystallization (FDC)	13.9%	Xiao et al. [137]
spray deposition	11.1%	Barrows et al. [138]
solvent engineering	18.4%	Jeon et al. [62]
spin coating	16.5%	Noel et al. [141]

Two-step dipping (TSD),[132,133] vapor-assisted solution process (VASP),[134] aerosol-assisted chemical vapor deposition (AACVD),[135] two-step sequential solution deposition,[136] fast deposition crystallization (FDC),[137]spray deposition,[138] spin coating,[123,139-141] and solvent engineering techniques[62] are among the most popular method to fabricate high quality perovskite absorber material thin films. Note that the efficiencies recorded in Table 1.2 mostly reflect data published on MA-based solar cells. Besides, the scientific community is still debating on which fabrication method would be the more consistent for standard thin film production.

In 2014, Eperon et al. published the first report on planar heterojunction formamidinium lead trihalide solar cells. Planar heterojunction solar cells were fabricated using single precursor spin-coating route, and demonstrated efficiencies up to 14.2%. This breakthrough rendered formamidinium as viable candidate for PSCs.[122] Currently, the record efficiency for planar heterjunction solar cell based on formamidinium lead triiodide is 20.1%,[12] confirming the importance of studying FA-based solar cells.

1.4 Overview of this dissertation

The work presented in this thesis is divided into **two parts**: Chapters 2 and 3 focus on the integration of CZTS absorber material into nanostructured and dye-sensitized solar cells, whereas Chapters 4, 5 and 6 will focus on fabrication and characterization of planar heterojunction perovskite solar cells. A short abstract for each chapter is given below.

Chapter 2 will focus on nanostructured solar cells. CZTS chalcopyrite semiconductor materials were integrated with the zinc oxide (ZnO) nanowire arrays to form 3D nanostrucutured solar cells. Different synthetic techniques for CZTS and ZnO will be discussed. Morphological, crystallographic, electrical and optical characterization of CZTS and ZnO semiconductor materials will be presented and their integration in solar devices will be discussed.

In **Chapter 3**, ligand-free vertically aligned Cu_2ZnSnS_4 nanoplates were directly synthesized on fluorine doped tin oxide substrate using the pulsed laser deposition (PLD) method, forming a nanoplate array. The array follows a two-step growth process by first forming a Cu_2ZnSnS_4 thin film (~100 nm), followed by vertical nanoplate formation. The nanoplates are about 20 nm thick and 300 nm high with a petal-like shape. Furthermore, the nanoplate array was integrated in a dye sensitized solar cell as a counter electrode with a power conversion efficiency of 3.65%. This is comparable to that of a conventional sputtered Pt counter electrode (3.33%)

and higher than that fabricated with a "classical" Cu_2ZnSnS_4 thin film (2.83%). The Cu_2ZnSnS_4 nanoplate array is proved to be suitable for counter electrode fabrication in achieving Pt-free dye sensitized solar cells, which could significantly decrease the cell cost and provide environmentally friendly photovoltaic devices.

Chapter 4 will report on fabrication parameters of the structural, optical, and electrical properties of formamidinium lead halide perovskite, (prepared by a solvent engineering method) and the device characteristics of planar $FAPbI_3$ solar cells. The fabrication parameters (the concentration of the precursor solution, the solvent engineering techniques and the annealing time and temperature) strongly affect the perovskite film's morphology, and optical properties. Small variation in the refined parameters (0.7M solution concentration, 170˚C, 10 min annealing) strongly impact the final device's efficiency. Devices up to 12% efficiency were fabricated using controlled parameters.

Chapter 5 will report on the effect of humidity on the structural, optical, and electrical properties of formamidinium lead halide perovskite, (prepared by a solvent engineering method) and the device's characteristics of planar $FAPbI_3$ solar cells. The relative humidity affects the perovskite film morphology, which changes from a uniformly covered $FAPbI_3$ film at low relative humidity (e.g., ~2%) to an inhomogeneous film consisting of many voids (or pinholes) at high humidity (30%–40%). This morphological deterioration with increasing humidity is also accompanied by a reduction of the film crystallinity, decay of optical property, and shorter carrier lifetime. The device based on a planar $FAPbI_3$ film shows the best conversion efficiency of 16.6% (with a stabilized output efficiency of 16.4%) at a low humidity (~2%).

Chapter 6 is an *in-situ* observation of the synthesis process inside the electron microscope, which can provide the necessary structure-property basis for controlling the

properties of perovskite solar-cells. Direct observations of the structure and chemistry of formamidinium lead-triiodide films over relevant spatial, time, and temperature scales were used to identify key perovskite formation and degradation mechanisms. Optimized processing protocols were then developed from the *in-situ* study, resulting in the fabrication of devices with conversion efficiencies up to 16.1%.

1.5 References

(1) T.A.Boden; Marland, G.; Andres, R. J. *Carbon Dioxide Information Analysis Center,Oak Ridge National Laboratory, U.S. Department of Energy, Oak Ridge, Tenn., U.S.A.* **2012**.

(2) Shafiee, S.; Topal, E. *Energy Policy* **2009**, *37*, 181.

(3) Wang, W.; Tade, M. O.; Shao, Z. *Chemical Society Reviews* **2015**.

(4) Goeppert, A.; Czaun, M.; Surya Prakash, G. K.; Olah, G. A. *Energy & Environmental Science* **2012**, *5*, 7833.

(5) Kamat, P. V. *The Journal of Physical Chemistry C* **2007**, *111*, 2834.

(6) Administration, E. I.; Energy, D. o., Ed. 2014

(7) Boyle, G. *Renewable energy, 2nd edition*; Oxford University Press, 2004.

(8) Sawin, J. L.; Sverrisson, F. *Renewable 2014 Global Status Report*, 2014.

(9) Brown, M. A.; Levine, M. D.; Short, W.; Koomey, J. G. *Energy Policy* **2001**, *29*, 1179.

(10) Jacobson, M. Z.; Delucchi, M. A.; Bazouin, G.; Bauer, Z. A. F.; Heavey, C. C.; Fisher, E.; Morris, S. B.; Piekutowski, D. J. Y.; Vencill, T. A.; Yeskoo, T. W. *Energy & Environmental Science* **2015**.

(11) Schmalensee, R.; Bulovi'c, V. *The future of solar energy*, 2015.

(12) Green, M. A.; Emery, K.; Hishikawa, Y.; Warta, W.; Dunlop, E. D. *Progress in Photovoltaics: Research and Applications* **2015**, *23*, 805.

(13) Masuko, K.; Shigematsu, M.; Hashiguchi, T.; Fujishima, D.; Kai, M.; Yoshimura, N.; Yamaguchi, T.; Ichihashi, Y.; Mishima, T.; Matsubara, N.; Yamanishi, T.; Takahama, T.; Taguchi, M.; Maruyama, E.; Okamoto, S. *Photovoltaics, IEEE Journal of* **2014**, *4*, 1433.

(14) Goetzberger, A. In *Workshop on Physics for 'RENEWABLE ENERGY'* Milan, 2005.

(15) Zhao, J.; Wang, A.; Yun, F.; Zhang, G.; Roche, D. M.; Wenham, S. R.; Green, M. A. *Prog. Photovoltaics* **1997**, *5*, 269.

(16) Zhao, J. H.; Wang, A. H.; Green, M. A.; Ferrazza, F. *Applied Physics Letters* **1998**, *73*, 1991.

(17) Aberle, A. G. *Progress in Photovoltaics: Research and Applications* **2000**, *8*, 473.

(18) Chu, T. L.; Chu, S. S.; Britt, J.; Ferekides, C.; Wang, C.; Wu, C. Q.; Ullal, H. S. *Electron Device Letters, IEEE* **1992**, *13*, 303.

(19) Wu, X.; Zhou, J.; Duda, A.; Yan, Y.; Teeter, G.; Asher, S.; Metzger, W. K.; Demtsu, S.; Wei, S.-H.; Noufi, R. *Thin Solid Films* **2007**, *515*, 5798.

(20) Sites, J.; Pan, J. *Thin Solid Films* **2007**, *515*, 6099.

(21) Nakayama, N.; Matsumoto, H.; Yamaguchi, K.; Ikegami, S.; Hioki, Y. *Japanese Journal of Applied Physics* **1976**, *15*, 2281.

(22) Meyers, P. V. *Solar Cells* **1988**, *23*, 59.

(23) Morales-Acevedo, A. *Solar Energy* **2006**, *80*, 675.

(24) Ohyama, H.; Aramoto, T.; Kumazawa, S.; Higuchi, H.; Arita, T.; Shibutani, S.; Nishio, T.; Nakajima, J.; Tsuji, M.; Hanafusa, A.; Hibino, T.; Omura, K.; Murozono, M. In *Photovoltaic Specialists Conference, 1997., Conference Record of the Twenty-Sixth IEEE* 1997, p 343.

(25) Wallin, E.; Malm, U.; Jarmar, T.; Lundberg, O.; Edoff, M.; Stolt, L. *Prog. Photovoltaics* **2012**, *20*, 851.

(26) Repins, I.; Contreras, M. A.; Egaas, B.; DeHart, C.; Scharf, J.; Perkins, C. L.; To, B.; Noufi, R. *Progress in Photovoltaics: Research and Applications* **2008**, *16*, 235.

(27) Ramanathan, K.; Contreras, M. A.; Perkins, C. L.; Asher, S.; Hasoon, F. S.; Keane, J.; Young, D.; Romero, M.; Metzger, W.; Noufi, R.; Ward, J.; Duda, A. *Progress in Photovoltaics: Research and Applications* **2003**, *11*, 225.

(28) Jackson, P.; Hariskos, D.; Lotter, E.; Paetel, S.; Wuerz, R.; Menner, R.; Wischmann, W.; Powalla, M. *Progress in Photovoltaics: Research and Applications* **2011**, *19*, 894.

(29) Jackson, P.; Hariskos, D.; Wuerz, R.; Wischmann, W.; Powalla, M. *physica status solidi (RRL) – Rapid Research Letters* **2014**, *8*, 219.

(30) Jackson, P.; Hariskos, D.; Wuerz, R.; Kiowski, O.; Bauer, A.; Friedlmeier, T. M.; Powalla, M. *physica status solidi (RRL) – Rapid Research Letters* **2015**, *9*, 28.

(31) Carlson, D. E.; Wronski, C. R. *Applied Physics Letters* **1976**, *28*, 671.

(32) Spear, W. E.; Le Comber, P. G. *Solid State Communications* **1975**, *17*, 1193.

(33) Taguchi, M.; Yano, A.; Tohoda, S.; Matsuyama, K.; Nakamura, Y.; Nishiwaki, T.; Fujita, K.; Maruyama, E. *Photovoltaics, IEEE Journal of* **2014**, *4*, 96.

(34) Tamang, A.; Hongsingthong, A.; Sichanugrist, P.; Jovanov, V.; Konagai, M.; Knipp, D. *Photovoltaics, IEEE Journal of* **2014**, *4*, 16.

(35) Park, S.; Yong Ji, H.; Jun Kim, M.; Hyeon Peck, J.; Kim, K. *Applied Physics Letters* **2014**, *104*, 073902.

(36) Kim, J.; Battaglia, C.; Charrière, M.; Hong, A.; Jung, W.; Park, H.; Ballif, C.; Sadana, D. *Advanced Materials* **2014**, *26*, 4082.

(37) Sai, H.; Matsui, T.; Matsubara, K.; Kondo, M.; Yoshida, I. *IEEE J. Photovolt.* **2014**, *4*, 1349.

(38) Steiner, M.; Bösch, A.; Dilger, A.; Dimroth, F.; Dörsam, T.; Muller, M.; Hornung, T.; Siefer, G.; Wiesenfarth, M.; Bett, A. W. *Progress in Photovoltaics: Research and Applications* **2014**, n/a.

(39) Yamaguchi, M. *Solar Energy Materials and Solar Cells* **2003**, *75*, 261.

(40) Meerheim, R.; Körner, C.; Leo, K. *Applied Physics Letters* **2014**, *105*, 063306.

(41) Dimroth, F.; Grave, M.; Beutel, P.; Fiedeler, U.; Karcher, C.; Tibbits, T. N. D.; Oliva, E.; Siefer, G.; Schachtner, M.; Wekkeli, A.; Bett, A. W.; Krause, R.; Piccin, M.; Blanc, N.; Drazek, C.; Guiot, E.; Ghyselen, B.; Salvetat, T.; Tauzin, A.; Signamarcheix, T.; Dobrich, A.; Hannappel, T.; Schwarzburg, K. *Progress in Photovoltaics: Research and Applications* **2014**, *22*, 277.

(42) Chuang, C.-H. M.; Brown, P. R.; Bulović, V.; Bawendi, M. G. *Nat Mater* **2014**, *13*, 796.

(43) Milliron, D. J. *Nat Mater* **2014**, *13*, 772.

(44) Pan, Z.; Mora-Seró, I.; Shen, Q.; Zhang, H.; Li, Y.; Zhao, K.; Wang, J.; Zhong, X.; Bisquert, J. *Journal of the American Chemical Society* **2014**, *136*, 9203.

(45) Ko, D.-K.; Brown, P. R.; Bawendi, M. G.; Bulović, V. *Advanced Materials* **2014**, *26*, 4845.

(46) Mathew, S.; Yella, A.; Gao, P.; Humphry-Baker, R.; CurchodBasile, F. E.; Ashari-Astani, N.; Tavernelli, I.; Rothlisberger, U.; NazeeruddinMd, K.; Grätzel, M. *Nat Chem* **2014**, *6*, 242.

(47) Yella, A.; Mai, C.-L.; Zakeeruddin, S. M.; Chang, S.-N.; Hsieh, C.-H.; Yeh, C.-Y.; Grätzel, M. *Angewandte Chemie* **2014**, *126*, 3017.

(48) Lau, G. P. S.; Tsao, H. N.; Yi, C.; Zakeeruddin, S. M.; Grätzel, M.; Dyson, P. J. *ChemSusChem* **2015**, *8*, 255.

(49) Wu, W.-Q.; Xu, Y.-F.; Su, C.-Y.; Kuang, D.-B. *Energy & Environmental Science* **2014**, *7*, 644.

(50) Liu, Y.; Zhao, J.; Li, Z.; Mu, C.; Ma, W.; Hu, H.; Jiang, K.; Lin, H.; Ade, H.; Yan, H. *Nat Commun* **2014**, *5*.

(51) Zhou, N.; Lin, H.; Lou, S. J.; Yu, X.; Guo, P.; Manley, E. F.; Loser, S.; Hartnett, P.; Huang, H.; Wasielewski, M. R.; Chen, L. X.; Chang, R. P. H.; Facchetti, A.; Marks, T. J. *Advanced Energy Materials* **2014**, *4*, n/a.

(52) Carle, J. E.; Helgesen, M.; Madsen, M. V.; Bundgaard, E.; Krebs, F. C. *Journal of Materials Chemistry C* **2014**, *2*, 1290.

(53) Chen, J.-D.; Cui, C.; Li, Y.-Q.; Zhou, L.; Ou, Q.-D.; Li, C.; Li, Y.; Tang, J.-X. *Advanced Materials* **2015**, *27*, 1035.

(54) Li, W.; Roelofs, W. S. C.; Turbiez, M.; Wienk, M. M.; Janssen, R. A. J. *Advanced Materials* **2014**, *26*, 3304.

(55) Wang, W.; Winkler, M. T.; Gunawan, O.; Gokmen, T.; Todorov, T. K.; Zhu, Y.; Mitzi, D. B. *Advanced Energy Materials* **2014**, *4*, n/a.

(56) Su, Z.; Sun, K.; Han, Z.; Cui, H.; Liu, F.; Lai, Y.; Li, J.; Hao, X.; Liu, Y.; Green, M. A. *Journal of Materials Chemistry A* **2014**, *2*, 500.

(57) Collord, A. D.; Hillhouse, H. W. *Chemistry of Materials* **2015**, *27*, 1855.

(58) Winkler, M. T.; Wang, W.; Gunawan, O.; Hovel, H. J.; Todorov, T. K.; Mitzi, D. B. *Energy & Environmental Science* **2014**, *7*, 1029.

(59) Hiroi, H.; Kim, J.; Kuwahara, M.; Todorov, T. K.; Nair, D.; Hopstaken, M.; Yu, Z.; Gunawan, O.; Mitzi, D. B.; Sugimoto, H. In *Photovoltaic Specialist Conference (PVSC), 2014 IEEE 40th* 2014, p 0030.

(60) Zhou, H.; Chen, Q.; Li, G.; Luo, S.; Song, T.-b.; Duan, H.-S.; Hong, Z.; You, J.; Liu, Y.; Yang, Y. *Science* **2014**, *345*, 542.

(61) Liu, D.; Kelly, T. L. *Nat Photon* **2014**, *8*, 133.

(62) Jeon, N. J.; Noh, J. H.; Kim, Y. C.; Yang, W. S.; Ryu, S.; Seok, S. I. *Nat Mater* **2014**, *13*, 897.

(63) Malinkiewicz, O.; Yella, A.; Lee, Y. H.; Espallargas, G. M.; Graetzel, M.; Nazeeruddin, M. K.; Bolink, H. J. *Nat Photon* **2014**, *8*, 128.

(64) Mei, A.; Li, X.; Liu, L.; Ku, Z.; Liu, T.; Rong, Y.; Xu, M.; Hu, M.; Chen, J.; Yang, Y.; Grätzel, M.; Han, H. *Science* **2014**, *345*, 295.

(65) Dyakonov, M. I. In *Spin Physics in Semiconductors*; Dyakonov, M., Ed.; Springer Berlin Heidelberg: 2008; Vol. 157, p 1.

(66) Hermann, K. In *Computational Methods in Catalysis and Materials Science*; Wiley-VCH Verlag GmbH & Co. KGaA: 2009, p 265.

(67) www.pveducation.org, 2015.

(68) Nelson, J. *The Physics of Solar Cells* Imperial College Press, 2003.

(69) Xiaodong Wang; Wang, Z. M. *High-Efficiency Solar Cells*; Springer International Publishing, 2014; Vol. 190.

(70) Catlow, C. R. A.; Guo, Z. X.; Miskufova, M.; Shevlin, S. A.; Smith, A. G. H.; Sokol, A. A.; Walsh, A.; Wilson, D. J.; Woodley, S. M. *Phil. Trans. R. Soc. A.* **2010**, *368*, 3379.

(71) Guo, Q.; Ford, G. M.; Yang, W.-C.; Walker, B. C.; Stach, E. A.; Hillhouse, H. W.; Agrawal, R. *J. Am. Chem. Soc.* **2010**, *132*, 17384.

(72) Nitsche, R.; Sargent, D. F.; Wild, P. *Journal of Crystal Growth* **1967**, *1*, 52.

(73) van Embden, J.; Chesman, A. S. R.; Della Gaspera, E.; Duffy, N. W.; Watkins, S. E.; Jasieniak, J. J. *Journal of the American Chemical Society* **2014**, *136*, 5237.

(74) Riha, S. C.; Parkinson, B. A.; Prieto, A. L. *Journal of the American Chemical Society* **2009**, *131*, 12054.

(75) Riha, S. C.; Parkinson, B. A.; Prieto, A. L. *Journal of the American Chemical Society* **2011**, *133*, 15272.

(76) Guo, Q.; Hillhouse, H. W.; Agrawal, R. *Journal of the American Chemical Society* **2009**, *131*, 11672.

(77) Shavel, A.; Cadavid, D.; Ibáñez, M.; Carrete, A.; Cabot, A. *Journal of the American Chemical Society* **2012**, *134*, 1438.

(78) Kentaro, I.; Tatsuo, N. *Japanese Journal of Applied Physics* **1988**, *27*, 2094.

(79) Katagiri, H.; Sasaguchi, N.; Hando, S.; Hoshino, S.; Ohashi, J.; Yokota, T. *Solar Energy Materials and Solar Cells* **1997**, *49*, 407.

(80) Takeshi, K.; Kazuo, J.; Kazuyuki, T.; Shunsuke, S.; Taisuke, O.; Hironori, K. *Japanese Journal of Applied Physics* **2005**, *44*, 783.

(81) Katagiri, H.; Saitoh, K.; Washio, T.; Shinohara, H.; Kurumadani, T.; Miyajima, S. *Solar Energy Materials and Solar Cells* **2001**, *65*, 141.

(82) Shi, C.; Shi, G.; Chen, Z.; Yang, P.; Yao, M. *Materials Letters* **2012**, *73*, 89.

(83) Oishi, K.; Saito, G.; Ebina, K.; Nagahashi, M.; Jimbo, K.; Maw, W. S.; Katagiri, H.; Yamazaki, M.; Araki, H.; Takeuchi, A. *Thin Solid Films* **2008**, *517*, 1449.

(84) Tombak, A.; Ocak, Y. S.; Genişel, M. F.; Kilicoglu, T. *Materials Science in Semiconductor Processing* **2014**, *28*, 98.

(85) Shin, B.; Gunawan, O.; Zhu, Y.; Bojarczuk, N. A.; Chey, S. J.; Guha, S. *Progress in Photovoltaics: Research and Applications* **2013**, *21*, 72.

(86) Hironori, K.; Kazuo, J.; Satoru, Y.; Tsuyoshi, K.; Win Shwe, M.; Tatsuo, F.; Tadashi, I.; Tomoyoshi, M. *Applied Physics Express* **2008**, *1*, 041201.

(87) Seol, J.-S.; Lee, S.-Y.; Lee, J.-C.; Nam, H.-D.; Kim, K.-H. *Solar Energy Materials and Solar Cells* **2003**, *75*, 155.

(88) Tanaka, T.; Nagatomo, T.; Kawasaki, D.; Nishio, M.; Guo, Q.; Wakahara, A.; Yoshida, A.; Ogawa, H. *Journal of Physics and Chemistry of Solids* **2005**, *66*, 1978.

(89) Moriya, K.; Tanaka, K.; Uchiki, H. *Japanese Journal of Applied Physics, Part 1: Regular Papers and Short Notes and Review Papers* **2007**, *46*, 5780.

(90) Moriya, K.; Tanaka, K.; Uchiki, H. *Japanese Journal of Applied Physics* **2008**, *47*, 602.

(91) Wozny, S.; Wang, K.; Zhou, W. *Journal of Materials Chemistry A* **2013**, *1*, 15517.

(92) Vanalakar, S. A.; Agawane, G. L.; Shin, S. W.; Suryawanshi, M. P.; Gurav, K. V.; Jeon, K. S.; Patil, P. S.; Jeong, C. W.; Kim, J. Y.; Kim, J. H. *Journal of Alloys and Compounds* **2015**, *619*, 109.

(93) Katsuhiko, M.; Kunihiko, T.; Hisao, U. *Japanese Journal of Applied Physics* **2007**, *46*, 5780.

(94) Moholkar, A. V.; Shinde, S. S.; Babar, A. R.; Sim, K.-U.; Kwon, Y.-b.; Rajpure, K. Y.; Patil, P. S.; Bhosale, C. H.; Kim, J. H. *Solar Energy* **2011**, *85*, 1354.

(95) Ahmed, S.; Reuter, K. B.; Gunawan, O.; Guo, L.; Romankiw, L. T.; Deligianni, H. *Advanced Energy Materials* **2012**, *2*, 253.

(96) Barkhouse, D. A. R.; Gunawan, O.; Gokmen, T.; Todorov, T. K.; Mitzi, D. B. *Progress in Photovoltaics: Research and Applications* **2012**, *20*, 6.

(97) Steinhagen, C.; Panthani, M. G.; Akhavan, V.; Goodfellow, B.; Koo, B.; Korgel, B. A. *J. Am. Chem. Soc.* **2009**, *131*, 12554.

(98) Khare, A.; Wills, A. W.; Ammerman, L. M.; Norris, D. J.; Aydil, E. S. *Chemical Communications* **2011**, *47*, 11721.

(99) Pal, M.; Mathews, N. R.; Gonzalez, R. S.; Mathew, X. *Thin Solid Films* **2013**, *535*, 78.

(100) Long, F.; Mo, S.; Zeng, Y.; Chi, S.; Zou, Z. *International Journal of Photoenergy* **2014**, *2014*, 4.

(101) Wei, A.; Yan, Z.; Zhao, Y.; Zhuang, M.; Liu, J. *International Journal of Hydrogen Energy* **2015**, *40*, 797.

(102) Chen, S.; Tao, H.; Shen, Y.; Zhu, L.; Zeng, X.; Tao, J.; Wang, T. *RSC Advances* **2015**, *5*, 6682.

(103) Vanalakar, S. A.; Agwane, G. L.; Gang, M. G.; Patil, P. S.; Kim, J. H.; Kim, J. Y. *physica status solidi (c)* **2015**, *12*, 500.

(104) Wang, J.; Zhang, P.; Song, X.; Gao, L. *RSC Advances* **2014**, *4*, 27805.

(105) Verma, S. k.; Agrawal, V.; Jain, K.; Pasricha, R.; Chand, S. *Journal of Nanoparticles* **2013**, *2013*, 7.

(106) Sekou Mariama, C.; Lingling, W.; Xintong, Z. *Nanotechnology* **2013**, *24*, 495401.

(107) Singh, A.; Geaney, H.; Laffir, F.; Ryan, K. M. *J. Am. Chem. Soc.* **2012**, *134*, 2910.

(108) Shi, L.; Pei, C.; Xu, Y.; Li, Q. *J. Am. Chem. Soc.* **2011**, *133*, 10328.

(109) Su, Z.; Yan, C.; Tang, D.; Sun, K.; Han, Z.; Liu, F.; Lai, Y.; Li, J.; Liu, Y. *CrystEngComm* **2012**, *14*, 782.

(110) Jeon, M.; Shimizu, T.; Shingubara, S. *Materials Letters* **2011**, *65*, 2364.

(111) Xu, J.; Yang, X.; Yang, Q.-D.; Wong, T.-L.; Lee, C.-S. *J. Phys. Chem. C* **2012**, *116*, 19718.

(112) Chang, J.; Waclawik, E. R. *RSC Advances* **2014**, *4*, 23505.

(113) Ramasamy, K.; Malik, M. A.; O'Brien, P. *Chemical Communications* **2012**, *48*, 5703.

(114) Saravana Kumar, R.; Ryu, B. D.; Chandramohan, S.; Seol, J. K.; Lee, S.-K.; Hong, C.-H. *Materials Letters* **2012**, *86*, 174.

(115) Sarkar, S.; Bhattacharjee, K.; Das, G. C.; Chattopadhyay, K. K. *CrystEngComm* **2014**, *16*, 2634.

(116) Liu, J.; Luo, F.; Wei, A.; Liu, Z.; Zhao, Y. *Materials Letters* **2015**, *141*, 228.

(117) Rajesh, G.; Muthukumarasamy, N.; Subramanian, E. P.; Venkatraman, M. R.; Agilan, S.; Ragavendran, V.; Thambidurai, M.; Velumani, S.; Yi, J.; Velauthapillai, D. *Superlattices and Microstructures* **2015**, *77*, 305.

(118) Bai, B.; Kou, D.-X.; Zhou, W.-H.; Zhou, Z.-J.; Wu, S.-X. *Green Chemistry* **2015**.

(119) Gratzel, M. *Nat Mater* **2014**, *13*, 838.

(120) Mitzi, D. B. In *Progress in Inorganic Chemistry*; John Wiley & Sons, Inc.: 2007, p 1.

(121) Baikie, T.; Fang, Y.; Kadro, J. M.; Schreyer, M.; Wei, F.; Mhaisalkar, S. G.; Graetzel, M.; White, T. J. *Journal of Materials Chemistry A* **2013**, *1*, 5628.

(122) Eperon, G. E.; Stranks, S. D.; Menelaou, C.; Johnston, M. B.; Herz, L. M.; Snaith, H. J. *Energy & Environmental Science* **2014**, *7*, 982.

(123) Koh, T. M.; Fu, K.; Fang, Y.; Chen, S.; Sum, T. C.; Mathews, N.; Mhaisalkar, S. G.; Boix, P. P.; Baikie, T. *The Journal of Physical Chemistry C* **2013**, *118*, 16458.

(124) Kim, H.-S.; Lee, C.-R.; Im, J.-H.; Lee, K.-B.; Moehl, T.; Marchioro, A.; Moon, S.-J.; Humphry-Baker, R.; Yum, J.-H.; Moser, J. E.; Gratzel, M.; Park, N.-G. *Sci. Rep.* **2012**, *2*.

(125) Kojima, A.; Teshima, K.; Shirai, Y.; Miyasaka, T. *Journal of the American Chemical Society* **2009**, *131*, 6050.

(126) Zhao, Y.; Zhu, K. *Journal of the American Chemical Society* **2014**, *136*, 12241.

(127) Lee, J.-W.; Seol, D.-J.; Cho, A.-N.; Park, N.-G. *Advanced Materials* **2014**, *26*, 4991.

(128) Chen, Q.; Zhou, H.; Hong, Z.; Luo, S.; Duan, H.-S.; Wang, H.-H.; Liu, Y.; Li, G.; Yang, Y. *Journal of the American Chemical Society* **2013**, *136*, 622.

(129) Im, J.-H.; Jang, I.-H.; Pellet, N.; Grätzel, M.; Park, N.-G. *Nat Nano* **2014**, *advance online publication*.

(130) Liu, M.; Johnston, M. B.; Snaith, H. J. *Nature* **2013**, *501*, 395.

(131) Ball, J. M.; Lee, M. M.; Hey, A.; Snaith, H. J. *Energy & Environmental Science* **2013**, *6*, 1739.

(132) Liang, K.; Mitzi, D. B.; Prikas, M. T. *Chemistry of Materials* **1998**, *10*, 403.

(133) Bi, D.; Moon, S.-J.; Haggman, L.; Boschloo, G.; Yang, L.; Johansson, E. M. J.; Nazeeruddin, M. K.; Gratzel, M.; Hagfeldt, A. *RSC Advances* **2013**, *3*, 18762.

(134) Chen, Q.; Zhou, H.; Hong, Z.; Luo, S.; Duan, H.-S.; Wang, H.-H.; Liu, Y.; Li, G.; Yang, Y. *Journal of the American Chemical Society* **2014**, *136*, 622.

(135) Lewis, D. J.; O'Brien, P. *Chemical Communications* **2014**, *50*, 6319.

(136) Ma, Y.; Zheng, L.; Chung, Y.-H.; Chu, S.; Xiao, L.; Chen, Z.; Wang, S.; Qu, B.; Gong, Q.; Wu, Z.; Hou, X. *Chemical Communications* **2014**, *50*, 12458.

(137) Xiao, M.; Huang, F.; Huang, W.; Dkhissi, Y.; Zhu, Y.; Etheridge, J.; Gray-Weale, A.; Bach, U.; Cheng, Y.-B.; Spiccia, L. *Angewandte Chemie International Edition* **2014**, *53*, 9898.

(138) Barrows, A. T.; Pearson, A. J.; Kwak, C. K.; Dunbar, A. D. F.; Buckley, A. R.; Lidzey, D. G. *Energy & Environmental Science* **2014**, *7*, 2944.

(139) Lv, S.; Pang, S.; Zhou, Y.; Padture, N. P.; Hu, H.; Wang, L.; Zhou, X.; Zhu, H.; Zhang, L.; Huang, C.; Cui, G. *Physical Chemistry Chemical Physics* **2014**, *16*, 19206.

(140) Pang, S.; Hu, H.; Zhang, J.; Lv, S.; Yu, Y.; Wei, F.; Qin, T.; Xu, H.; Liu, Z.; Cui, G. *Chemistry of Materials* **2014**, *26*, 1485.

(141) Noel, N. K.; Abate, A.; Stranks, S. D.; Parrott, E. S.; Burlakov, V. M.; Goriely, A.; Snaith, H. J. *ACS Nano* **2014**, *8*, 9815.

Chapter 2 Bulk heterojunction formation between Zinc Oxide nanowire array and Cu_2ZnSnS_4 nanoparticles for 3-Dimensional nanostructured solar cells*

2.1 Introduction

With 1.3 billion people without access to electricity and a perpetual energy demand, it is critical to find low cost, reliable and clean ways to produce energy. In 2013, the worldwide production of renewable electricity accounted for 22.1% of the total energy production. The renewable electricity was produced from hydropower (16.4%), wind (2.9%), bio-power (1.8%), solar photovoltaic (0.7%) and geothermal (0.4%). Despite this extremely low production from solar power, photovoltaics are the renewable energy which generates the highest investment (53%) for clean energy production.[1] Therefore, the demand for highly efficient photovoltaics, which relies on green and abundant materials keep increasing. [1,2] The major goal for commercialization of photovoltaic cells is to significantly increase the energy conversion efficiency while cutting down the cost. To reach this goal, engineering nanostructured materials to achieve high efficiency is very crucial. Nanostructure based solar cells are ideal candidates for fulfilling this perpetual demand.[3-7]

1D radial nanostructures compared to planar demonstrate the advantages of optimal light absorption,[4,5,8-12] enhanced charge carrier collection efficiency,[7,13-15] and smaller recombination loss of minority carriers at the interfaces,[7,13,16-18] thus enhancing the solar cell efficiency.[2,4,5,8,10,12-17,19-22] However, nanostructure based solar cells have not reach yet the power conversion efficiencies achieved for planar solar cells. [21,23]

*This chapter was adapted from: Wozny, S.; Wang, K.; Alkurd, N.; Zhou, W., Heterojunction Formation between Zinc Oxide Nanowires and Cu_2ZnSnS_4 Nanoparticles For Inorganic 3D Solar Cell Applications *Proc. 42th IEEE PVSC 2015*, **2015**

Recently, there has been a growing interest for Cu_2ZnSnS_4 (CZTS) quaternary semiconductor due to the abundance and low cost of its precursors. Moreover, this chalcopyrite material has an ideal direct band gap around 1.5 eV, [24] high absorption coefficient [25] ($\alpha > 10^4$ cm^{-1}) and high conductivity[26] that makes it suitable for nanostructure solar cells applications. CZTS has been synthesized by several methods over recent years,[27] such as sputtering, [28, 29] evaporation,[28] pulse laser deposition, [26,31, 32] and synthesis of nanocrystals inks,[29-33] etc.[33-38] The synthetic methods, however, are limited to the formation of thin film structure so far, which generated the excessive loss of minority carriers in the semiconductor layers through the junction.[23]

Three dimensional (3D) nanostructures demonstrated new structures and physics for limiting the recombination at the interfaces, thus enhancing the solar cell efficiency. [18,21,23,39] Since the conversion efficiency is mainly controlled by the composition of the nanocrystals, the structure of the device, and the morphology of CZTS; a three-dimensional (3D) nano-junction is a potential solution to this issue due to the reduced lateral travel distance for the minority carriers which would decrease the defect trapping problem.[21] Ultimately, an extremely thin *p*-type absorber layer (CZTS) and an *n*-type nanostructure (ZnO Nanowires) could potentially increase the charge collection efficiency of the device through the lateral junction while maintaining a complete light absorption due to multiple absorption paths.

In this work, CZTS nanocrystals (*p*-type) were synthesized by hot injection method or pulsed laser deposition technique (PLD), and deposited in the interstitial space of pre-fabricated zinc oxide (ZnO) nanowires array to form a 3D heterojunction device. A *pn*-junction was successfully created, as well as workable devices, demonstrating the potential of CZTS as an inorganic 3D bulk heterojunction for solar cell applications.

2.2 Experimental

2.2.1 Synthesis of CZTS

2.2.1.1 Synthesis of CZTS nanocrystal ink by hot injection method

The synthesis of CZTS nanocrystals was performed following Guo *et al*., method with slight modifications.[32] The hot injection synthetic process is summarized in Figure 2.1. Briefly, copper II acethylacetonate (0.48 mmol), tin IV acetate (0.25 mmol) and zinc acetate (0.27 mmol) were added to 16 mL of oleylamine which was degassed using three times the freeze thaw method.

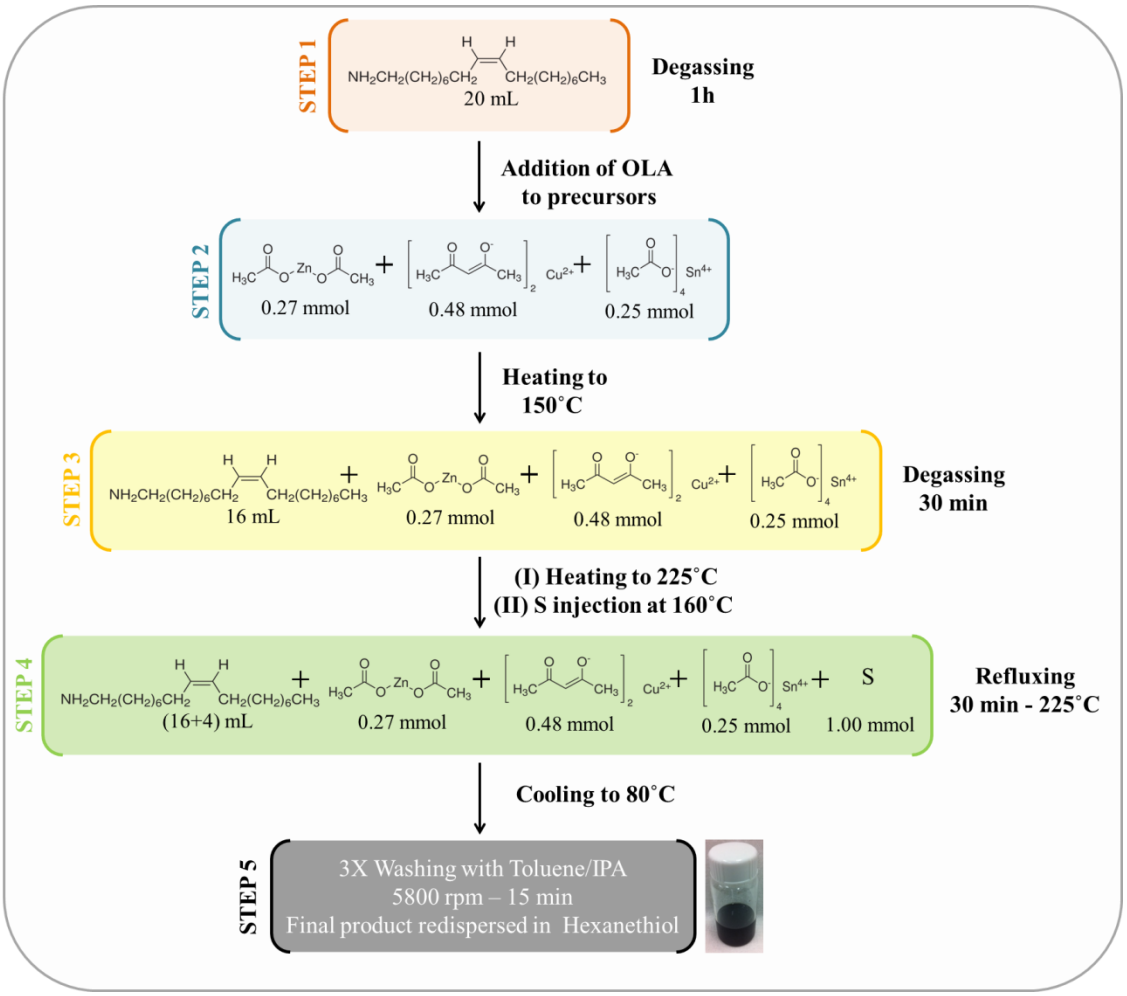

Figure 2. 1. Schematic summarizing the hot injection process for the synthesis of CZTS nanocrystals.

The mixture was heated to 150 ˚C under vacuum and subsequently degassed and purged for 30 min. In a 20 mL scintillation vial, elemental sulfur (1 mmol) was sonicated in 4 mL of oleylamine at 60 ˚C until complete dissolution of the sulfur. When the metal precursor solution reached 160 ˚C, 3 mL of the sulfur-oleylamine solution were rapidly injected. The metal precursor was then heated to 225 ˚C and kept at this temperature for 30 min under nitrogen atmosphere. The reaction was cooled to room temperature by removing the heating mantle and small amounts of toluene were added to avoid aggregation and solidification of the nanocrystals. Toluene and isopropyl alcohol (IPA) were used, respectively to precipitate and redisperse the nanocrystals. The solution was then centrifuged, and the washing process was repeated 3 times. The nanocrystals were dried under vacuum and redispersed in hexanethiol to form stable black ink.

2.2.1.2 Synthesis of CZTS by pulse laser deposition

A custom made PLD system (Figure 2.2) was used for CZTS deposition. A Nd:YAG pulsed laser with a wavelength of 1064 nm and a repetition rate of 10 Hz was focused on a sintered CZTS target placed inside a 1 inch quartz tube connected to a vacuum pump. The CZTS target was prepared by mixing stoichiometric amount of Cu_2S, ZnS and SnS_2 (1:1:1) powder, which was pressed into a pellet of 10 mm diameter and 3-5 mm thickness. The pellet was sealed in an evacuated quartz tube and annealed for 20 h at 750˚C with a heating and cooling ramp of 2 ˚C/min.[40] Before deposition, the target was polished to achieve a smooth and uniform surface. The substrate was then cleaned and placed in front of the target and the tube was flushed with Ar and evacuated several times before pumped down to 800 mTorr. The quartz tube was heated to 450˚C, and the target was ablated for 3 hours at 27 mJ/cm^2, followed by 15 min at 32 mJ/cm^2.

The target was then annealed for 10 min at 450˚C and naturally cooled to room temperature for future experiments.

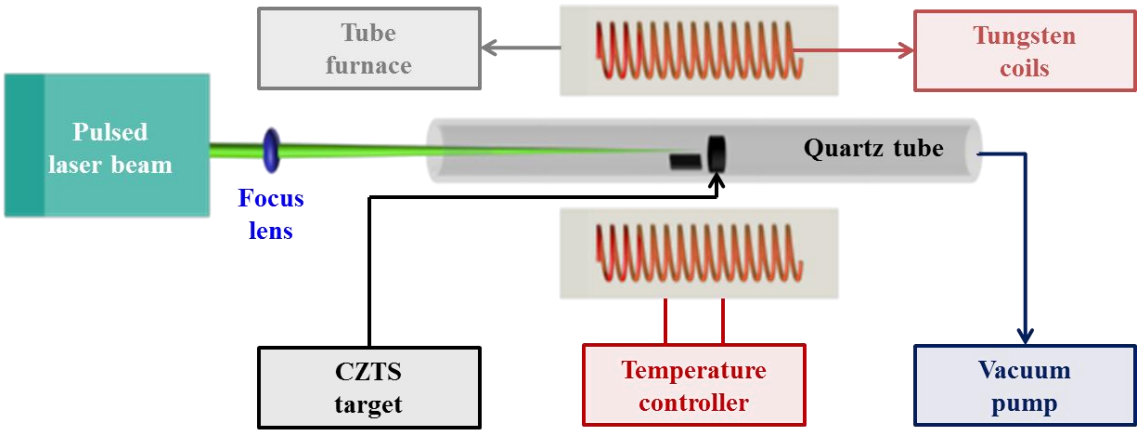

Figure 2. 2. Schematic of the custom made pulsed laser deposition system

2.2.2 Synthesis of ZnO nanowire array

Glass substrates were ordered from VWR, and conventionally washed. A 100 nm seed layer of Aluminum-ZnO (AZO) was RF sputtered (60W) on the clean glass and annealed at 450˚C for 1 h. Further, ZnO nanowires were hydrothermally grown using slight modification from the conventional growth method.[41] Zinc nitrate hexahydrate (25 mM), hexamethylenetetramine (HMT) (25 mM) and polyethyleneimine (PEI) (5mM) solution in DI water were mixed together and heated up to 90˚C. A substrate was immersed in the solution for 10 hours. The solution was replaced with fresh one every two hours to maintain a constant growth rate. The substrate was then lightly sonicated to remove artifact from the growth solution, washed with DI water and annealed at 450 ˚C for 1 h. Figure 2.3 summarizes the synthetic process for the growth of vertically aligned ZnO nanowires.

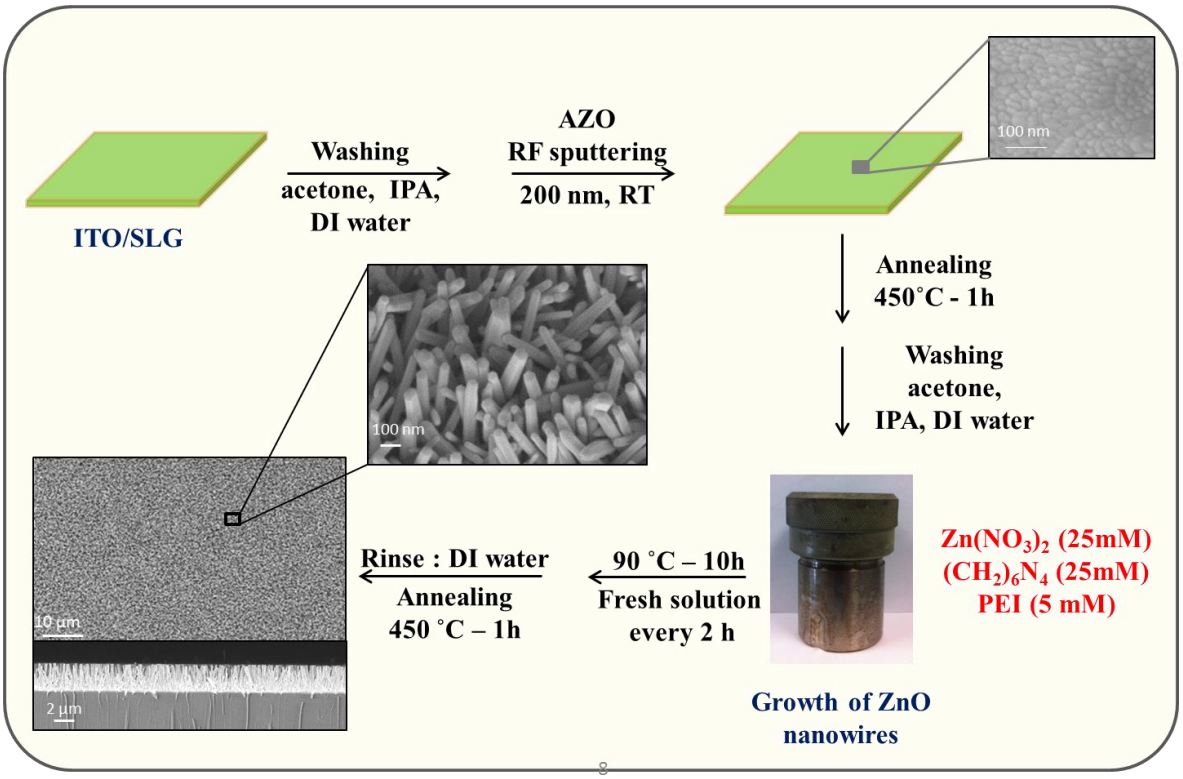

Figure 2. 3. Schematic summarizing the hydrothermal method for the synthesis of 3D nanowire array

2.2.3 Device fabrication

For a 3D device (Figure 2.4), a thin film (~100 nm) of AZO was coated by RF magnetron sputtering on soda lime glass substrate. Zinc oxide nanowires (5 µm, *n*-type) were grown on the AZO film, and further embedded by either dropping CZTS nanocrystals ink (200 mg/mL) on the nanowires or by PLD technique. For the second technique, a custom made PLD system was used for filling ZnO nanowires interstitial space with CZTS. A Nd:YAG pulsed laser with a wavelength of 1064 nm and a repetition rate of 10 Hz was focused on a sintered CZTS target placed inside a 1 inch quartz tube connected to a vacuum pump. The substrate was placed in front of the target and heated to 450˚C. The target was initially ablated for 3 hours at 27 mJ/cm^2, followed by 15 min at 32 mJ/cm^2. Finally, a top electrode of Molybdenum (Mo) was RF

sputtered using a bilayer process on the surface of the absorber material to complete the device. First the chamber was evacuated to a base pressure of $5x10^{-6}$ Torr, which was then increased to 10 mTorr using Ar partial pressure. 5 nm of Mo (100W) were initially sputtered at 10 mTorr, followed by 1 µm of Mo at 2 mTorr to achieve a low sheet resistance film.

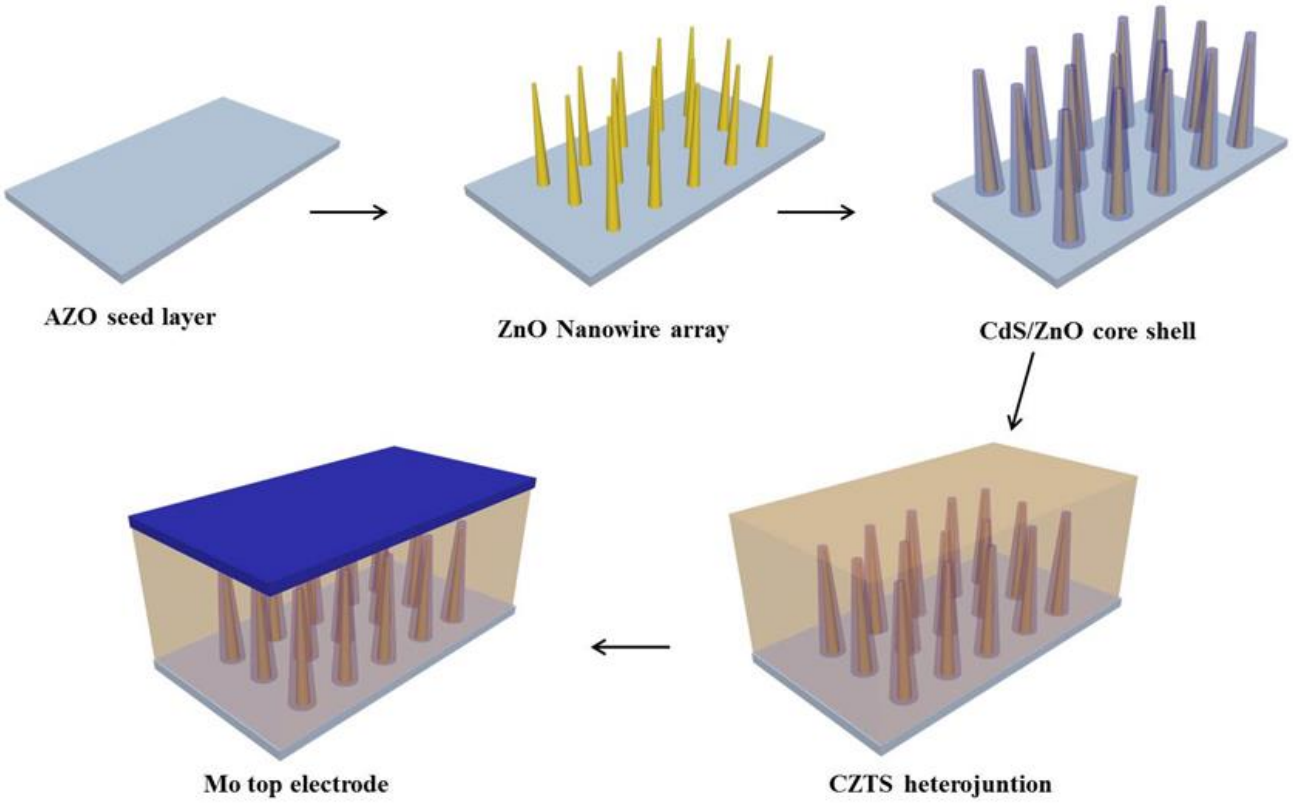

Figure 2. 4. Schematic summarizing the device fabrication process

2.2.4 Material characterizations

A Carl Zeiss 1530 VP field emission scanning electron microscope (FESEM) and a Tecnai G2 20 transmission electron microscope (TEM) equipped with EDS were used to characterize the morphology of the synthesized nanostructures. The crystallinity and purity of the samples were examined by X-ray diffraction (XRD) using a Philips X-ray diffractometer equipped with graphite-monochromated Cu Kα radiation at λ = 1.541 Å, and a confocal Raman microscope (DXR Thermo Scientific). The photocurrent−voltage (*JV*) characteristic of

CZTS/ZnO 3D nanostructured solar cells were measured with a Newport solar cell simulator (Model 9119X) equipped with a 150 W Xenon lamp under simulated AM 1.5G illumination (light irradiation of 100 $mW.cm^{-2}$).

2.3 Results and discussion

2.3.1 Working principle

In this 3D nanostructure solar cell design, we use an "inverse' configuration compare to the classical 2D thin film device. The inverse structure relies on the use of nanowire array (ZnO), which can potentially reduce the charge recombination at the interfaces between the *p*- and *n*-type materials due to the reduced lateral travel distance for the minority carriers, which would decrease the defect trapping problem and thus increase the solar cell efficiency. Additionally, the use of a nano-junction between ZnO and CZTS would potentially increase the *pn*-junction surface area while decreasing the amount of material needed for the fabrication of the device, which ultimately would provide devices with increased efficiency at a lower cost.

2.3.2 CZTS nanocrystals

One of the limitations concerning the growth of kesterite CZTS nanocrystals is the lack of thermodynamic studies. In addition, the characterization of the samples is not straightforward due to the similar crystallographic structures between CZTS and some spurious phases, such as ZnS, Cu_xS, SnS_2, which degrade the quality of the final absorber layer. The CZTS nanocrystals were characterized by several means in order to substantiate the purity of the kesterite structure. Figure 2.5a represents a characteristic XRD for CZTS nanocrystals which is confirmed by the presence of the major diffraction peaks (112), (200), (220), and (312) of the

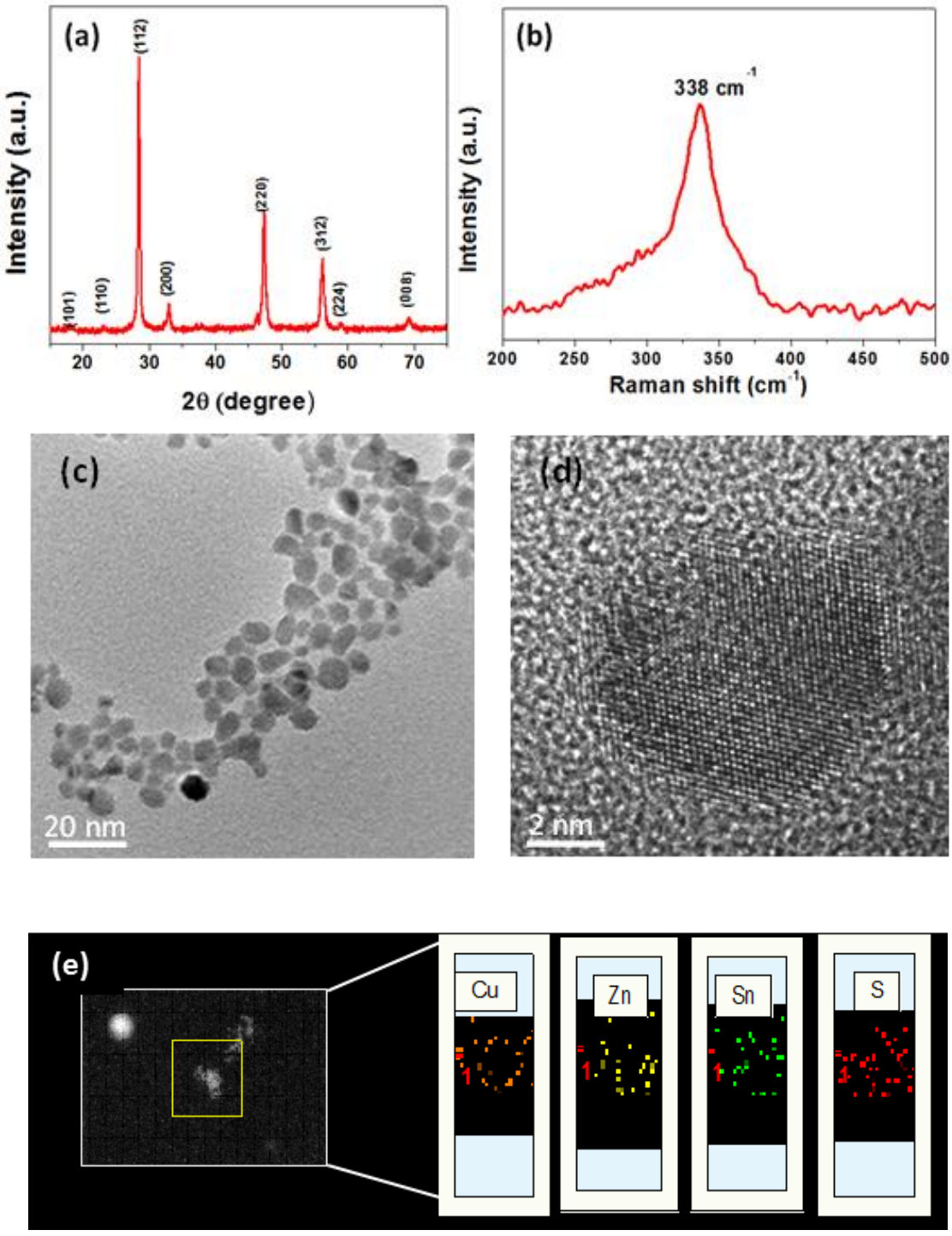

Figure 2. 5. (a) X-Ray diffraction pattern and (b) Raman spectrum of CZTS sample; (c) Low Magnification TEM image and (d) HRTEM of CZTS nanocrystals. (e) EDS Mapping of a CZTS nanoparticle.

CZTS kesterite structure. These results are in good agreement with the value reported in the literature, [30-32] as well as the Powder Diffraction File 26-0575 of the International Center for Diffraction Data. Additionally, the single-phase nature of the sample was further confirmed by Raman spectrum. As shown in Figure 2.5b, the characteristic peak of a pure CZTS phase, centered at 338 cm-1 was observed. The nanocrystals were further characterized by transmission electron microscopy (TEM). Figure 2.5c shows a typical low magnification TEM image of well dispersed and quasi uniform CZTS nanoparticles with a diameter in the range of 7~15 nm. A high resolution electron microscopy (HREM) image of a single CZTS nanocrystal also reveals the inter-planar d_{112} spacing of 3.1Å, further confirming the nature of the nanocrystals as CZTS (Figure 2.5d). An energy dispersive x-ray (EDX) mapping of an individual CZTS nanoparticle (Figure 2.5e) demonstrates the repartition of the elements is uniformly distributed in the nanocrystal. As a result, it is apparent to conclude that the as-synthesized nanocrystals are pure CZTS, which can be used for further device fabrication.

2.3.3 ZnO nanowires

The *n*-type part of the junction is engineered by ZnO nanowires on an AZO seed layer. This transparent conducting oxide layer, with an n^+- type conductivity, allows the wavelength to be transmitted to the *p*-type absorber layer. The conductive behavior of the seed layer is strongly correlated to its number of oxygen vacancies, percentage of Aluminum doping, and its thickness. A 100 nm seed layer is thick enough to provide a good conductivity, but thin enough to maintain a good transparency.[42, 43] Moreover; this thickness is optimum to provide a solid growth site for the ZnO nanowires (a wide band gap semiconductor (3.37 eV at RT) with wurtzite structure.

It is colorless and clear in the near UV.[44] Figure 2.6a is a top-view FESEM image of the AZO seed layer after annealing. The thin film shows a uniform and smooth surface which grain size about 15 to 50nm. The ZnO nanowires were synthesized on the AZO/soda lime glass. Initially, $Zn(NO_3)_2$ and HMT were mixed with DI water. The reactions occurred following equation (1) and (2). $Zn(NO_3)_2$ and HTM were reacted and hydrated, providing respectively Zn^{2+} and OH^- to the solution.

$$\mathbf{(CH_2)_6N_4 + H_2O \xrightarrow{\Delta} 4NH_3\,(g) + 6HCHO(g)\ (1)}$$

$$\mathbf{NH_3 + H_2O \rightarrow NH_4{+} + OH^-\ (2)}$$

When the precursor solution was further heated, Zn^{2+} reacted easily with OH^- to form more soluble $Zn(OH)_2$ complexes (equation (3)), which were decomposed to form ZnO nanostructures (equation (4)).

$$\mathbf{Zn^{2+} + 2OH\text{-} \leftrightarrow Zn(OH)_2(s)\ (3)}$$

$$\mathbf{Zn(OH)_2 \leftrightarrow ZnO(s) + H_2O\ (4)}$$

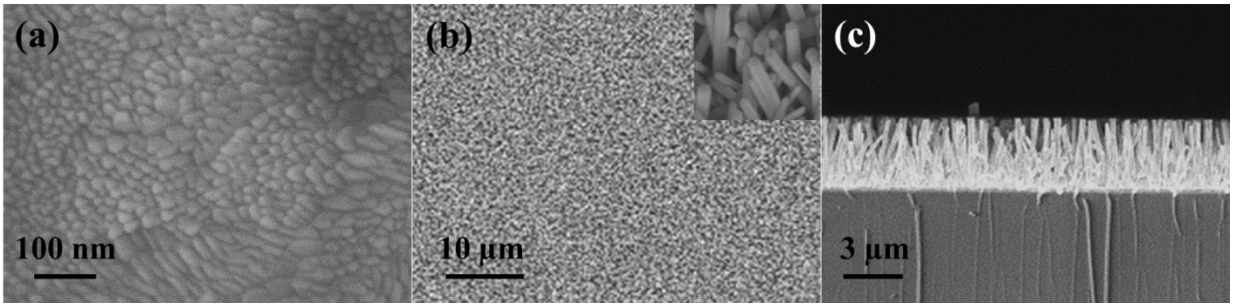

Figure 2. 6. (a) FESEM image of the AZO seed layer deposited by RF magnetron sputtering, (b) Large area FESEM image of ZnO nanowire array grown by hydrothermal method on the AZO seed layer, the inset shows a higher magnification image of the same nanowires exhibiting a diameter around 80~200 nm, and (c) is the cross sectional image of the ZnO nanowires with a length about 5µm.

The concentration of ZnO increased until super-saturation, where ZnO crystal nuclei were formed and led to the growth of the nanowires.45 Figure 2.6b shows a typical low-magnification FESEM image of as-synthesized large-area ZnO nanowire array. Most ZnO nanowires exhibit tapered morphologies and diameters that are in the range of 80~300 nm, as shown in the inset of Figure 2.6b. The cross sectional FESEM images of the ZnO nanowire array, as shown in Figure 2.6c, demonstrates a successful c-oriented growth with length ~5 μm.

2.3.4 Formation of *pn*-junction

2.3.4.1 Formation of *pn*-junction using CZTS nanocrystal ink

However, controlling the density of the ZnO nanowires arrays synthesized by hydrothermal route seems to be difficult because of no effective way to control the growth of seed layer. As a consequence, fully filling the nanocrystal ink among the nanowires became difficult by using conventional solution method, such as dropping the ink onto the nanowire array, immersing the nanowires inside the ink, spin coating, etc.

Figure 2.7a shows a top view FESEM image of ZnO nanowires filled with CZTS nanocrystals by drop coating method. The top view reveals the tip of the nanowires seems well embedded in the ink, however, they were barely coated at their roots from cross-sectional view (Figure 2.7b). However, solution method is still considered as a fast and low cost method for large scale PV device fabrication. Therefore, it is necessary to find a way to effectively space the ZnO nanowires to accommodate the CZTS nanocrystals filling. It has been reported that e-beam nanolithography (EBNL) is a very effective way to generate patterns for directing growth of ZnO nanowire array.[46,47] In our experiment, EBNL was employed to make a PMMA mask on top of the ZnO seed layer. Figure 2.7c is a FESEM image of the mask pattern fabricated using EBNL.

After patterning, hydrothermal growth was performed, as shown in Figure 2.7d and e. The nanowires were well spaced with cactus-like growth, providing enough space for CZTS nanocrystals to be filled. Figure 2.7f is the top view micrograph of ZnO nanowire array half-filled with CZTS nanocrystals, showing ZnO nanowire roots have been fully covered, compared to the one without EBNL patterning.

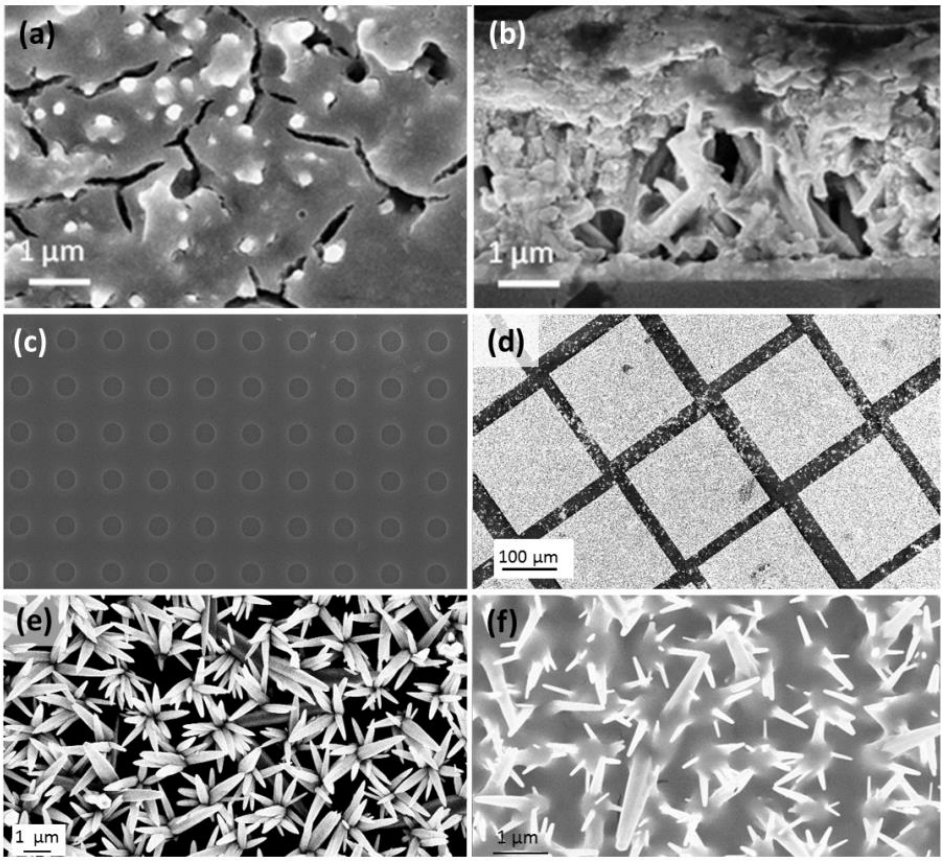

Figure 2. 7. (a) top view and (b) cross-sectional FESEM image of ZnO nanowires filled with CZTS nanocrystals by drop coating method, (c) FESEM top view image of ITO substrate patterned by e-beam nanolitography, (d) low magnification FESEM image of hydrothermally grown ZnO nanowires using PMMA mask. (e) and (f) FESEM top view image of the ZnO nanowires before and after being filled with CZTS nanocrystals

Using this way, we are able to control the spacing of the nanowire as well as the quality of the filling for large scale device fabrication in the future. But the drawback for this method is one has to spend long time for EBNL patterning, especially for large scale patterning. The preliminary device was workable with measured conversion efficiency of 0.004% though it is low.

2.3.4.2 Formation of *pn*-junction using PLD method

Alternatively, the coating can be done more efficiently using PLD method to fill dense ZnO nanowires. The pulse of laser allowed the diffusion of CZTS nanocrystals in small and confined spaces. In Figure 2.8b, a dense ZnO nanowires array was successfully coated with CZTS nanocrystals after the deposition (27 mJ/cm^2) for 3 hrs.

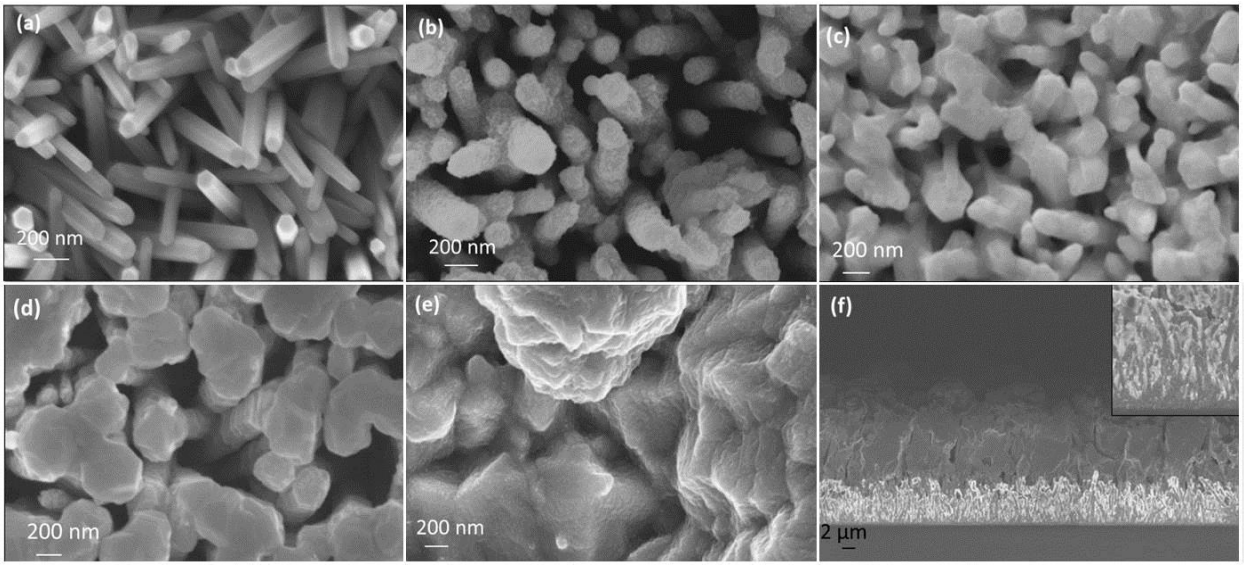

Figure 2. 8. FESEM image of CZTS coating by PLD on ZnO nanowires array at different time and power of deposition: a. bare ZnO nanowires; b. 3h at 27 mJ/cm^2; c. 5 min at 32 mJ/cm^2 ; d. 10 min at 32 mJ/cm^2 ; e. and f. 15 min at 32 mJ/cm^2

From the image, it can be seen that the surface of the nanowires were well coated with a rough surface. By extending the deposition time and power (15 min at 32 mJ/cm^2), the CZTS coating became thicker and smoother as shown in a top view FESEM image in Figure 2.8c-e. Figure 2.8c, d and e are FESEM images of the nanowires after 5, 10 and 15 min of deposition at higher energy. The cross sectional microscopy image on Figure 2.8f confirms that the space between the nanowires is nearly fully filled, forming a thick and flat film for the further deposition of Molybdenum ohmic contact by RF sputtering.

However, ink methods are still preferable as fast and low cost methods for large scale PV device fabrication. Therefore, it is necessary to find a way to effectively space the ZnO nanowires to accommodate the CZTS nanocrystal filling.

2.3.4.3 Device assembly

A Molybdenum (Mo) metal electrode was RF sputtered on the surface of the device following a bilayer process.[48] First the chamber was evacuated to a base pressure of 5x10^{-6} Torr, which was then increased to 10 mTorr using Argon partial pressure. Once the plasma was stable, Mo (100W) was sputtered on the absorber layer for 2 min in order to form an adhesion layer, and then the pressure in the chamber was gradually changed to reach a low pressure state (2 mTorr) to achieve a low sheet resistance film with a final thickness of 1µm. The bilayer sputtering process revealed to be critical, to avoid peeling off of the Mo metallic electrode. Figure 2.9a is top view and (b) cross section FESEM image of Mo metal electrode. The Mo film exhibit a rough surface with texture around 100 nm. The XRD spectrum in Figure 2.9c shows the high crystallinity of the Mo electrode.

2.3.4.4 Device characterization

The device characterization was performed by measurements of current density-voltage *(JV)* curves under dark and simulated sun light. The *JV* curves measured under sun-light were collected under 100 $mW.cm^{-2}$ (AM1.5) simulated solar irradiation. The power conversion efficiency of a typical CZTS/ZnO nanostructured solar cells can reach up to 0.4%. Although, the devices are workable, the low photovoltaic parameters are attributed to the preliminary structure of the nanostructured devices where the efficiency of the device is strongly affected by the property, spacing and length of the nanowires, the quality of the coating layer and contacts, and a buffer layer (absence) between *pn*-junction. These issues are currently being investigated in order to obtain higher efficiency devices.

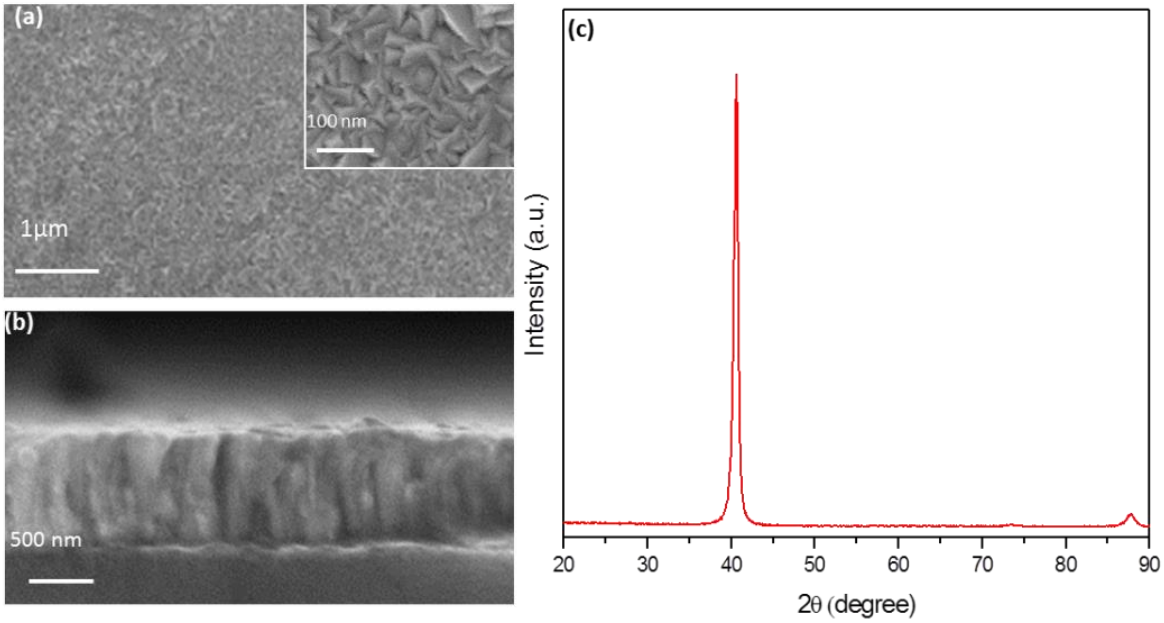

Figure 2. 9. (a) Top view and (b) cross section FESEM image of Mo metal electrode, and (c) XRD spectrum of the Mo electrode.

2.4 Conclusions

A 3D architecture using CZTS nanocrystals and ZnO nanowire arrays for inorganic heterojunction solar cell applications was proposed. The use of a 3D nano-junction would potentially reduce the charge carrier recombination at the interfaces in the device, and the amount of material needed while increasing the device efficiency. Here, CZTS nanocrystals were synthesized by pulsed laser deposition method and simultaneously used to fill the interstitial space of previously synthesized ZnO nanowires array. The PLD method proved to be an excellent technique to coat the nanowires. Further, the characterization of the CZTS nanocrystals proved the purity of the semiconductor. The device, however, has low conversion efficiency due to a preliminary structure. Solutions such as a CdS buffer layer to enhance the *pn*-junction, an optimization of the absorber layer in the device are expected to significantly improve the device efficiency.

2.5 References

(1) Sawin, J. L.; Sverrisson, F. *Renewable 2014 Global Status Report*, 2014.

(2) Fan, C. C.; United States Energy Information Administration: 2012.

(3) Green, M. A. *Physica E: Low-dimensional Systems and Nanostructures* **2002**, *14*, 65.

(4) Park, J. H.; Lee, T.-W.; Kang, M. G. *Chemical Communications* **2008**, 2867.

(5) Han, J.; Fan, F.; Xu, C.; Lin, S.; Wei, M.; Duan, X.; Wang, Z. L. *Nanotechnology* **2010**, *21*, 405203.

(6) Tian, B.; Zheng, X.; Kempa, T. J.; Fang, Y.; Yu, N.; Yu, G.; Huang, J.; Lieber, C. M. *Nature* **2007**, *449*, 885.

(7) Fan, Z.; Razavi, H.; Do, J.-w.; Moriwaki, A.; Ergen, O.; Chueh, Y.-L.; Leu, P. W.; Ho, J. C.; Takahashi, T.; Reichertz, L. A.; Neale, S.; Yu, K.; Wu, M.; Ager, J. W.; Javey, A. *Nat Mater* **2009**, *8*, 648.

(8) Zhu, J.; Yu, Z.; Fan, S.; Cui, Y. *Materials Science and Engineering: R: Reports* **2010**, *70*, 330.

(9) Fan, Z.; Kapadia, R.; Leu, P. W.; Zhang, X.; Chueh, Y.-L.; Takei, K.; Yu, K.; Jamshidi, A.; Rathore, A. A.; Ruebusch, D. J.; Wu, M.; Javey, A. *Nano Letters* **2010**, *10*, 3823.

(10) Garnett, E.; Yang, P. *Nano Letters* **2010**, *10*, 1082.

(11) Lin, C.; Povinelli, M. L. *Opt. Express* **2009**, *17*, 19371.

(12) Lu, Y.; Lal, A. *Nano Letters* **2010**, *10*, 4651.

(13) Spurgeon, J. M.; Atwater, H. A.; Lewis, N. S. *The Journal of Physical Chemistry C* **2008**, *112*, 6186.

(14) Bao, H.; Ruan, X. *Opt. Lett.* **2010**, *35*, 3378.

(15) Baek, S.-H.; Jang, H. S.; Kim, J. H. *Current Applied Physics* **2011**, *11*, S30.

(16) Tian, B.; Zheng, X.; Kempa, T. J.; Fang, Y.; Yu, N.; Yu, G.; Huang, J.; Lieber, C. M. *Nature* **2007**, *449*, 885.

(17) Kuang, Y.; van der Werf, K. H. M.; Houweling, Z. S.; Schropp, R. E. I. *Applied Physics Letters* **2011**, *98*, 113111.

(18) Wang, K.; Rai, S. C.; Marmon, J.; Chen, J.; Yao, K.; Wozny, S.; Cao, B.; Yan, Y.; Zhang, Y.; Zhou, W. *Nanoscale* **2014**, *6*, 3679.

(19) Greenham, N. C.; Grätzel, M. *Nanotechnology* **2008**, *19*, 420201.

(20) Yu, M.; Long, Y.-Z.; Sun, B.; Fan, Z. *Nanoscale* **2012**, *4*, 2783.

(21) Lee, S. H.; Zhang, X. G.; Parish, C. M.; Lee, H. N.; Smith, D. B.; He, Y.; Xu, J. *Advanced Materials* **2011**, *23*, 4381.

(22) Camacho, R. E.; Morgan, A. R.; Flores, M. C.; McLeod, T. A.; Kumsomboone, V. S.; Mordecai, B. J.; Bhattacharjea, R.; Tong, W.; Wagner, B. K.; Flicker, J. D.; Turano, S. P.; Ready, W. J. *JOM* **2007**, *59*, 39.

(23) Kayes, B. M.; Atwater, H. A.; Lewis, N. S. *Journal of Applied Physics* **2005**, *97*, 114302.

(24) Todorov, T. K.; Tang, J.; Bag, S.; Gunawan, O.; Gokmen, T.; Zhu, Y.; Mitzi, D. B. *Advanced Energy Materials* **2012**, n/a.

(25) Ito, K.; Tatsuo, N. *Jpn. J. Appl. Phys.* **1988**, *27*, 2094.

(26) Wozny, S.; Wang, K.; Zhou, W. *Journal of Materials Chemistry A* **2013**, *1*, 15517.

(27) Ramasamy, K.; Malik, M. A.; O'Brien, P. *Chemical Communications* **2012**, *48*, 5703.

(28) Shin, B.; Gunawan, O.; Zhu, Y.; Bojarczuk, N. A.; Chey, S. J.; Guha, S. *Progress in Photovoltaics: Research and Applications* **2011**, n/a.

(29) Todorov, T. K.; Reuter, K. B.; Mitzi, D. B. *Advanced Materials* **2010**, *22*, E156.

(30) Riha, S. C.; Parkinson, B. A.; Prieto, A. L. *J. Am. Chem. Soc.* **2009**, *131*, 12054.

(31) Steinhagen, C.; Panthani, M. G.; Akhavan, V.; Goodfellow, B.; Koo, B.; Korgel, B. A. *J. Am. Chem. Soc.* **2009**, *131*, 12554.

(32) Guo, Q.; Ford, G. M.; Yang, W.-C.; Walker, B. C.; Stach, E. A.; Hillhouse, H. W.; Agrawal, R. *J. Am. Chem. Soc.* **2010**, *132*, 17384.

(33) Khare, A.; Wills, A. W.; Ammerman, L. M.; Norris, D. J.; Aydil, E. S. *Chemical Communications* **2011**, *47*, 11721.

(34) Scragg, J. J.; Berg, D. M.; Dale, P. J. *Journal of Electroanalytical Chemistry* **2010**, *646*, 52.

(35) Jeon, M.; Shimizu, T.; Shingubara, S. *Materials Letters* **2011**, *65*, 2364.

(36) Su, Z.; Yan, C.; Tang, D.; Sun, K.; Han, Z.; Liu, F.; Lai, Y.; Li, J.; Liu, Y. *CrystEngComm* **2012**, *14*, 782.

(37) Singh, A.; Geaney, H.; Laffir, F.; Ryan, K. M. *J. Am. Chem. Soc.* **2012**, *134*, 2910.

(38) Shi, L.; Pei, C.; Xu, Y.; Li, Q. *J. Am. Chem. Soc.* **2011**, *133*, 10328.

(39) Lévy-Clément, C.; Tena-Zaera, R.; Ryan, M. A.; Katty, A.; Hodes, G. *Advanced Materials* **2005**, *17*, 1512.

(40) Moriya, K.; Tanaka, K.; Uchiki, H. *Jpn. J. Appl. Phys.* **2007**, *46*, 5780.

(41) Greene, L. E.; Law, M.; Tan, D. H.; Montano, M.; Goldberger, J.; Somorjai, G.; Yang, P. *Nano Letters* **2005**, *5*, 1231.

(42) Kemell, M.; Ritala, M.; Leskelä, M. *Critical Reviews in Solid State and Materials Sciences* **2005**, *30*, 1.

(43) Johnston, D. *Solar Energy* **2010**, *84*, 384.

(44) Ladanov, M.; Ram, M. K.; Matthews, G.; Kumar, A. *Langmuir* **2011**, *27*, 9012.

(45) Qiu, J.; Li, X.; He, W.; Park, S.-J.; Kim, H.-K.; Hwang, Y.-H.; Lee, J.-H.; Kim, Y.-D. *Nanotechnology* **2009**, *20*, 155603.

(46) Kurihara, K.; Iwadate, K.; Namatsu, H.; Nagase, M.; Takenaka, H.; Murase, K. *Jpn. J. Appl. Phys.* **1995**, *34*, 6940.

(47) Pease, R. F. W.; AVS: 1992; Vol. 10, p 278.

(48) Cho, Y. K.; Kim, G. S.; Song, Y. S.; Lim, T. H.; Jung, D. *Thin Solid Films* **2013**, *548*, 162.

Chapter 3 Synthesis of CZTS nanoplate array for dye-sensitized solar cell applications*

3.1 Introduction

Dye sensitized solar cells (DSSCs) have been developed into one of the most attractive third generation photovoltaic devices, with easy fabrication and relatively high conversion efficiency.[1] A typical DSSC is composed of three parts: a dye-sensitized semiconductor photoanode, an electrolyte, and a counter-electrode. So far, titanium dioxide (TiO_2) nanostructured photoanodes are the most promising semiconductor materials in DSSCs to promote electrons from the ground state to an excited state, in the dyes,[2-4] and then transfer them to the conduction band of the photoanodes. Different dyes have been investigated to absorb broader bands to improve the light absorption.[5-8] High electrocatalytic activity for efficient reduction of the charge carriers in the electrolyte is also indispensable,[9,10] which requires a high quality counter electrode with a good electronic conduction. Generally, platinum (Pt) is used as a counter electrode, where electrons from the external circuit are collected and catalyse the reduction of the redox electrolyte.[11] However, catalytic materials with low cost, low toxicity and environmental abundance are always highly favoured to replace Pt (scarce and expensive) despite its high conductivity and good electrocatalytic activity.

In the past several years, considerable efforts have been made to replace this precious metal by using abundant and low cost materials.[12] Previous studies have reported the use of various materials as possible candidates for non-platinum-based counter-electrodes.

*This chapter was adapted from: Wozny, S.; Wang, K.; Zhou, W., Cu_2ZnSnS_4 nanoplate arrays synthesized by pulsed laser deposition with high catalytic activity as counter electrodes for dye-sensitized solar cell applications *J. Mater. Chem. A*, **2013**, 1, 15517-15523

For instance, carbon materials (graphene, graphite, carbon nanotubes, active carbon, etc.)[13-18] were chosen for their high surface area and low cost. Conductive polymers (poly(3,4-ethylenedioxythiophene) (PEDOT), polypyrrole (PPy), polyaniline (PANI), etc.)[19-23] were studied for their stability and high catalytic activity. Other inorganic materials (nitrides, carbides, oxides, Cu_2S, PbS, $CuInS_2$, etc.) [22,24-30] were also investigated for their abundance and diversity, including quaternary chalcogenide Cu_2ZnSnS_4 (CZTS).

CZTS was first found as a p-type semiconductor with suitable properties for solar cell applications.[31-34] The advantages of this quaternary semiconductor are its earth-abundance and ideal direct band gap of ~1.5 eV and its high absorption coefficient ($> 1 \times 10^{-4}$ cm^{-1}),[35] enabling a wide range of applications, such as light absorber material for thin film photovoltaics,[32,33] thermoelectric material,[34] etc. Recently, Xin *et al*. spin-coated CZTS nanocrystal ink to form a thin film directly on fluorine doped tin oxide (FTO) glass[36] as an efficient counter-electrode for DSSC photocathode and the thin film exhibited both high electrocatalytic activity comparable to Pt and efficient reduction of I_3^- in the electrolyte. Following this work, porous CZTS thin film,[37] and porous[38] and hierarchical[39] CZTS microspheres were also employed to fabricate efficient counter-electrodes, further confirming the high catalytic activity of CZTS as a counter electrode obtained by Xin *et al*. However, most of the above materials rely on wet chemistry syntheses and inevitable post-treatments, such as washing, annealing, etc., to remove the excessive ligands, which are time consuming and may affect the final performance of the CZTS DSSC counter-electrodes.

To overcome this barrier, we have used a physical method to synthesized CZTS nanostructures. Pulsed laser deposition (PLD) technique was used to grow vertically oriented CZTS nanoplate array directly on FTO glass substrate by a simple one step synthesis.

The two-dimensional (2D) vertical nanoplates showed uniform morphology and provide a larger interfacial contact area compared to a compact thin film of the same dimension. In addition, the interfacial contact between the electrolyte and the counter-electrode is enhanced so that the charge transfer to the electrolyte is greatly improved. DSSCs were fabricated using this nanoplate array as counter electrode and showed comparable efficiency to that made of the sputtered Pt counter-electrode.

3.2 Experimental

3.2.1 Synthesis of CZTS nanoplate by PLD

Vertically aligned CZTS nanoplate arrays were directly grown on a clean FTO glass substrate by ablating a CZTS target with a neodymium-doped yttrium aluminium garnet (Nd:YAG) laser in a horizontal tube furnace.[40] Figure 3.1 is a schematic of the homemade PLD system. It consists of a Nd:YAG laser focused through a focus lens on a target, located inside a one inch diameter quartz tube. In this design, the substrate was placed in front of the target inside the quartz tube, which was connected to a vacuum pump in order to control the atmosphere during the ablation process.

The CZTS target was fabricated by solid-state reaction[41]. Cu_2S, ZnS, SnS_2 and S powders were mixed at mol ratio of 0.95:1.05:1:0.02 and were cold pressed to form a 1 cm diameter target. The target was then sealed in an inert quartz tube and annealed at 750°C for 24h. The pellet's surface was polished to ensure and smooth surface before the ablation process.

A small hole was drilled in the glass of the FTO substrate in order to later inject the electrolyte, and the substrate was cleaned in ethanol. The FTO substrate was placed in front of the CZTS target inside the tube (Figure 3.1).

The laser wavelength, energy density, and pulse frequency were fixed at 1064 nm, 31.5 mJ/cm^2, and 10 Hz, respectively. Prior to the laser deposition, the tube was pumped down to 600 mTorr, and flushed with formic gas three times to remove residual oxygen. The system was heated and maintained at 285°C during the ablation process. After about a 17 min deposition, the furnace was naturally cooled down to room temperature.

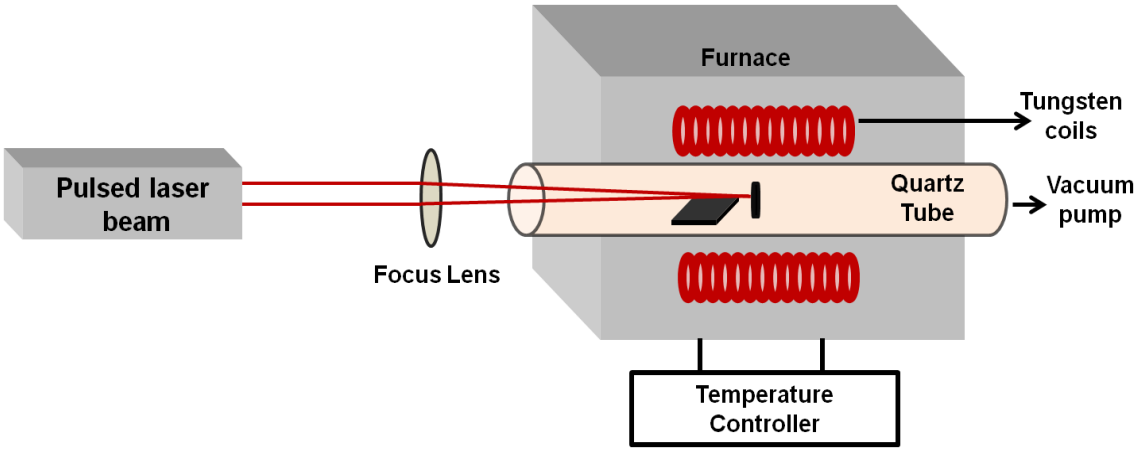

Figure 3. 1. Schematic of the custom made pulsed laser deposition system

3.2.2 Synthesis of CZTS thin film by PLD

CZTS thin films were directly grown on a clean FTO glass substrate by a similar procedure to the one of the CZTS nanoplate array fabrication. The same experimental set-up previously described in Figure 3.1 was used. The CZTS nanoplate array procedure was slightly modify in order to get a compact thin film. Energy density and synthetic temperature are the key parameters for the formation of CZTS nanostructures. The laser wavelength, energy density, and pulse frequency were adjusted to 1064 nm, 34.0 mJ/cm^2, and 10 Hz, respectively. The FTO substrate was placed in front of the target, heated and maintained at 450°C. After about a 10 min deposition, the furnace was naturally cooled down to room temperature. The synthetic

parameters for the growth of CZTS nanoplate array and compact thin film are summarized in Table 3.1.

Table 3. 1. Synthetic parameters for the growth of CZTS films

Parameters	**Nanoplate array**	**Compact thin film**
Laser wavelength (nm)	1064	1064
Energy density (mJ/cm^2)	31.5	34.0
Pulse frequency (Hz)	10	10
Pressure (mTorr)	600	600
Growth temperature (°C)	285	450
Growth time (min)	17	10

3.2.3 Device Fabrication

For a fair comparison, all the DSSCs were fabricated with TiO_2 photoanode materials relying on a standardized fabrication process. A schematic of the device fabrication process is displayed in Figure 3.2. A commercial solution of TiO_2 (Solaronix) was spin-coated on a clean FTO glass, baked for 10 in at 150 °C and immediately annealed for 30 min at 500 °C. The photoanodes were then sensitized in a 0.3 mM *cis*-diisothiocyanato-bis(2,2'-bipyridyl-4,4'(dicarboxylato)ruthenium(II)bis(tetrabutyl-ammonium) ethanolic solution (N 719, Solaronix) for 24 h at room temperature. The cell was assembled with a 75 μm spacer (Surlyn) and backfilled with an iodine electrolyte (acetonitrile, DMPII (1mM), LiI (0.1M), I_2 (0.12 M), and terbutylpyridine (0.5 M)).

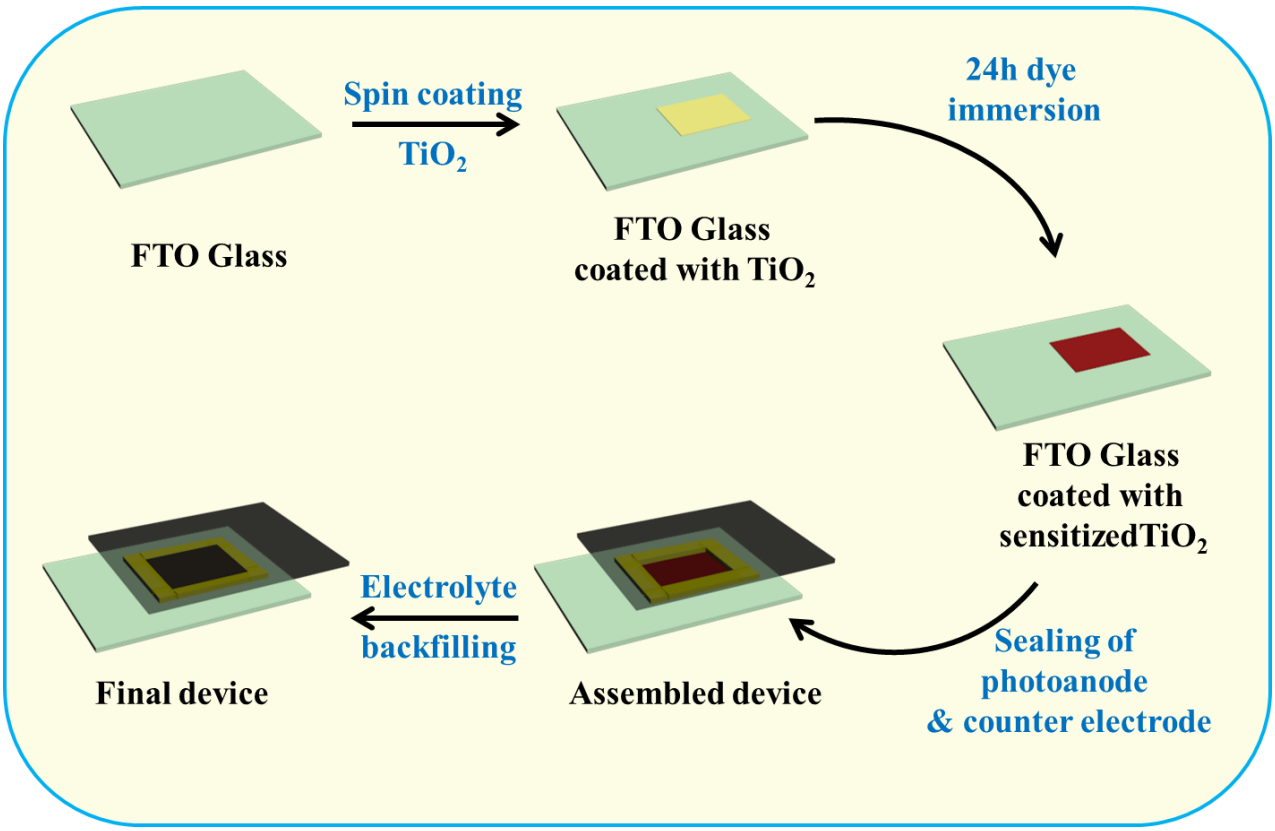

Figure 3. 2. Schematic of DSSC fabrication process

3.2.4 Material characterization

The crystallinity and purity of the samples were examined by X-ray diffraction (XRD) using a Philips X-ray diffractometer equipped with graphite-monochromated Cu Kα radiation at λ = 1.541 Å, and a confocal Raman microscope (DXR Thermo Scientific). Carl Zeiss 1530 VP field emission scanning electron microscope (FESEM) was used to characterize the morphology of the synthesized nanostructures. The detailed nanostructures were investigated using JEOL 2010 transmission electron microscopy (TEM). The elemental mapping of the nanoplates and high resolution imaging was carried out using FEI Tecnai F30 TEM equipped with Oxford electron dispersive spectroscopy (EDS). The elemental composition was further characterized by

X-ray photoelectron spectroscopy (XPS) (Perkin-Elmer Phi 560 XPS/Auger System). A Newport solar cell simulator (Model 9119X) equipped with a 150 W Xenon lamp (light irradiation of 100 mW/cm^2) was employed to measure the *JV* curves of the devices. Electrochemical impedance was measured on a Gamry potentiostat (Series G™ 300), with the frequency range of 0.1 Hz ~ 100 kHz and a perturbation amplitude of 10 mV.

3.3 Results and discussion

3.3.1 Nanoplate array characterization

The nanoplate array grown by PLD is shown in the FESEM image in Figure 3.3. Figure 3.3a presents a large area of vertically aligned nanoplates, uniformly distributed over an area of 1 cm × 1 cm FTO glass substrate. Nanoplates with a petal-like shape and about 20 nm thickness are clearly seen in a zoom-in image, as shown in Figure 3.3b. In our growth, it was found that nanoplates were always grown out from a seed layer formed during the first 5 min ablation of the target, on the surface of the FTO glass (Figure 3.3c). The seed layer consists of CZTS nanocrystalline clustered grains with inhomogeneous sizes ranging from 300-700 nm, as shown in the inset in Figure 3c. Figure 3d is a TEM image of the grains found in the seed layer. The nanocrystal size varies from 20 to 50 nm and shows inhomogeneous morphologies. The structure of the nanoplates was further investigated by TEM (Figure 3.4). A top view image of a cluster of CZTS nanoplates, peeled off from the seed layer, can be clearly seen in Figure 3.4a, confirming that the thickness (~20 nm) of the nanoplates is the same as observed by FESEM. A side view of two nanoplates lying on top of a carbon TEM grid (Figure 3.4b) reveals the height of the

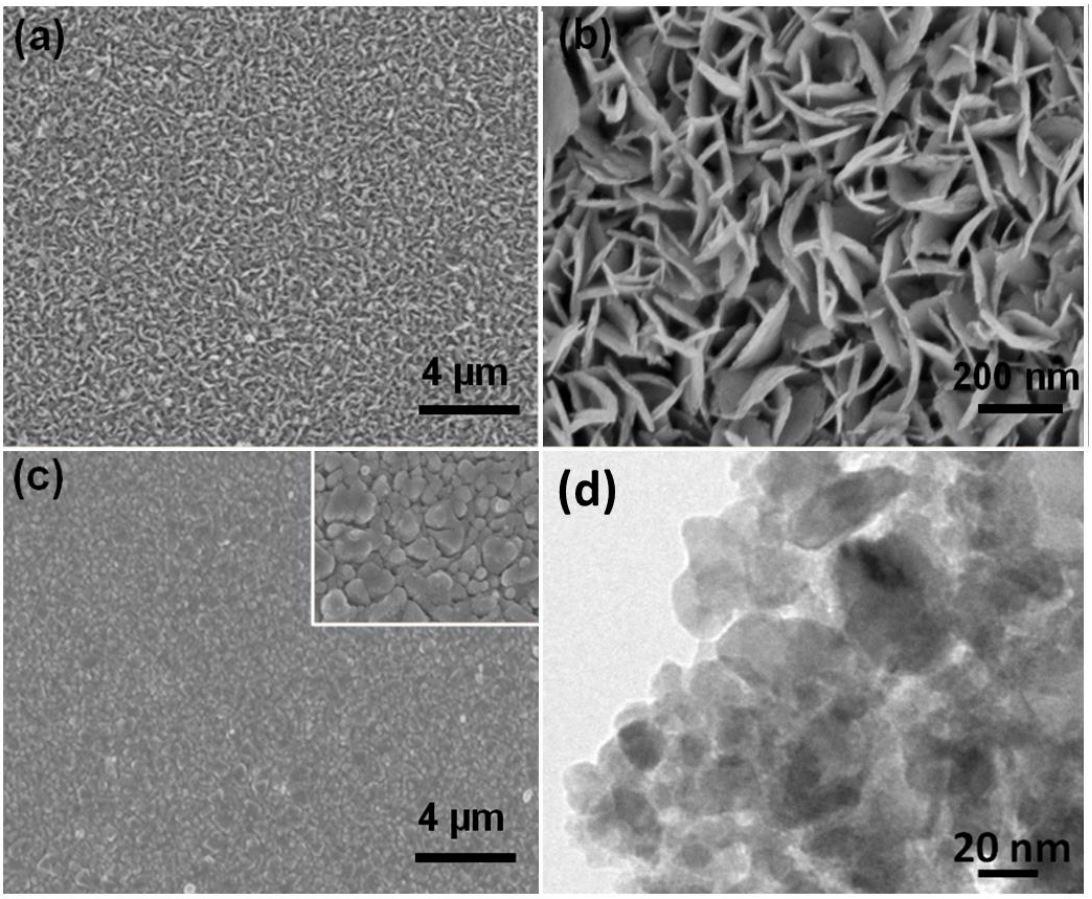

Figure 3. 3. (a) and (b) show FESEM images of vertically aligned CZTS nanoplate array at low and high magnifications, (c) FESEM image of the granular CZTS thin film acting as a seed layer for the growth of the nanoplates, the inset shows a zoom-in image of the film, and (d) TEM image of a cluster of CZTS nanocrystals with a size of about 20-50 nm, which act as the seed layer for the growth of the CZTS nanoplate array.

nanoplates is about 300 nm. The selected area electron diffraction (SAED) pattern of the nanoplates, correspond to the polycrystalline CZTS kesterite structure (simulated with the PCED2.0 program)[42] with the presence of the major diffraction rings (112), (200), (220), and (312), is indexed in Figure 3.4c, which are in good agreement with those reported in the literature.[43] No apparent additional phases were observed, which will be further confirmed by

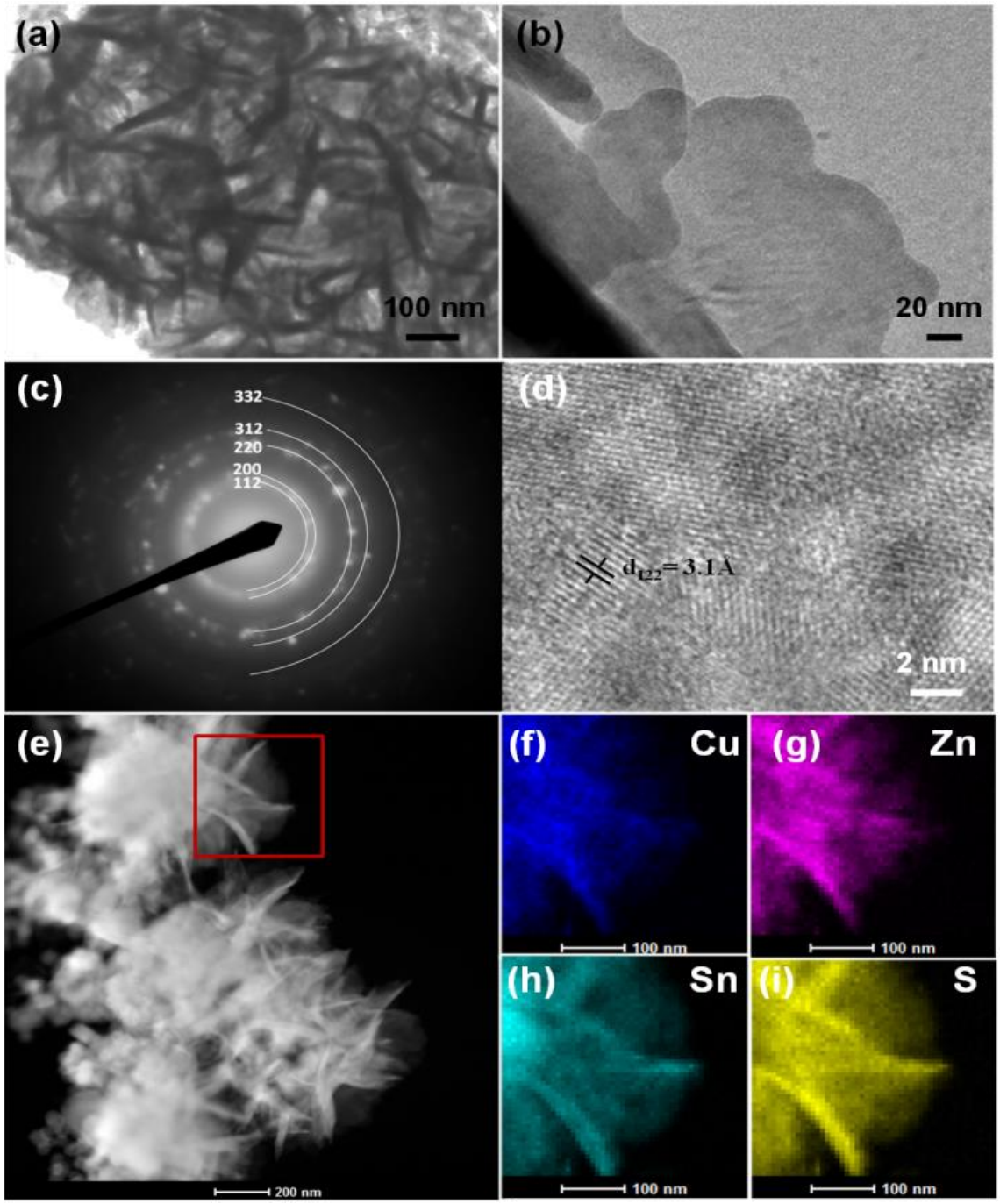

Figure 3. 4. (a) Top view TEM image of a cluster of CZTS nanoplates array, (b) Side view TEM image of two single CZTS nanoplates lying on the carbon film of the TEM grid, (c) Selected area diffraction pattern (SADP) of CZTS nanoplate with a polycrystalline structure, (d) High resolution TEM image of a nanoplate showing different grain sizes and orientations, and (e) STEM image of nanoplates, (f) Cu, (g) Zn, (h) Sn, and (i) S elemental EDS mappings of CZTS nanoplates highlighted in the rectangular area in (e).

XRD and Raman data later on. A high resolution electron microscopy image (HREM) (Figure 3.4d) of the nanoplate also shows the feature of polycrystalline nanocrystals, where the (112) lattice fringes can be clearly observed. The CZTS nanocrystals present inhomogeneous size distributions with diameters ranging from several to tens of nanometers. Figure 3.4e is a scanning transmission electron microscopy (STEM) image of an additional cross-sectional view of a cluster of CZTS nanoplates grown out from the seed film. EDS mappings were performed in the rectangular area highlighted in Figure 3.4e, revealing the coexistence of copper, zinc, tin and sulfur in the nanoplates, as shown in Figure 3.4f-i, respectively. It appears that all the elements are homogeneously distributed over the whole area of the nanoplates. By quantitatively analysing the EDS data collected from different locations on the nanoplates, the elemental composition of CZTS nanoplates was calculated to be $Cu_{1.62}Zn_{1.33}Sn_{1.31}S_{3.74}$, showing a Cu deficient and Zn rich CZTS kesterite phase.

The XRD was also employed in structural analysis. As shown in Figure 3.5a, the XRD data of a pure FTO substrate (lower) and the CZTS nanoplate array, prepared on a FTO glass substrate (upper), are presented. Besides the FTO peaks from the substrate, the other peaks, denoted by stars, can be clearly indexed as (112), (220), (312), and (008), planes of CZTS kesterite pure phase (JCPDS No. 26-0575), which correspond with those reported by others.[44] Raman spectrum in Figure 3.5b further authenticates the nature of the kesterite phase with a single peak at 331cm^{-1}, consistent with previously published results (331-338 cm^{-1}).[39,45-47] No impurity peaks were observed both in XRD and Raman spectrum, confirming the high purity of the CZTS nanoplates.

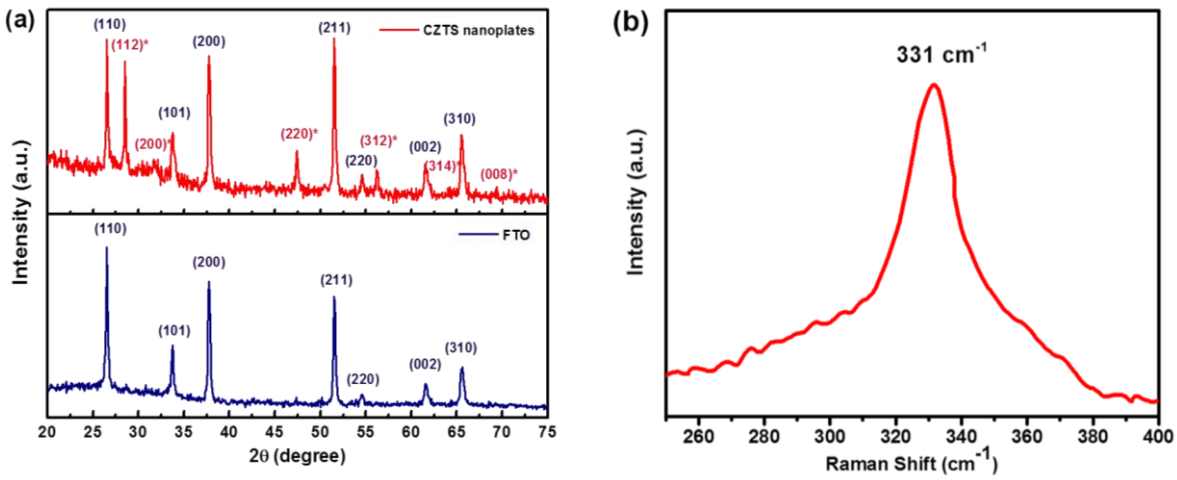

Figure 3. 5. (a) Powder XRD pattern of FTO glass susbtrate (lower) and CZTS nanoplate array (upper), which clearly shows (112), (220), (312), and (008) characteristic peaks of CZTS kesterite phase and (b) Raman scattering analysis of the nanoplates with a single peak at 331 cm^{-1}, consistent with a pure kesterite phase.

Moreover, XPS was used to verify the oxidation states of the four elements in the CZTS nanoplate sample by characterizing the Cu 2p, Zn 2p, Sn 3d, and S 2p core levels. In the Cu 2p spectrum (Figure 3.6a), there are two peaks located at 952.02 and 932.28 eV, respectively, with a separation of 19.74 eV, indicating the presence of Cu^{+}. Zn 2p core level spectrum clearly shows that two peaks appear at 1045.12 and 1022.11 eV with a characteristic peak separation of 23.01 eV (Figure 3.6b), revealing the formation of Zn^{2+}. In the Sn 3d core level (Figure 3.6c), two peaks are found at 494.51 and 486.15 eV, respectively, corresponding to Sn^{4+} oxidation state with a characteristic binding energy of 8.36 eV. Finally, two peaks at 162.60 eV and 161.42 eV with a peak separation of 1.14 eV, in the S 2p spectrum (Figure 3.6d), are also seen, which is in good agreement with the values reported for S.[39]

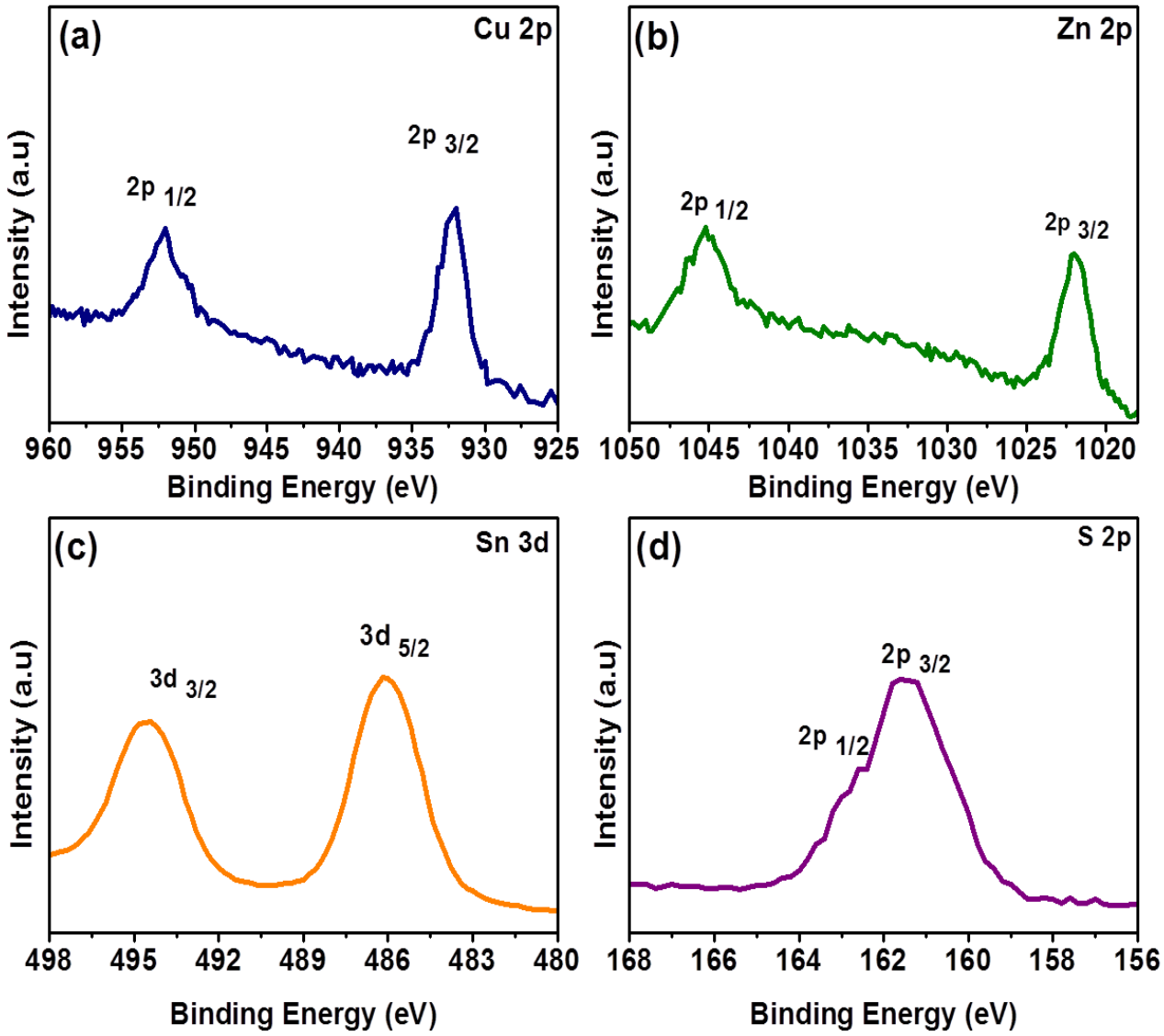

Figure 3. 6. High-resolution XPS analysis of the four constituent elements of the vertically oriented CZTS nanoplates: (a) copper 2p, (b) zinc 2p, (c) tin 3d, and (d) sulfur 2p in good agreement with the literature.

3.3.2 Influence of growth parameters

In our study, a two-step growth, namely seed layer growth and vertically aligned nanoplate formation, was observed. During the first 5 min of PLD ablation, a thin seed layer of CZTS nanocrystalline clustered grains with sizes between 300 and 700 nm were formed. The

granular thin film, composed of 20-50 nm nanocrystals (Figure 3.3d), acts as seed layer for initiating the perpendicular nanoplate growth.

In our experiments, several synthesis parameters had been changed to study the nanoplate formation. First, when the temperature was varied from 150°C to 350°C, no dramatic change of the vertically aligned nanoplate growth was observed. The pressure of the growth was also tuned from 600 mTorr to 1400 mTorr and proved to be a critical parameter for the vertical alignment and growth of the nanoplates array. At 600 mTorr, the nanoplates exhibit a vertical and uniform growth from the seed layer over a large area (Figure 3.7a), however, when the pressure is change to 1000 mTorr the nanoplates have a tendency to lose their alignment and growth in a coral-like shape at random positions in the array (Figure 3.7b).

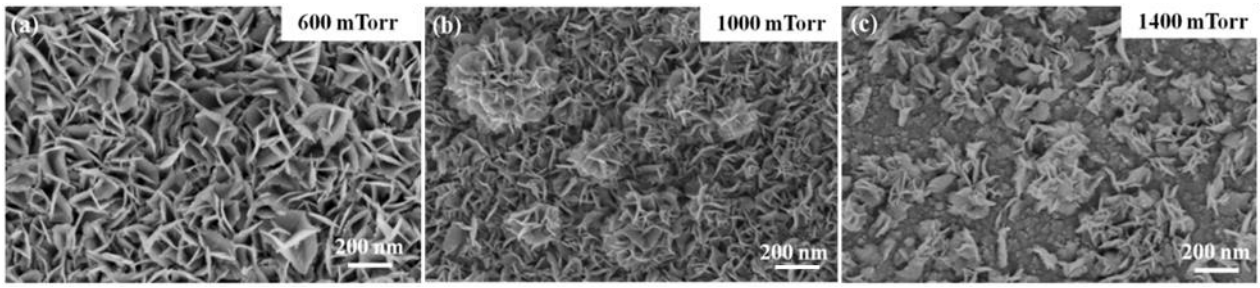

Figure 3. 7. (a) FESEM image of the vertically aligned CZTS nanoplate array synthesized by PLD at 600 mTorr, (b) FESEM image of the nanoplate array synthesised at 1000 mTorr. The nanoplates tend to lose their alignment and growth in a coral-like shape at random positions in the array, and (c) FESEM image of the nanoplate synthesized at 1400 mTorr, in which the growth of the nanoplates is irregular and suppressed.

Further changing the pressure to 1400 mTorr resulted in sparse and irregular growth of the nanoplates. As observed in Figure 3.7c, only few nanoplates are able to grow on the substrate and present random orientation. Additionally, it was found that the laser beam energy was a very

sensitive parameter for the nanoplate growth and the nanoplates were only formed in the energy range between 30 to 32 mJ/cm^2. Thus far, we haven't fully understood why the perpendicular nanoplate formation was initiated after the CZTS granular seed layer thickness reached a certain value (~100 nm). However, we believe, first, the CZTS seed layer thickness and morphology are critical for the nanoplate formation, and, second, the beam energy associated with producing the ablation plume to a specific partial pressure inside the tube determines if the beam can initiate this vertical nanoplate growth.

3.3.3 CZTS thin film characterization

For comparison purpose, a CZTS film (~0.5 μm) similar to the height of nanoplate array was also prepared by increasing the laser energy to 34 mJ/cm^2 and temperature to 450°C. The FESEM images of top and plane views of the CZTS thin film (Figure 3.8a and b) reveal a uniform surface and homogeneous thickness of the thin film with inhomogeneous grain sizes. No cracks or voids are visible on the top view and cross-sectional images. In addition, EDS was performed on the sample (Figure 3.8c) and confirm the presence of Cu, Zn, Sn and S. The XRD was also employed in structural analysis in Figure 3.9a.

The XRD data of a standard CZTS sample (lower) and the CZTS thin film prepared on a FTO glass substrate (upper) are presented. The major diffraction peaks for CZTS can be clearly indexed as (112), (200), (220), (312), (224) and (008) planes of CZTS kesterite pure phase (JCPDS No. 26-0575), which correspond with those reported previously and by others.[44] The CZTS thin film do not show the presence of the FTO peaks on the XRD data due to the overall thickness of the film which is higher than the penetration depth of the x-rays. The nature of the kesterite phase was further authenticated with Raman spectroscopy. Figure 3.9b shows a single

CZTS characteristic peak at 333cm^{-1}, consistent with previously published results (331-338 cm^{-1}).[39,45-47] As for the nanoplate array, no impurity peaks were observed both in XRD and Raman spectrum, confirming the high purity of the CZTS thin film.

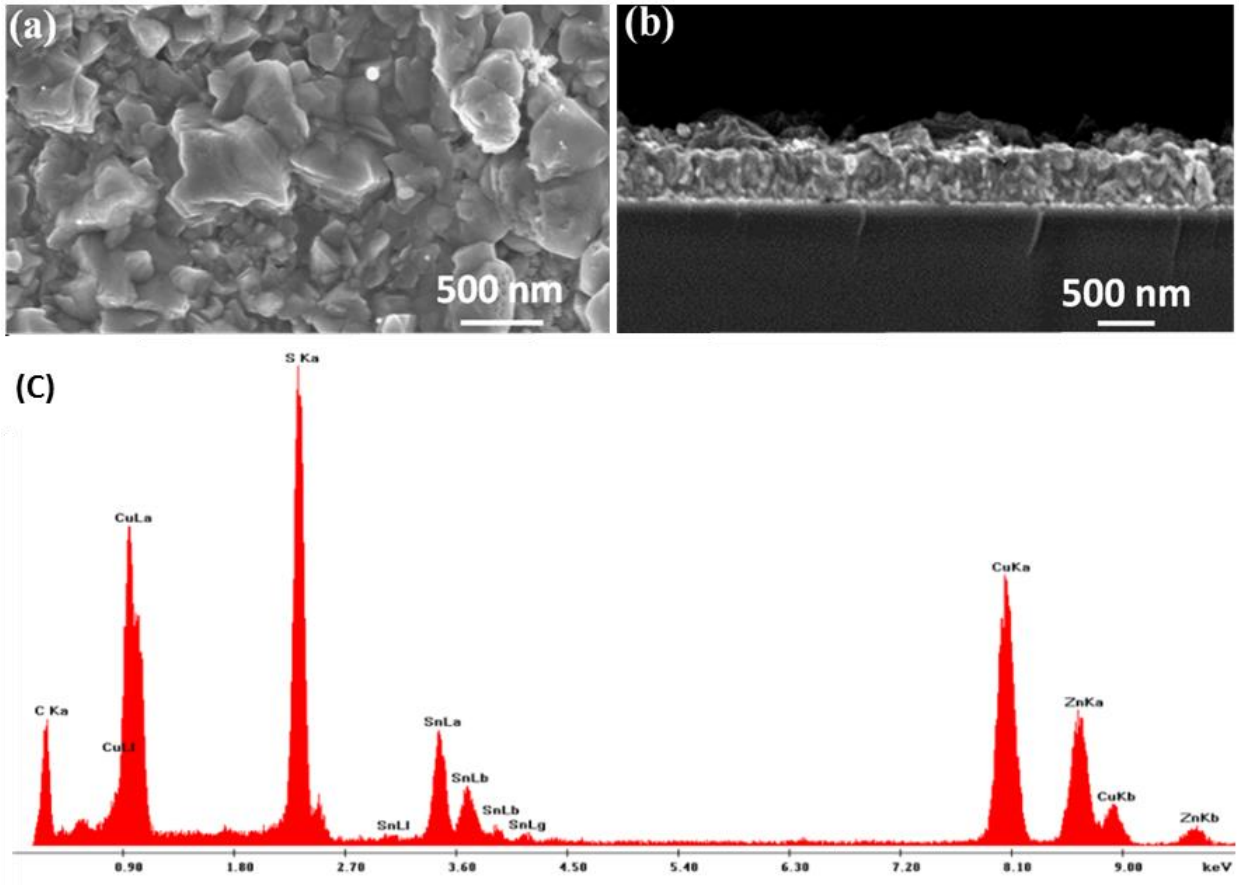

Figure 3. 8. (a) Top view FESEM image, (b) Cross sectional FESEM image of the CZTS thin film synthesized by pulsed laser deposition (34mJ/cm^{-2}, 450°C) with a similar height as the nanoplates (about ∼0.5 μm), and (c) EDS spectrum of CZTS thin film.

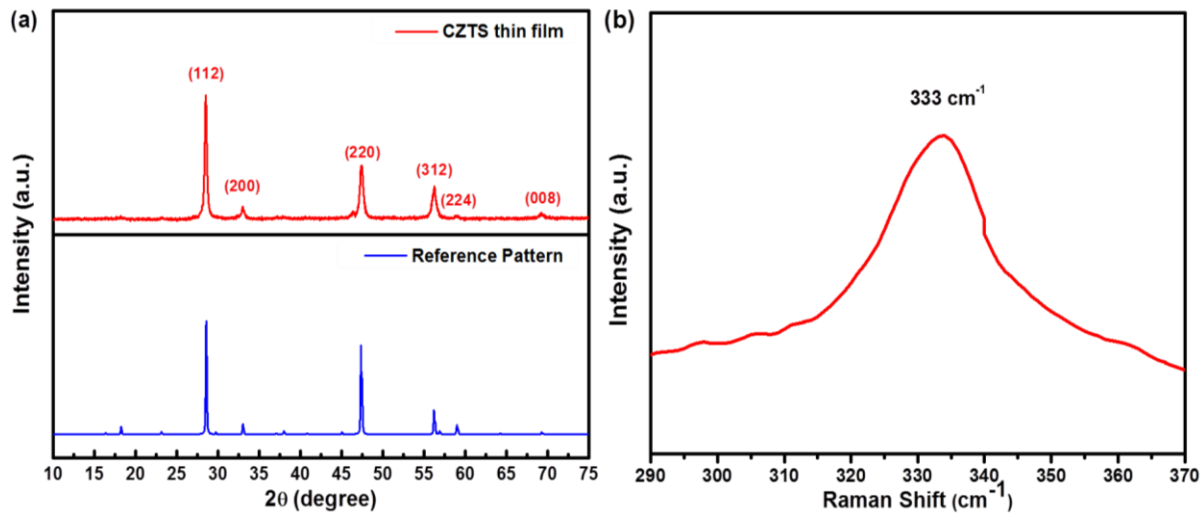

Figure 3. 9. (a) Powder XRD data of the CZTS thin film, which clearly shows (112), (220), (312), and (008) characteristic peaks of CZTS kesterite phase, compared to CZTS reference spectrum JCPDS No. 26-0575 (lower spectrum), and (b) Raman spectrum of the same CZTS thin film with a single peak at 333cm^{-1}, consistent with a pure kesterite phase.

3.3.4 Device characterization and performance

To estimate the photovoltaic performance and electrocatalytic activity of the CZTS nanoplate films versus Pt counter electrodes, DSSC devices were fabricated. For comparison purpose, a CZTS film (~ 0.5 μm) similar to the height of nanoplate array was also prepared. Figure 3.10 shows the current density-voltage (*JV*) performances of three typical DSSCs; and their characteristic parameters are summarized in Table 3.2. The cell based on the CZTS nanoplate array counter electrode presents the best efficiency (3.65%) with a short current density of 10.27 mA·cm^{-2} and a fill factor of 0.55, which is slightly higher than the cell fabricated with a standard Pt counter electrode, with an efficiency and short circuit density of 3.33% and 8.72 mA·cm^{-2}, respectively.

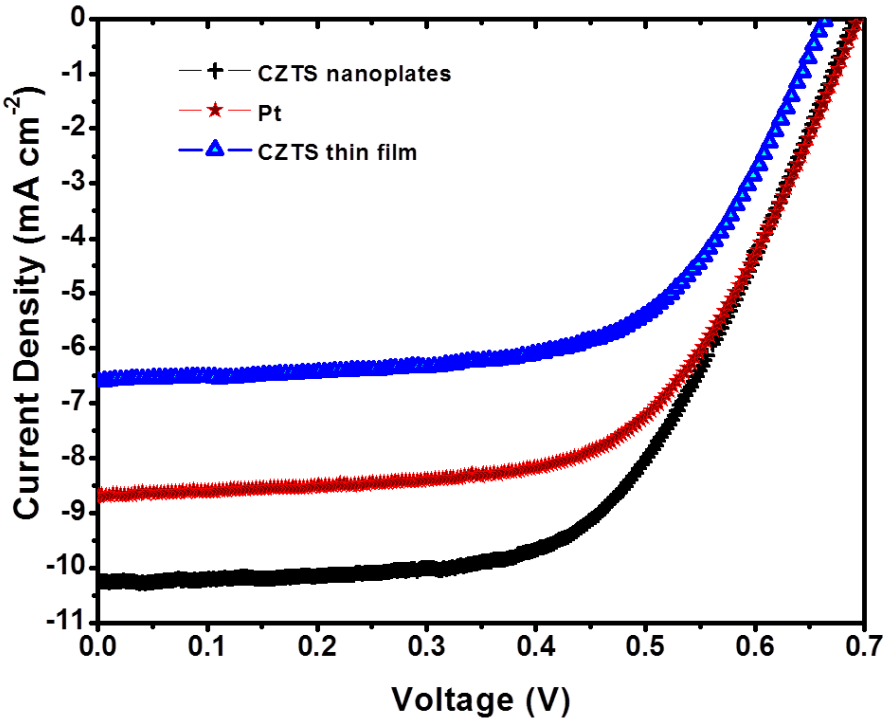

Figure 3. 10. Photocurrent–voltage characteristics of DSSCs containing the same photoanode of TiO_2 nanospheres and various counter electrodes of Pt/FTO, CZTS nanoplates/FTO, and CZTS thin film/FTO.

When the CZTS film (0.5 μm) was employed and measured, the efficiency of the cell only reached to 2.83%. The higher efficiency using the CZTS nanoplate film might be attributed to the ligand free PLD synthesis as well as the large surface area of vertically aligned nanoplates, which provides more catalytic cycles for the reduction of the redox couple in the electrolyte. The effect of the photo-activity of CZTS is not believed to influence the short-circuit current of the device for the reason mentioned above, further the sensitized TiO2 and the electrolyte absorb most of the incident light, and only a very small portion could potentially reach CZTS and contribute to the reduction of the electrolyte, which would not be reflected by such a large increase in the efficiency of the DSSCs. However its effect cannot be totally rule out. As for the CZTS thin film solar cell, the lower efficiency might be resulted from less surface area compared

to the nanoplate array, which didn't significantly improve the efficiency as the thickness increased.

Table 3. 2. Summary of Current density-voltage (*JV*) performances of three typical DSSCs; and their impedance parameters.

Counter Electrode	**Jsc ($mA\ cm^{-2}$)**	**Voc (V)**	**FF**	**η (%)**	**Rs (Ω)**	**Rct (Ω)**
CZTS thin film	6.66	0.65	0.53	2.83	18.27	14.44
CZTS nanoplate array	10.27	0.68	0.55	3.65	18.01	3.96
Sputtered Pt	8.72	0.69	0.54	3.33	15.70	5.38

Electrochemical impedance spectroscopy (EIS) experiments were carried out to further characterize the electrocatalytic activity of the various counter electrodes. A dummy cell with a symmetric sandwich-like (CE/electrolyte/CE) configuration for each type of counter-electrodes was adopted in order to acquire Nyquist plots. An impedance measurement was obtained by applying a fixed DC current to a device while scanning the frequency at a multitude of values over several decades (from 0.1 Hz to 100 kHz). Nyquiest plots were fitted with an equivalent circuit (Figure 3.11) where Rs represents the series resistance, Rct the charge transfer resistance, Zw the Nernst diffusion impedance, and CPE the constant phase angle element at the electrolyte/counter electrode interface. Rs is defined by the high frequency intercept on the real axis (Z'axis). The semi-circle in the high and low frequencies represent the Rct value and the CPE at the electrolyte/counter electrode interface, and Nernst diffusion impedance of the

triiodide/iodide couple in the electrolyte, respectively. All the electrochemical impedance data were extracted using Gamry Echem Analyst software and summarized in Table 3.2.

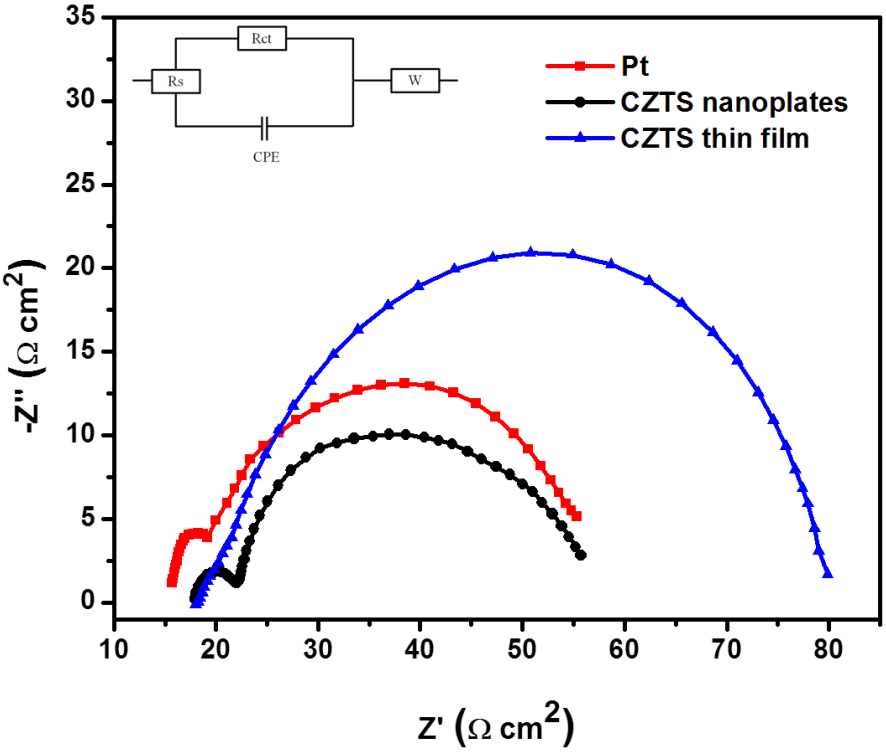

Figure 3. 11. Nyquist plots of solar cells containing symmetric cells of Pt/FTO, CZTS nanoplates/FTO, and CZTS thin film/FTO.

The large and similar Rs value for the CZTS thin film (18.27Ω) and CZTS nanoplate array (18.01Ω) counter electrodes can be attributed to the poorer conductivity of CZTS compared to metallic Pt (15.70 Ω). The higher Rct value for the CZTS thin film cell (14.44 Ω) might be caused by less catalytic sites compared to the nanoplate array. The Rct for CZTS nanoplate array (3.96Ω) is in the same range as Pt (5.38Ω) , but smaller, implying that the reduction of the electrolyte at the interface is faster than that for Pt, further proving that this three-dimensional nanoplate array is a good candidate for Pt free counter electrode fabrication in DSSCs.

3.4 Conclusions

In summary, we have synthesized ligand free and vertically aligned CZTS nanoplates directly on FTO glass substrate by a one-step PLD method. The formation process of the nanoplates was controlled by a two-step growth, where a seed layer was first formed directly on the surface of the substrate, followed by the nanoplate array growth. The nanoplate arrays were used as counter electrodes in DSSCs, demonstrating higher electrocatalytic activity and efficiency comparable to those of Pt counter electrodes, which opens the possibilities of developing low cost and environmentally friendly counter electrode for DSSCs.

3.5 References

(1) Baxter, J. B. *J. Vac. Science & Tech, A: Vacuum, Surfaces, and Films* **2012**, *30*, 020801.

(2) Lee, B. H.; Song, M. Y.; Jang, S.-Y.; Jo, S. M.; Kwak, S.-Y.; Kim, D. Y. *J. Phys. Chem. C* **2009**, *113*, 21453.

(3) Sahu, G.; Wang, K.; Gordon, S. W.; Zhou, W.; Tarr, M. A. *RSC Adv.* **2012**, *2*, 3791.

(4) Tricoli, A.; Wallerand, A. S.; Righettoni, M. *J. Mater. Chem.* **2012**, *22*, 14254.

(5) Kwon, T.-H.; Armel, V.; Nattestad, A.; MacFarlane, D. R.; Bach, U.; Lind, S. J.; Gordon, K. C.; Tang, W.; Jones, D. J.; Holmes, A. B. *J. Org. Chem* **2011**, *76*, 4088.

(6) Hsieh, C.-P.; Lu, H.-P.; Chiu, C.-L.; Lee, C.-W.; Chuang, S.-H.; Mai, C.-L.; Yen, W.-N.; Hsu, S.-J.; Diau, E. W.-G.; Yeh, C.-Y. *J. Mater. Chem.* **2010**, *20*, 1127.

(7) Mai, C.-L.; Huang, W.-K.; Lu, H.-P.; Lee, C.-W.; Chiu, C.-L.; Liang, Y.-R.; Diau, E. W.-G.; Yeh, C.-Y. *Chem. Commun.* **2010**, *46*, 809.

(8) Kim, H.-S.; Lee, J.-W.; Yantara, N.; Boix, P. P.; Kulkarni, S. A.; Mhaisalkar, S.; Grätzel, M.; Park, N.-G. *Nano Lett.* **2013**.

(9) Kalaignan, G. P.; Kang, M.-S.; kang, Y. S. *Solid State Ionics* **2006**, *177*, 1091.

(10) Wu, J.; Hao, S.; Lan, Z.; Lin, J.; Huang, M.; Huang, Y.; Li, P.; Yin, S.; Sato, T. *J. Am. Chem. Soc.* **2008**, *130*, 11568.

(11) Grätzel, M. *J. Photochem. Photobiol., C* **2003**, *4*, 145.

(12) Ahmad, S.; Yum, J.-H.; Butt, H.-J.; Nazeeruddin, M. K.; Grätzel, M. *ChemPhysChem* **2010**, *11*, 2814.

(13) Xu, F.; Chen, J.; Wu, X.; Zhang, Y.; Wang, Y.; Sun, J.; Bi, H.; Lei, W.; Ni, Y.; Sun, L. *J. Phys. Chem. C* **2013**, *117*, 8619.

(14) Roy-Mayhew, J. D.; Bozym, D. J.; Punckt, C.; Aksay, I. A. *ACS Nano* **2010**, *4*, 6203.

(15) Veerappan, G.; Bojan, K.; Rhee, S.-W. *ACS Appl. Mater. Interfaces* **2011**, *3*, 857.

(16) Yue, G.; Wu, J.; Lin, J.-Y.; Xiao, Y.; Tai, S.-Y.; Lin, J.; Huang, M.; Lan, Z. *Carbon*.

(17) Ramasamy, E.; Lee, W. J.; Lee, D. Y.; Song, J. S. *Electrochem. Commun.* **2008**, *10*, 1087.

(18) Imoto, K.; Takahashi, K.; Yamaguchi, T.; Komura, T.; Nakamura, J.-i.; Murata, K. *Sol. Energy Mater. Sol. Cells* **2003**, *79*, 459.

(19) Yeh, M.-H.; Lee, C.-P.; Chou, C.-Y.; Lin, L.-Y.; Wei, H.-Y.; Chu, C.-W.; Vittal, R.; Ho, K.-C. *Electrochim. Acta* **2011**, *57*, 277.

(20) Chen, J.-G.; Wei, H.-Y.; Ho, K.-C. *Sol. Energy Mater. Sol. Cells* **2007**, *91*, 1472.

(21) Keothongkham, K.; Pimanpang, S.; Maiaugree, W.; Saekow, S.; Jarernboon, W.; Amornkitbamrung, V. *Int. J. Photoenergy* **2012**, *2012*.

(22) Zhang, Z.; Zhang, X.; Xu, H.; Liu, Z.; Pang, S.; Zhou, X.; Dong, S.; Chen, X.; Cui, G. *ACS Appl. Mater. Interfaces* **2012**, *4*, 6242.

(23) Li, Z.; Ye, B.; Hu, X.; Ma, X.; Zhang, X.; Deng, Y. *Electrochem. Commun.* **2009**, *11*, 1768.

(24) Gong, F.; Wang, H.; Xu, X.; Zhou, G.; Wang, Z.-S. *J. Am. Chem. Soc.* **2012**, *134*, 10953.

(25) Zhao, Y.; Burda, C. *Energy Environ. Sci.* **2012**, *5*, 5564.

(26) Santra, P. K.; Kamat, P. V. *J. Am. Chem. Soc.* **2012**, *134*, 2508.

(27) Tachan, Z.; Shalom, M.; Hod, I.; Rühle, S.; Tirosh, S.; Zaban, A. *J. Phys. Chem. C* **2011**, *115*, 6162.

(28) Li, G.-R.; Wang, F.; Jiang, Q.-W.; Gao, X.-P.; Shen, P.-W. *Angew. Chem., Int. Ed.* **2010**, *49*, 3653.

(29) Radich, J. G.; Dwyer, R.; Kamat, P. V. *J. Phys. Chem. Lett.* **2011**, *2*, 2453.

(30) Wu, M.; Lin, X.; Hagfeldt, A.; Ma, T. *Angew. Chem., Int. Ed.* **2011**, *50*, 3520.

(31) Guo, Q.; Ford, G. M.; Yang, W.-C.; Walker, B. C.; Stach, E. A.; Hillhouse, H. W.; Agrawal, R. *J. Am. Chem. Soc.2* **2010**, *132*, 17384.

(32) Fairbrother, A.; García-Hemme, E.; Izquierdo-Roca, V.; Fontané, X.; Pulgarín-Agudelo, F. A.; Vigil-Galán, O.; Pérez-Rodríguez, A.; Saucedo, E. *J. Am. Chem. Soc.* **2012**, *134*, 8018.

(33) Cao, Y.; Denny, M. S.; Caspar, J. V.; Farneth, W. E.; Guo, Q.; Ionkin, A. S.; Johnson, L. K.; Lu, M.; Malajovich, I.; Radu, D.; Rosenfeld, H. D.; Choudhury, K. R.; Wu, W. *J. Am. Chem. Soc.* **2012**, *134*, 15644.

(34) Yang, H.; Jauregui, L. A.; Zhang, G.; Chen, Y. P.; Wu, Y. *Nano Lett.* **2012**, *12*, 540.

(35) Ito, K.; Nakazawa, T. *Jpn. J. Appl. Phys.* **1988**, *27*, 2094.

(36) Xin, X.; He, M.; Han, W.; Jung, J.; Lin, Z. *Angew. Chem., Int. Ed.* **2011**, *50*, 11739.

(37) Dai, P.; Zhang, G.; Chen, Y.; Jiang, H.; Feng, Z.; Lin, Z.; Zhan, J. *Chem. Commun.* **2012**, *48*, 3006.

(38) Du, Y.-F.; Fan, J.-Q.; Zhou, W.-H.; Zhou, Z.-J.; Jiao, J.; Wu, S.-X. *ACS Appl. Mater. Interfaces* **2012**, *4*, 1796.

(39) Xu, J.; Yang, X.; Yang, Q.-D.; Wong, T.-L.; Lee, C.-S. *J. Phys. Chem. C* **2012**, *116*, 19718.

(40) Wang, K.; Chen, J.; Zhou, W.; Zhang, Y.; Yan, Y.; Pern, J.; Mascarenhas, A. *Advanced Materials* **2008**, *20*, 3248.

(41) Moholkar, A. V.; Shinde, S. S.; Agawane, G. L.; Jo, S. H.; Rajpure, K. Y.; Patil, P. S.; Bhosale, C. H.; Kim, J. H. *J. Alloys Compd.* **2012**, *544*, 145.

(42) Li, X. Z. *Ultramicroscopy* **2010**, *110*, 297.

(43) Zhou, Y.-L.; Zhou, W.-H.; Du, Y.-F.; Li, M.; Wu, S.-X. *Mater. Lett.* **2011**, *65*, 1535.

(44) Tanaka, K.; Oonuki, M.; Moritake, N.; Uchiki, H. *Sol. Energy Mater. Sol. Cells* **2009**, *93*, 583.

(45) Khare, A.; Himmetoglu, B.; Johnson, M.; Norris, D. J.; Cococcioni, M.; Aydil, E. S. *J. Appl. Phys.* **2012**, *111*, 083707.

(46) Fernandes, P. A.; Salomé, P. M. P.; da Cunha, A. F. *J. Alloys Compd.* **2011**, *509*, 7600.

(47) Fontané, X.; Izquierdo-Roca, V.; Saucedo, E.; Schorr, S.; Yukhymchuk, V. O.; Valakh, M. Y.; Pérez-Rodríguez, A.; Morante, J. R. *J. Alloys Compd.* **2012**, *539*, 190.

Chapter 4 Fabrication and characterization of high efficiency formamidinum lead triiodide perovskite solar cells

4.1 Introduction

Perovskite is the name given to any compound with ABX_3 structure where "A" and "B" are two cations of various size (A being larger than B) and X is the anion which is bonding them together. Perovskites are naturally occurring minerals, such as calcium titanate ($CaTiO_3$), which were first discovered in 1839 by G. Rose.[1] In 1893, lead and tin halides (such as $CsPbX_3$ with X = Cl, Br or I) were chemically engineered and, only several years later, crystallographically characterized as perovskite materials.[2] Three dimensional organic-inorganic hybrid perovskites were synthesized by replacing cesium by methyl ammonium (MA = $CH_3NH_3^+$) or formamidinium (FA = $CH(NH_2)_2^+$) cations, conferring semiconducting properties to these new materials.[3] They both possess good optical and electrical properties with ideal direct band gaps at 1.55 and 1.47 eV and an absorption edge at 800 and 850 nm, respectively,[4-8] which allow them to absorb photons in both the visible and near-infrared solar spectrum. Further, organic-inorganic halide perovskites demonstrate very interesting properties since they can act as an electron transporter, as well as a hole conductor material.[7,9-13] These dual charge transport properties make these new kinds of perovskites extremely interesting for solar cell applications. The first perovskite solar cell (PSC) was fabricated in 2009 by Kojima *et al.*[14] It was based on a liquid electrolyte dye-sensitized solar cell architecture where $MAPbI_3$ was used as a sensitizer for the metal oxide photoanode. The device demonstrated poor performance due to dissolution of the halides in the electrolyte. The breakthrough for PSCs came in 2012, when solid-state planar heterojunction architecture was employed; suppressing the need for liquid electrolyte, and

devices could reach efficiencies higher than 10%.[11,15-17] Over the last 3 years, the infatuation for PSCs using MA precursors grew bigger. Efficiencies up to 20.1% were obtained by solvent engineering techniques, which marked a fivefold increase in efficiency in just three years.[18] However, to date, experimental work based on FA solar cells was limited to few publications.[5,15,19-25] In 2014, Eperon et al. published the first report on planar heterojunction formamidinium lead trihalide solar cells. In this work, formamidinium was used to narrow the bandgap, and extend the absorption edge by tuning the halide ratio between Bromine and Iodine. Planar heterojunction solar cells were fabricated using single precursor spin-coating route, and demonstrated efficiencies up to 14.2%. This breakthrough rendered formamidinium cations as a viable candidate for PSCs.[5] Despite remarkably high efficiencies obtained within the last three years, PSCs remain as highly unstable without careful fabrication control.[7,13,26-28] It has been shown that PSCs degrade under high temperature due to the decomposition of organic cations and the formation of PbI_2. [26-28] Very few stability studies[26-28] have been done, and the reasons of the decomposition of the perovskite layer remain uncertain. In order for these devices to meet the minimum useful lifetime required for commercialization, it is necessary to understand the underlying cause of their instability by meticulous monitoring of their fabrication condition.

In this chapter, we examine the effect of precursor concentration, solvent engineering technique, and annealing temperature and time on the structural, optical, and electrical properties of $FAPbI_3$ thin films.

All these variables strongly impact the morphological and optical properties of $FAPbI_3$ and the performances of completed devices. A systematic study of these parameters allowed us to refine the fabrication parameters in order to obtain high perovskite solar cell efficiency up to 12.1%.

4.2 Experimental

4.2.1 Synthesis of precursors solution for device fabrication

4.2.1.1 Formamidinium iodide (FAI)

All solvents and reagents were of analytical grade and used as received. In a typical preparation, 25.20g of formamidinium acetate (Aldrich) was added to 250 mL methanol in a 500 mL Erlenmeyer flask that was immersed in a salt/ice bath. 48 mL hydriodic acid (Aldrich, 57 wt % in water, stabilized) was added dropwise at first, then more rapidly. The reaction was left stirring for approximately 2 h at room temperature, and most of the methanol was evaporated on a rotary evaporator. Diethyl ether was added to precipitate the product which was collected by vacuum filtration. The initial yield was 17.3 g (42% yield). It was recrystallized three times from ethanol and dried in a vacuum oven overnight, yielding white crystalline needles of FAI that were immediately transferred into a glovebox for storage. The synthetic process for the fabrication of Formamidinium iodide (FAI) is summarized in Figure 4.1.

4.2.1.2 Formamidinium lead triiodide ($FAPbI_3$)

A 0.7M perovskite solution was prepared from stoichiometric amounts of lead iodide (PbI_2) and FAI in anhydrous N, N'-dimethylformamide (DMF, Sigma Aldrich). The solution was vortexed for 30 min to dissolve PbI_2 and FAI powders in DMF, leading to a clear, bright yellow solution. Finally, the solution was filtered twice using a PTFE 0.45 μm syringe filter to remove any undissolved starting materials.

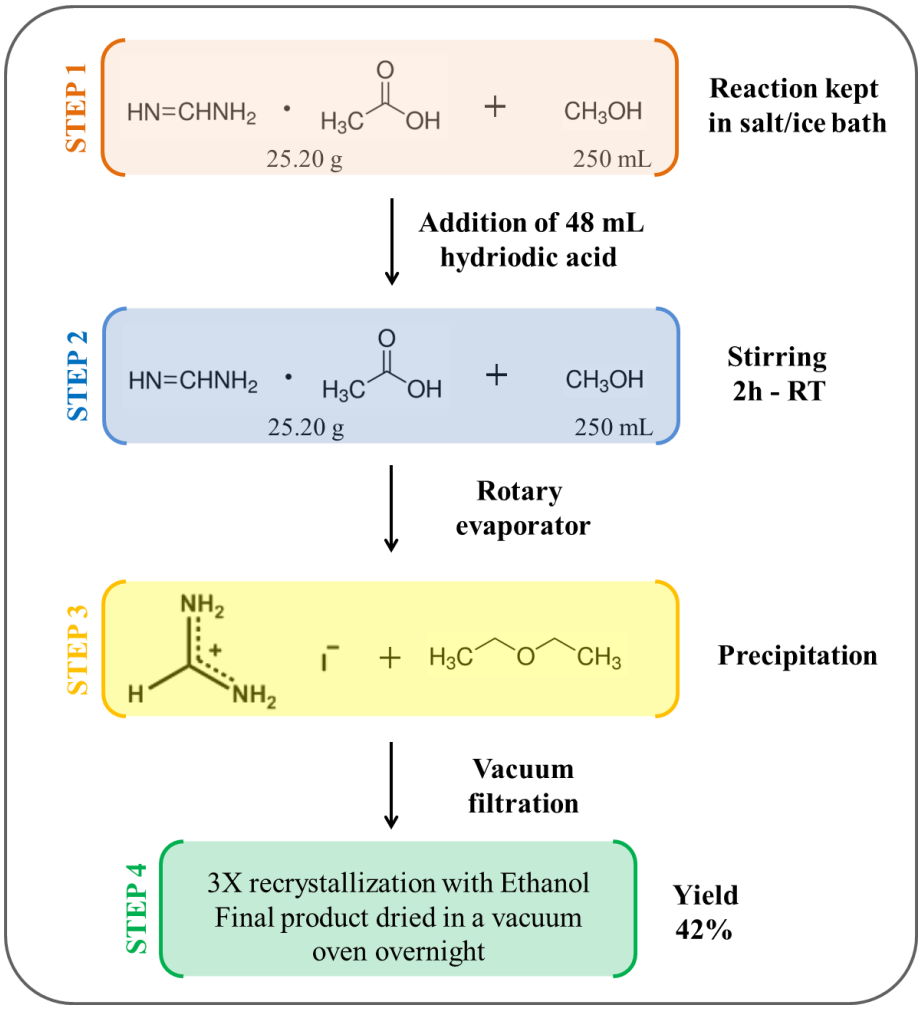

Figure 4. 1. Schematic summarizing the synthetic process of formamidinium iodide (FAI) precursor.

4.2.1.3 2',7,7'-tetrakis(N,N-dip-methoxyphenylamine)-9,9'-spirobifluorene solution (Spiro-OMeTAD)

2',7,7'-tetrakis(N,N-dip-methoxyphenylamine)-9,9'-spirobifluorene solution abbreviated as Spiro-OMeTAD was prepared by adding 80 mg of spiro-OMeTAD, 30µl of bis(trifluoromethane)sulfonimide lithium salt stocking solution (500 mg Li-TFSI in 1 ml

acetonitrile), and 30µl of 4-tert-butylpyridine (TBP) in 1 ml chlorobenzene. The solution was vortexed for 30 min and used immediately.

1.2.1 Substrate preparation

A 1x1 inch Fluorine-doped SnO_2-coated transparent conducting glass (FTO/Glass) substrate was patterned using a 2M HCl solution and Zinc powder.[29] A c-TiO_2 compact blocking layer was spray coated on the hot FTO glass (450°C) using 0.2 M solution of Ti(IV) bis(ethyl acetoacetate)-diisopropoxide in 1-butanol. The spraying process was repeated for 12 cycles, and the substrate was subsequently annealed at 450 °C for 1 hour.[11]

4.2.2 Device fabrication

The devices were fabricated on a bench top using of solvent engineering method. Figure 4.2 summarizes the fabrication process of the perovskite solar cell. Briefly, 100µl of perovskite solution was deposited onto the c-TiO_2/FTO by spin coating.[30] The substrate was spun at 500 rpm for 3 sec to remove excess solution. Rotation was then increased to 3500 rpm and 1 drop of toluene was added to precipitate the perovskite from the solvent exactly 2 seconds before the end of the second spin coating step. The films were dried at 5000 rpm for 30 sec. The substrate was subsequently annealed on a hot plate. The film was cooled for 1 min, before spin coating the spiro-OMeTAD solution on the warm substrate for 30 seconds at 4000 rpm. Finally, silver electrodes were thermally evaporated to evaluate the performance of the device.

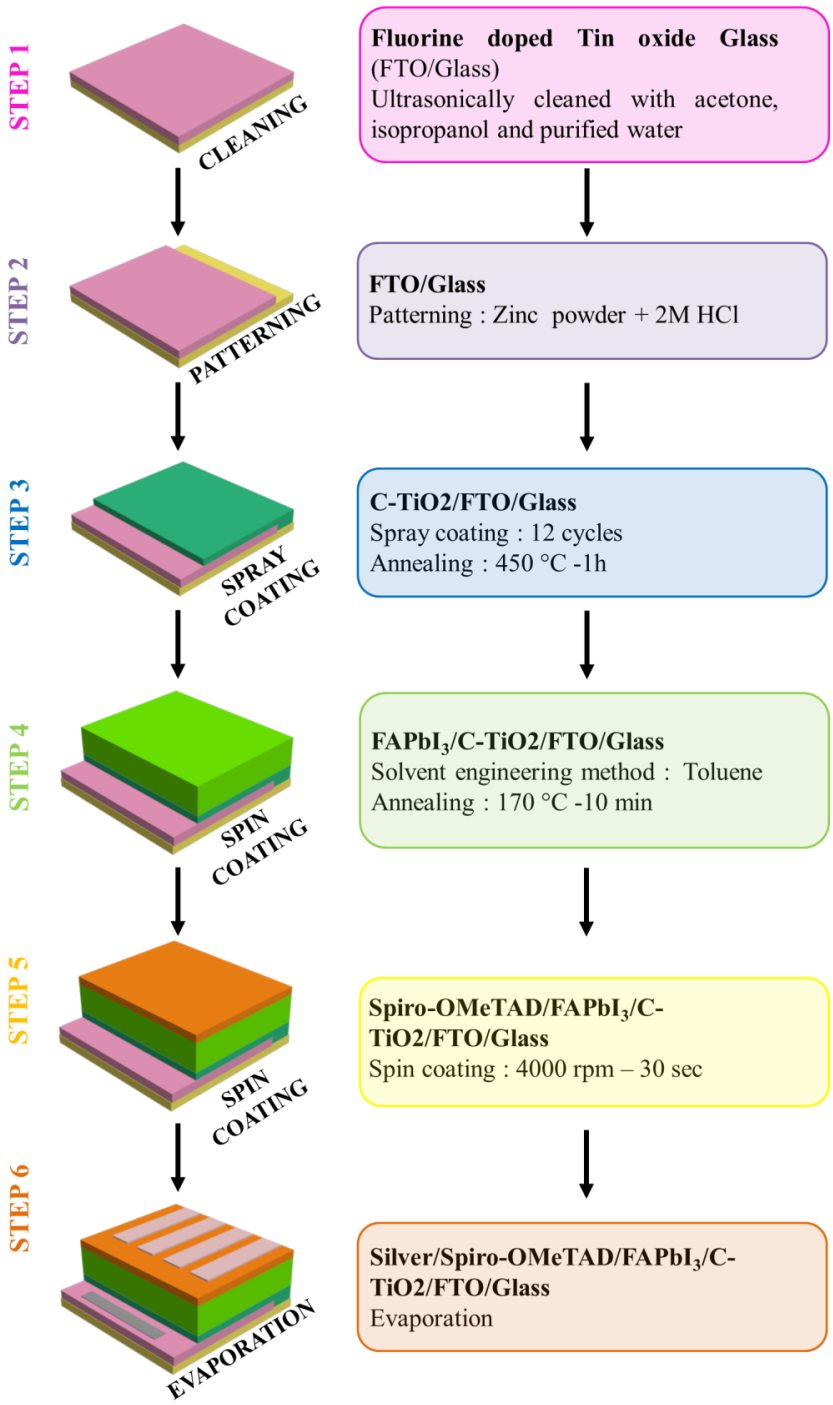

Figure 4. 2. Schematic summarizing the fabrication process of the $FAPbI_3$ perovskite solar cell, where the transparent conductive glass substrate is initially cleaned (step 1), patterned (step 2), and spray coated with a compact layer of titanium dioxide (step 3). The perovskite precursor solution is then spin coated and annealed (step 4), followed by the spin coating of the hole transporting material (step 5). Finally, metal electrodes are thermally evaporated (step 6).

4.3. Results and discussion

4.3.1 Influence of toluene addition on solvent engineering technique

A solvent-engineering technique was used for the fabrication of highly uniform and dense perovskite thin film. This technique has a great potential toward the fabrication of fully solution-processed perovskite solar cells. The planar structure of the device requires having a highly uniform and compact absorber layer to enhance the charge collection in the device and provide good interface with the c-TiO_2 and the hole transporting material, respectively. The method consists of three spin coating stages. First, the precursor solution (FAI and PbI_2) is uniformly deposited on the entire surface of the substrate, and the spin-coater is accelerated to a low rotational speed to remove the excess of solution on the substrate. Second, the rotational speed is increased and maintained at a specific value for several seconds. During this second phase, a drop of solvent is added in order to precipitate the perovskite precursors out of the solvent (DMF). Toluene is a great candidate for the precipitation procedure as it does not dissolve the perovskite precursors and is miscible with DMF. Finally, the rotational speed is increased to a high value in order to evaporate the residual DMF and fully dry the perovskite precursors as a dense and highly uniform layer. By further annealing the thin film, a pure and highly crystalline $FAPbI_3$ phase can be obtained. Figure 4.3 is a picture of $FAPbI_3$ thin films prepared by a solvent engineering technique using toluene. A 3-step spin coating process is used. The substrate is initially spun at 500 rpm for 3 s to remove excess solution. Rotation is then increased to 3500 rpm for 11 s and 1 drop of toluene is added to precipitate the perovskite from the solvent about 1−4 s before the end of the second spin coating step. Finally, the films are dried at 5000 rpm for 30 s. The toluene addition parameters revealed to be critical to obtain a high quality film. In Figure 3 a, b, and c, the toluene is added after 8s, 9s and 10s after the beginning of the second

step, respectively. When the toluene is added too early (8s) or too late (10s), the film is cloudy and seems rough. However, when the toluene is added at 9s, the precursors are frozen on the substrate in a highly uniform and transparent layer.

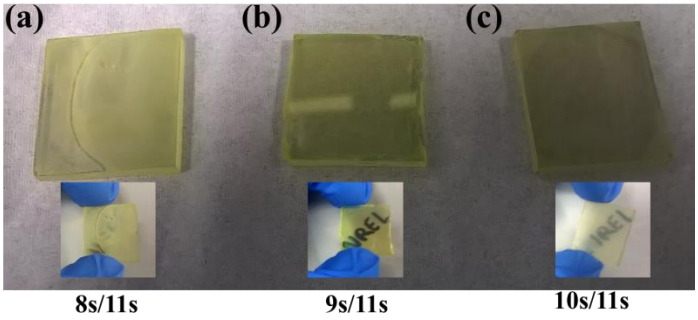

Figure 4. 3. Picture of $FAPbI_3$ thin films prepared by solvent engineering technique. The toluene drop was added at (a) 8 s, (b) 9 s, and (c) 10 s after the beginning of step 2.

Developing a high-quality perovskite thin film with uniform and dense coverage is critical to achieving good performance and reliable studies on charge-carrier dynamics in perovskite solar cells. The properties of the perovskite thin film depend strongly on the processing conditions. To understand the role of toluene on the perovskite film quality, we examined the film morphology, and optical absorbance of the $FAPbI_3$ thin films prepared under different toluene addition time from 8s to 10s during the second spin coating step (total duration : 11s).

4.3.1.1 Morphological characterization

Figure 4.4 shows the field-emission scanning electron microscope (FESEM) images of perovskite films prepared at various addition times, approximately from 8s to 10s. The films prepared at 8s/11s (Figures 4.4a–b) do not indicate the presence of a uniform film on c-TiO_2/FTO/Glass substrate. The grains are arranged in a needle-like structure connected from

several central nucleation point. These structure are growing on the top of the film, and exibit high surface roughness , with broad grain size distibution and micrometer size pinholes. Figures 4.4c–d (9s/11s) show a highly uniform and compact perovskite thin film and do not indicate the presence of any pinholes on c-TiO_2/FTO/Glass substrate.

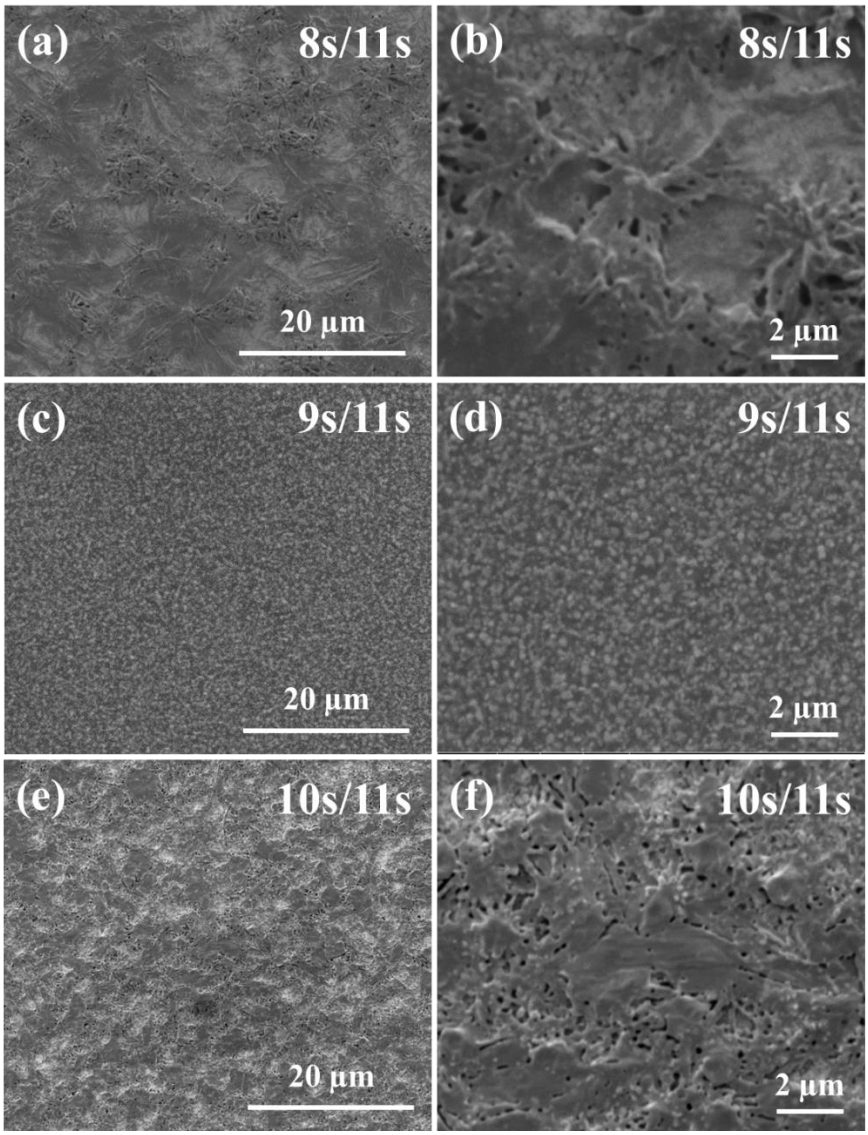

Figure 4. 4. Top-view FESEM images of perovskite thin films prepared at different toluene addition time. (a) and (b), (c) and (d), and (e) and (f) are low and high magnification image of the perovskite film prepared at 8s/11s, 9s/11s and 10s/11s toluene addition time, respectively.

Furthermore, the grain sizes for these films remain similar with a mixture of smaller and larger grains with diameters between 200 and 800 nm. When the addition time is increased to 10s/11s (Figure 4.4e-f), the film loose its uniformity and pinholes with sizes ranging from 50 to 500 nm start to form on the film surface, covering about 17% of the surface area.

4.3.1.2 Optical characterization

Figure 4.5 shows the ultraviolet-visible (UV-Vis) absorption spectra of the $FAPbI_3$ thin films prepared under various toluene deposition time. Films exhibit a broad absorption over the whole visible and near-infrared spectrum with an absorption onset near 840 nm, which is consistent with the reported optical bandgap of about 1.47 eV for the FA-based perovskite.[5,15] In each case, the absorption increases rapidly with decreasing wavelength. However, there are major changes when the toluene is added at 8s and 10s

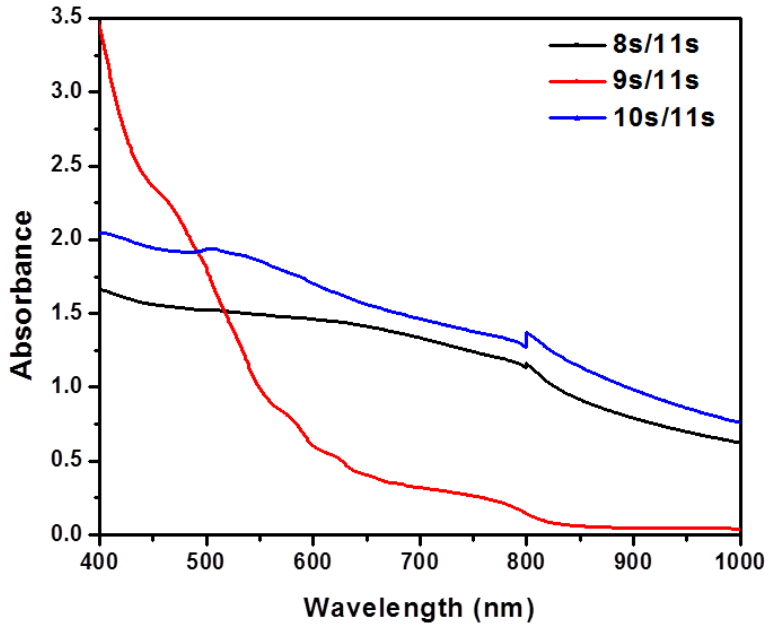

Figure 4. 5. UV−Vis absorption spectra of $FAPbI_3$ films prepared as a function of toluene addition during the solvent engineering process: 8s/11s (black), 9s/11s (red), and 10s/11s (blue).

In contrast to the 9s addition; there is a significant increase in the baseline of the absorption spectrum, indicating enhanced light scattering, which we associate with the formation of pinholes. These results are consistent with the morphological changes observed in FESEM, as shown in Figure 4.4. It is also noteworthy that the features of the absorption spectrum at lower wavelength change significantly compared to films prepared at 9s, showing a degradation of the optical absorbance of the perovskite film.

From the morphological and optical observations, we proposed formation mechanisms for the deposition of the perovskite thin film as a function of addition time of toluene. Upon early addition of the precipitation solvent, some DMF remains trapped with the FAI and PbI_2 precursor materials. When the DMF evaporates during the drying phase, it leaves behind pinholes and a rough surface. At 9s/11s toluene addition, the right amount of DMF is already evaporated, but the film is not yet fully dried, allowing the precursors to be frozen in a dense and uniform film. Upon late addition of the precipitation solvent, the precursor solution already started drying on the patterned substrate and it is too late for freezing the precursor in a compact and uniform film.

4.3.2 Influence of precursor solution concentration on device performance

To fabricate efficient solar cells, the active layer of the light harvester must be thick enough to absorb sufficient incident light and thin enough to avoid recombination of charge carrier at the interfaces. Fortunately, the high absorption coefficient of $FAPbI_3$ allows the use of very thin layers to absorb light over the entire visible and ultraviolet range. To understand the effect of precursor concentration on the perovskite thin film, we performed morphological and optical characterization.

4.3.2.1 Morphological characterization

Figure 4.6 shows the FESEM images of perovskite films prepared at various precursor concentrations, ranging from 0.5M to 0.9M. The films prepared at each concentration (0.5M-0.9M) display uniform and compact perovskite thin film morphology, without the presence of pinholes, on c-TiO_2/FTO/Glass substrate. However, the films show different grain arrangement. For the lowest concentration (Figure 4.6a), the grains show inhomogeneous grain size distribution ranging from 50 to 400 nm. Further, small perovskite particles with a size of about 100 nm are located on the top of the films, providing higher surface roughness. When 0.7M concentration is used (Figure 4.6b), the grain size distribution becomes narrower (ranging from 150 to 400 nm) and the film exhibits a very smooth surface.

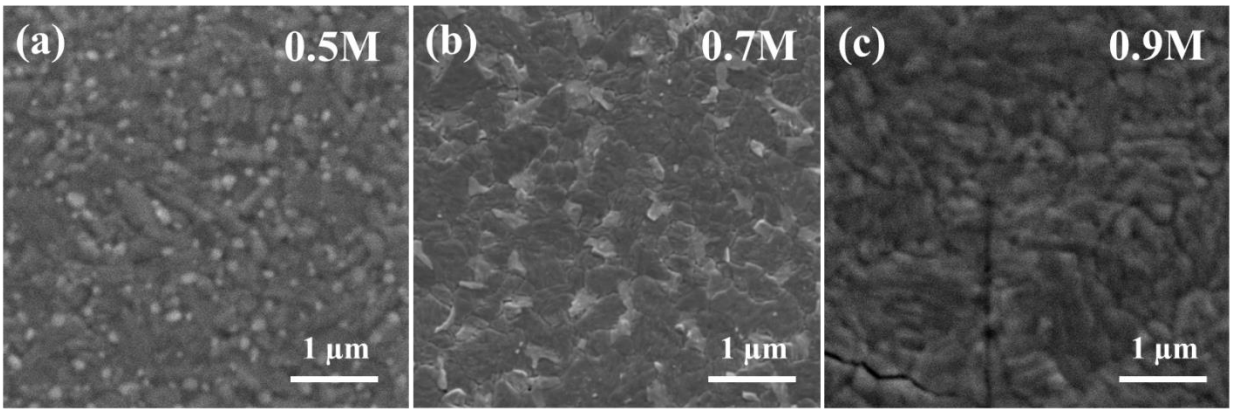

Figure 4. 6. Top-view FESEM images of perovskite thin films prepared at different precursor concentration: (a) 0.5M, (b) 0.7M, and (c) 0.9M.

When the highest concentration is used (Figure 4.6c), the grain size further increase between 200 and 500nm. However, it is important to notice that micrometer size cracks are forming in the film, leading to enhance charge carrier recombination in the final device.

4.3.2.2 Optical characterization

Figure 4.7 shows the UV-Vis absorption spectra of the $FAPbI_3$ thin films prepared under various precursor solution concentrations. Films exhibit a broad absorption over the whole visible and near-infrared spectrum with an absorption onset near 840 nm, which is consistent with the reported optical bandgap of about 1.47 eV for the FA-based perovskite.[5,15]

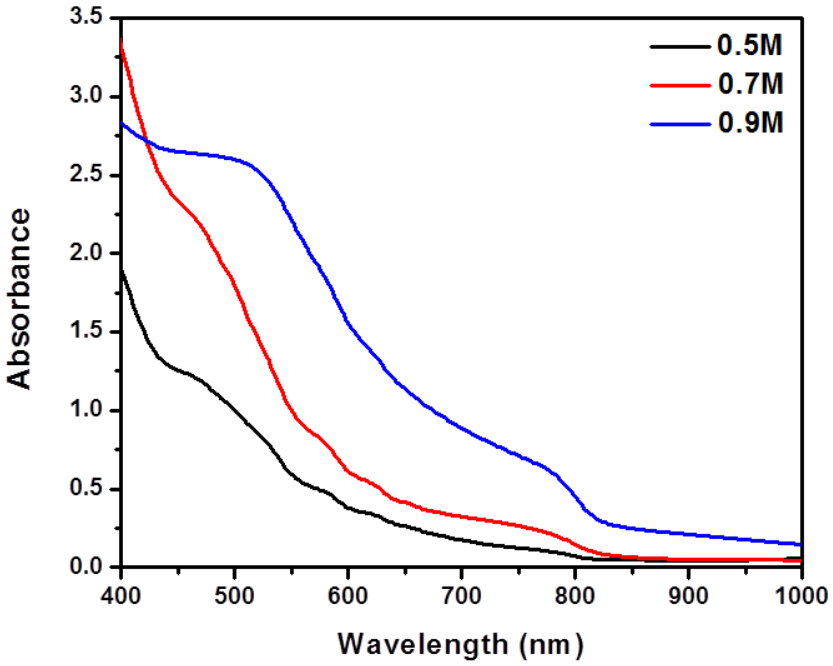

Figure 4. 7. UV−Vis absorption spectra of $FAPbI_3$ films prepared as a function of precursor solution concentration: 0.5M (black), 0.7M (red), and 0.9M (blue).

In each case, the absorption increases rapidly with decreasing wavelength. However, there are major changes when the concentration is increased/decreased from the standard 0.7M value. When 0.5M is used, the absorption is significantly decreased due to a reduced amount of absorber material (thin film thickness below 200 nm) which leads to lower device efficiencies due to lower absorption of incoming light, as discussed later on. When the concentration is raised

to 0.9M, there is a significant increase in the baseline of the absorption spectrum, indicating the presence of a thicker film (about 500 nm) and enhanced light scattering, which we associate with the formation of micrometer-size cracks. These results are consistent with the morphological changes observed in FESEM, as shown in Figure 4.6.

4.3.2.3 Photovoltaic performances

Consistent with the optical and microscopic observation, FA-based PSCs were fabricated to link the observed microstructure differences with device performance. Table 4.1 compares the effect of the precursor solution concentration on the photocurrent density-voltage (*JV*) curves of FA-based devices. Device measurements were conducted under 100 $mW.cm^{-2}$ (AM1.5) simulated solar irradiation. At 0.5M, *JV* curve shows that the device can reach efficiencies up to 9.12%. In correlation with the FESEM and UV-vis observation, it is clear that the devices are workable. Yet, the device performances remain lower due to a smaller film thickness which results in limited light collection in the device. However, when the concentration is increased to 0.7M, an improvement can be seen in the *JV* curves both from the J_{sc}, V_{oc} and Fill Factor (FF), leading to efficiencies of 12.1%.

When the concentration is further increased to 0.9M, the degradation of $FAPbI_3$ photovoltaic performance is observed. This is strongly correlated to higher thickness of the film, as well as the micrometer cracks previously observed in Figure 4.6d in FESEM. These morphological changes lead to higher recombination of charge carriers, which is directly linked to the lower J_{sc}, V_{oc}, and Fill Factor values.

Table 4. 1. Photovoltaic parameters of $FAPbI_3$ perovskite solar cells fabricated as a function of precursor concentration ranging from 0.5M to 0.9M.

Device concentration	J_{sc} ($mA.cm^{-2}$)	V_{oc} (V)	FF (%)	η (%)
0.5M	17.70	0.89	58.12	9.12
0.7M	23.43	0.91	56.83	12.1
0.9M	22.71	0.82	46.19	8.60

4.3.3 General annealing conditions

4.3.3.1 Influence of annealing temperature on device performance

4.3.3.1.1 Morphological characterization

To fabricate efficient solar cells, the active layer of the light harvester must be as crystalline as possible to absorb sufficient incident light. Generally, formamidinium iodide and lead iodide precursors are mixed at equimolar ratio in DMF. When the temperature is raised, the precursors can react to form the formamidinium lead triiodide absorber material. During our experiments, we noticed that $FAPbI_3$ perovskite compound is highly sensitive to the annealing temperature and that a small change can significantly impact the final device's photovoltaic properties. Surprisingly, we did not observe any morphological changes by FESEM for films prepared at temperature ranging from 160 ˚C to 180 ˚C. We further performed optical characterization of thin films by UV-vis spectroscopy.

4.3.3.1.2 Optical characterization

Figure 4.8 shows the absorption spectrums for $FAPbI_3$ thin films annealed at 160˚C (black), 170˚C (red) and 180˚C (blue) for 10 min. It is noteworthy that the films exhibit the same

absorption profile with a broad absorption over the whole visible and near-infrared spectrum and an absorption onset near 840 nm, which is consistent with the morphological observations.

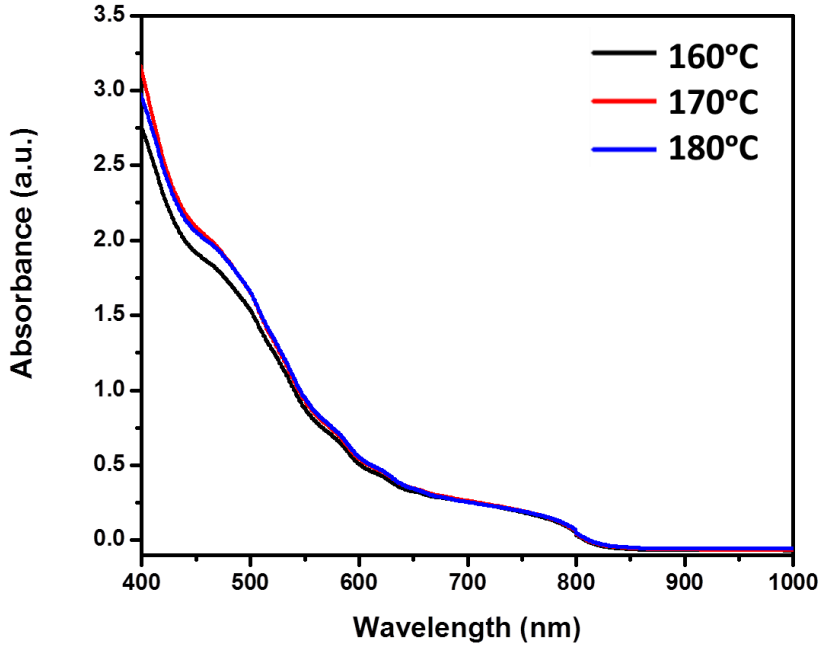

Figure 4. 8. UV−Vis absorption spectra of $FAPbI_3$ films annealed for 10 min as a function of annealing temperature. The data are shown for film annealed at temperature of 160˚C (black), 170˚C (red) and 180˚C (blue).

4.3.3.1.3 Photovoltaic performances

Consistent with the optical and microscopic observation, FA-based PSCs were fabricated to link the observed microstructure differences with device performance. Table 4.2 compares the effect of annealing temperature on the *JV* curves of FA-based devices. Device measurements were conducted under 100 $mW.cm^{-2}$ (AM1.5) simulated solar irradiation. Photovoltaic parameters reveal that the performance of the device is strongly influenced by the annealing temperature; a change of ± 10 ºC will impact the short circuit current and fill factor significantly.

The open circuit voltage will not significantly be dependent on the temperature change. So far, there is no clear explanation for the tremendous effect of annealing temperature on the photovoltaic properties. Morphological and optical analysis did not help to understand the underlying cause of degraded devices performance.

Table 4. 2. Photovoltaic parameters of $FAPbI_3$ perovskite solar cells fabricated as a function of annealing temperature, ranging from 160˚C.

Annealing Temperature (˚C)	**J_{sc} ($mA.cm^{-2}$)**	**V_{oc} (V)**	**FF (%)**	**η (%)**
160˚C	18.87	0.86	36.77	6.00
170˚C	23.43	0.91	56.83	12.1
180˚C	20.94	0.86	45.59	8.21

4.3.3.2 Influence of annealing time on device performance

In addition to its sensitivity to annealing temperatures, formamidinium lead triiodide perovskite material is extremely versatile as a function of annealing time due to its organic-inorganic nature. It is expected that, when the film is deposited on a hot plate calibrated at 170˚C, both precursors will react to form the perovskite material. However, when the material is annealed for an extended period of time, a decomposition mechanism will be initiated due to the dissociation between the organic (FAI) and inorganic (PbI_2) part of the perovskite. To verify this hypothesis, we performed morphological and optical studies of $FAPbI_3$ perovskite thin film annealed at 170˚C as a function of time.

4.3.3.2.1 Morphological characterization

Figure 4.9 shows the FESEM images of perovskite films annealed at 170˚C for various time, ranging from 0 min to 10min. The films prepared at each annealing time exhibit uniform and compact perovskite thin film, without the presence of pinholes, on c-TiO_2/FTO/Glass substrate.

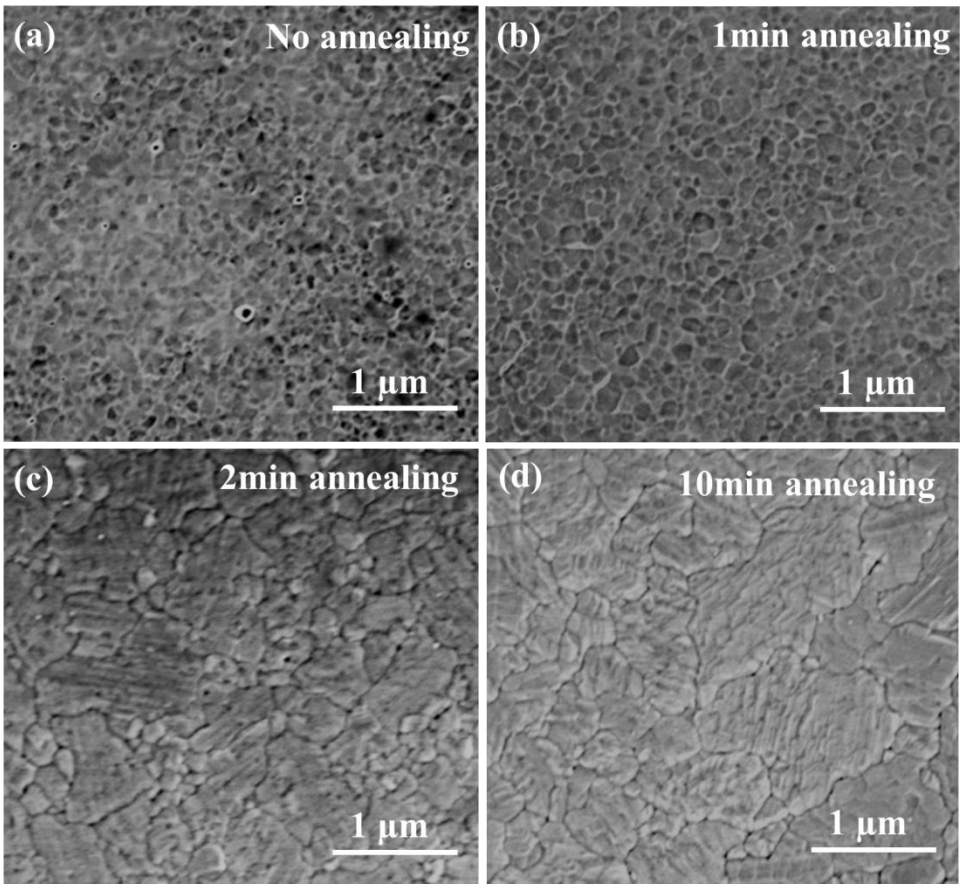

Figure 4. 9. Top-view FESEM images of perovskite thin films annealed at 170˚C for different annealing time: (a) no annealing, (b) 1 min annealing, (c) 2 min annealing and (d) 10 min annealing.

However, the films show different grain size. For the as-prepared film (Figure 4.9a), the crystallization of the precursor materials into perovskite has not been initiated. Small grains with

homogeneous size distribution ranging from 50 to 150 nm are deposited in a dense precursor layer. When the film is annealed for one minute (Figure 4.9b), the film exhibits a similar morphology to the non-annealed one, however the average grain increased, with a broaden grain size distribution ranging from 50 to 250 nm. After 2 min annealing (Figure 4.9c), the $FAPbI_3$ perovskite is fully crystallized and the morphology of the film will not evolve anymore with increased annealing time (Figure 4.9d).

4.3.3.2.2 Optical characterization

These results are further confirmed in Figure 4.10, by UV-Vis absorption spectrum of the $FAPbI_3$ thin films prepared under various annealing time for a constant temperature of 170˚C. For 0 min and 1 min annealing time, a strong PbI_2 absorption peak at 380 nm is observed

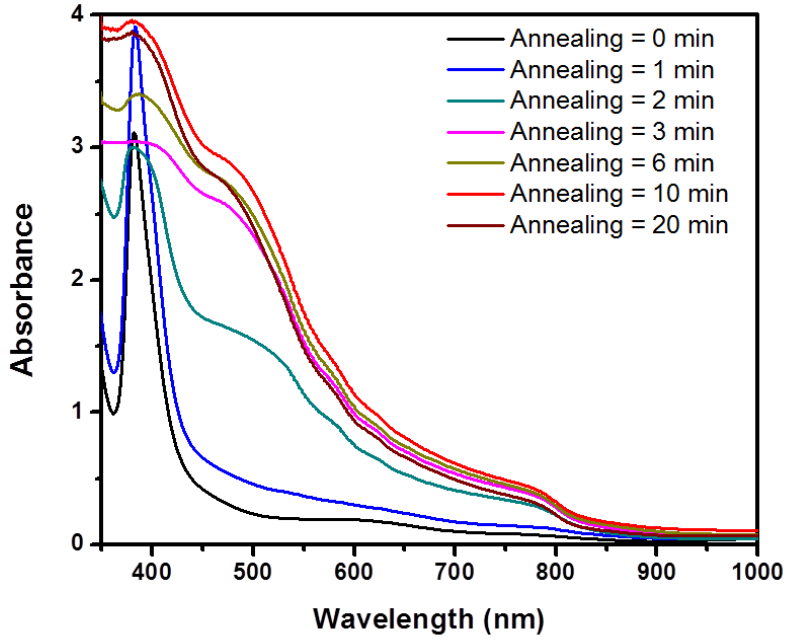

Figure 4. 10. UV−Vis absorption spectra of $FAPbI_3$ films prepared at 170 ºC as a function of annealing time. The spectrums are recorded from no annealing to 20 min annealing time.

In addition, the intensity of the PbI_2 peak decreases with increasing annealing time, leading to the formation of crystalline perovskite after 2 min annealing, confirming the FESEM results shown in Figure 4.9c. After 3 min annealing time, the optical properties of $FAPbI_3$ do not significantly change, as the UV-vis data remain similar. This is further confirming the FESEM results shown in Figure 4.9d, where no morphological change were noted after increased the annealing time to 10 min. After 20 min annealing, there is a slight decrease in the absorption spectrum, showing that the degradation of the perovskite absorber material has been initiated.

4.3.3.2.3 Photovoltaic performances

JV data have been compiled as a function of annealing time for devices prepared at 170 ºC. The results are presented in Table 4.3. For 5 min annealing, *JV* curve shows that the device can reach efficiencies up to 8.05%. However, despite the morphological and optical observation, it is clear that PbI_2 and FAI are not yet fully crystallized into $FAPbI_3$, leading to a reduced efficiency due to an unfinished crystallization process. However, when the time is increased to 10 min, an improvement can be seen in the *JV* curves both from the J_{sc}, V_{oc} and Fill Factor (FF), leading to efficiencies of 12.1%.

When the time is further increased to 15 min and 20 min, the degradation of the $FAPbI_3$ perovskite is initiated. This is probably due to dissociation between PbI_2 and the organic material. This degradation leads to loss in key device parameters: J_{sc}, V_{oc} and Fill Factor which directly impacts the efficiencies of the PSCs. Furthermore, when the time is increased to 25 min, the device is fully degraded and efficiency fall down to 1.5%.

Table 4. 3. Photovoltaic parameters of $FAPbI_3$ perovskite solar cells fabricated as a function of annealing time, ranging from 5 min to 25 min.

Annealing Time (min)	J_{sc} ($mA.cm^{-2}$)	V_{oc} (V)	FF (%)	η (%)
5 min	19.16	0.82	51.25	8.05
10 min	23.43	0.91	56.83	12.1
15 min	18.16	0.91	54.54	8.9
20 min	15.52	0.84	49.01	7.48
25 min	6.99	0.56	38.38	1.5

4.3.4 Refined fabrication parameters for high efficiency $FAPbI_3$ solar cell

From the previous studies, we were able to determine optimum fabrication parameters in order to maximize the photovoltaic parameters and ultimately the efficiency of the final perovskite solar cell. Figure 4.11 is a summary of the optimized parameters for the fabrication process.

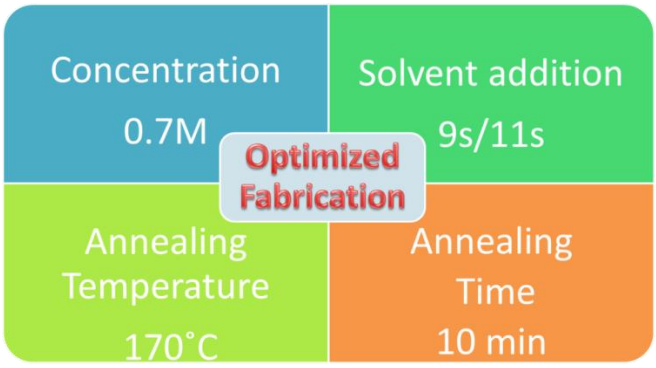

Figure 4. 11. Summary of the optimized fabrication parameters for the processing of highly efficient formamidinium lead triiodide perovskite solar cell.

For the best device, 0.7M precursor solution was used for the solvent engineering method and a drop of toluene was added at exactly 2 s before the end of the second spin coating step in order to obtain a compact and highly uniform perovskite thin film. The annealing of the film was carried out on a hot plate calibrated at 170ºC for 10 min.

4.4 Conclusions

In summary, we have fabricated $FAPbI_3$ planar heterojunction solar cells with a Glass/FTO/c-TiO_2/$FAPbI_3$/Spiro-OMeTAD/Ag construction by a solvent engineering method under controlled fabrication conditions. In this approach, the precursor solution concentration revealed to be critical to obtain the adequate perovskite absorber thin film thickness. The 0.7M concentration was the best, as the film was thick enough to absorb incoming light over the whole solar spectrum and thin enough to limit the recombination mechanisms of the charge carriers due to lateral travel distance. Another step was to study the effect of toluene addition during the solvent engineering process. A timely control of the solvent addition (9s/11s) was necessary to ensure the "freezing" of the precursor materials in a compact and uniform fashion. Finally, the annealing time and temperature were evaluated and revealed to highly impact the solar cells efficiency. For each investigated parameters, we observed that the film morphology, optical, and electrical properties of $FAPbI_3$ differ significantly. Highly uniform and crystalline films were achieved at 170ºC annealing temperature for 10 min. As the annealing process was varied, $FAPbI_3$ films became inhomogeneous with the presence of voids, and the crystalline and optical properties were degraded. This deterioration of the films led to lower device efficiencies, mainly due to a loss in the J_{sc}, $V_{oc,}$ and FF.

4.5 References

(1) Chakhmouradian, A.; Woodward, P. *Phys Chem Minerals* **2014**, *41*, 387.

(2) Wells, H. L. *Zeitschrift für anorganische Chemie* **1893**, *3*, 195.

(3) Mitzi, D. B. In *Progress in Inorganic Chemistry*; John Wiley & Sons, Inc.: 2007, p 1.

(4) Baikie, T.; Fang, Y.; Kadro, J. M.; Schreyer, M.; Wei, F.; Mhaisalkar, S. G.; Graetzel, M.; White, T. J. *Journal of Materials Chemistry A* **2013**, *1*, 5628.

(5) Eperon, G. E.; Stranks, S. D.; Menelaou, C.; Johnston, M. B.; Herz, L. M.; Snaith, H. J. *Energy & Environmental Science* **2014**, *7*, 982.

(6) Koh, T. M.; Fu, K.; Fang, Y.; Chen, S.; Sum, T. C.; Mathews, N.; Mhaisalkar, S. G.; Boix, P. P.; Baikie, T. *The Journal of Physical Chemistry C* **2013**, *118*, 16458.

(7) Gratzel, M. *Nat Mater* **2014**, *13*, 838.

(8) Kim, H.-S.; Lee, C.-R.; Im, J.-H.; Lee, K.-B.; Moehl, T.; Marchioro, A.; Moon, S.-J.; Humphry-Baker, R.; Yum, J.-H.; Moser, J. E.; Gratzel, M.; Park, N.-G. *Sci. Rep.* **2012**, *2*.

(9) Ogomi, Y.; Morita, A.; Tsukamoto, S.; Saitho, T.; Fujikawa, N.; Shen, Q.; Toyoda, T.; Yoshino, K.; Pandey, S. S.; Ma, T.; Hayase, S. *The Journal of Physical Chemistry Letters* **2014**, *5*, 1004.

(10) Boix, P. P.; Nonomura, K.; Mathews, N.; Mhaisalkar, S. G. *Materials Today* **2014**, *17*, 16.

(11) Zhao, Y.; Zhu, K. *Journal of the American Chemical Society* **2014**, *136*, 12241.

(12) Sanchez, R. S.; Gonzalez-Pedro, V.; Lee, J.-W.; Park, N.-G.; Kang, Y. S.; Mora-Sero, I.; Bisquert, J. *The Journal of Physical Chemistry Letters* **2014**, *5*, 2357.

(13) Green, M. A.; Ho-Baillie, A.; Snaith, H. J. *Nat Photon* **2014**, *8*, 506.

(14) Kojima, A.; Teshima, K.; Shirai, Y.; Miyasaka, T. *Journal of the American Chemical Society* **2009**, *131*, 6050.

(15) Lee, J.-W.; Seol, D.-J.; Cho, A.-N.; Park, N.-G. *Advanced Materials* **2014**, *26*, 4991.

(16) Chen, Q.; Zhou, H.; Hong, Z.; Luo, S.; Duan, H.-S.; Wang, H.-H.; Liu, Y.; Li, G.; Yang, Y. *Journal of the American Chemical Society* **2013**, *136*, 622.

(17) Im, J.-H.; Jang, I.-H.; Pellet, N.; Grätzel, M.; Park, N.-G. *Nat Nano* **2014**, *advance online publication*.

(18) Green, M. A.; Emery, K.; Hishikawa, Y.; Warta, W.; Dunlop, E. D. *Progress in Photovoltaics: Research and Applications* **2015**, *23*, 1.

(19) Hanusch, F. C.; Wiesenmayer, E.; Mankel, E.; Binek, A.; Angloher, P.; Fraunhofer, C.; Giesbrecht, N.; Feckl, J. M.; Jaegermann, W.; Johrendt, D.; Bein, T.; Docampo, P. *The Journal of Physical Chemistry Letters* **2014**, *5*, 2791.

(20) Lv, S.; Pang, S.; Zhou, Y.; Padture, N. P.; Hu, H.; Wang, L.; Zhou, X.; Zhu, H.; Zhang, L.; Huang, C.; Cui, G. *Physical Chemistry Chemical Physics* **2014**, *16*, 19206.

(21) Pang, S.; Hu, H.; Zhang, J.; Lv, S.; Yu, Y.; Wei, F.; Qin, T.; Xu, H.; Liu, Z.; Cui, G. *Chemistry of Materials* **2014**, *26*, 1485.

(22) Jeon, N. J.; Noh, J. H.; Yang, W. S.; Kim, Y. C.; Ryu, S.; Seo, J.; Seok, S. I. *Nature* **2015**, *517*, 476.

(23) Lee, J.-W.; Lee, S. H.; Ko, H.-S.; Kwon, J.; Park, J. H.; Kang, S. M.; Ahn, N.; Choi, M.; Kim, J. K.; Park, N.-G. *Journal of Materials Chemistry A* **2015**.

(24) Wang, F.; Yu, H.; Xu, H.; Zhao, N. *Advanced Functional Materials* **2015**, *25*, 1120.

(25) Wozny, S.; Yang, M.; Nardes, A. M.; Mercado, C. C.; Ferrere, S.; Reese, M. O.; Zhou, W.; Zhu, K. *Chemistry of Materials* **2015**.

(26) Burschka, J.; Pellet, N.; Moon, S.-J.; Humphry-Baker, R.; Gao, P.; Nazeeruddin, M. K.; Gratzel, M. *Nature* **2013**, *499*, 316.

(27) Mei, A.; Li, X.; Liu, L.; Ku, Z.; Liu, T.; Rong, Y.; Xu, M.; Hu, M.; Chen, J.; Yang, Y.; Grätzel, M.; Han, H. *Science* **2014**, *345*, 295.

(28) Niu, G.; Li, W.; Meng, F.; Wang, L.; Dong, H.; Qiu, Y. *Journal of Materials Chemistry A* **2014**, *2*, 705.

(29) Zhao, Y.; Nardes, A. M.; Zhu, K. *The Journal of Physical Chemistry Letters* **2014**, *5*, 490.

(30) Jeon, N. J.; Noh, J. H.; Kim, Y. C.; Yang, W. S.; Ryu, S.; Seok, S. I. *Nat Mater* **2014**, *13*, 897.

Chapter 5 Effect of controlled humidity on high-performance formamidinium lead triiodide planar heterojunction solar cells*

5.1 Introduction

Over the last several years, hybrid organic–inorganic perovskite solar cells have become one of the most attractive photovoltaic technologies, with easy solution fabrication and high conversion efficiencies.[1-4] Perovskite has an ABX_3 structure where "A" and "B" are cations of various size and X is the anion.[1,2,5,6] Adjusting A, B, and/or X with different elements can significantly change the material and optoelectronic properties of perovskites.[6-10] Methyl ammonium (MA) cation in the A site is so far the most explored perovskite composition in the past few years.[1,2,10-13] Despite the rapid progress for MA-based perovskite absorbers (e.g., $MAPbI_3$), their optical bandgaps are generally larger than 1.55 eV. Replacing MA with formamidinium (FA or $CH(NH_2)_2^+$) represents one direction to reduce the bandgap toward a more ideal range.[4,7,14-18] For example, $FAPbI_3$ is reported to have a bandgap of about 1.47 eV.[7,15,19] Thus, replacing $MAPbI_3$ with $FAPbI_3$ should, in theory, lead to >10% gain in the photocurrent density. However, to date, experimental work based on FA-perovskite solar cells had been limited to only a few publications, including pure $FAPbI_3$[16,18,20,21], and perovskites with either mixed halides[7,13,17,22] or mixed organic cations.[23,24] It is noteworthy that a recent study shows that a bilayer structure of $FAPbI_3$ followed by a thin layer of $MAPbI_3$ enhances light absorption of pure $FAPbI_3$,[15] whereas another study illustrates that compositional engineering

*This chapter was adapted from: Wozny, S.; M.; Nardes, A.; Mercado, C.; Ferrere, S,; O Reese, M.; Zhou, W., Zhu, K.; A Controlled Humidity Study on the Formation of Higher Efficiency Formamidinium Lead Triiodide-Based Solar Cells *Chem. Mater*., DOI: 10.1021/acs.chemmater.5b016912015

by mixing 85% of $FAPbI_3$ with 15% of $MAPbBr_3$ can lead to >18% devices.[4] In addition, FA-based devices could have higher stability than MA-based cells.[23] These reports illustrate the potential and importance of studying FA-based solar cells for future perovskite solar cell applications.

Among various environmental factors, moisture has received increasing attention due to its reported impact on perovskites, including material properties and device characteristics (e.g., efficiency and stability). Most of such studies were conducted with MA-based perovskites. It has been reported previously for MA-based perovskite that the relative humidity is detrimental to the device performance.[8,25] Kamat et al.[25] reported that pure $MAPbI_3$ perovskite gets hydrated $[(CH_3NH_3)_4PbI_6.2H_2O]$ under a humid environment in the dark and it forms PbI_2 under a humid environment in light.[25,26] The crystallographic deterioration is mainly responsible for the degraded device performance. However, another study showed that a moderate moisture level (~35% relative humidity) can enhance the recrystallization of perovskites during the normal film formation process and thus result in a high-quality perovskite film and solar cell performance using MA-based perovskites.[27] Despite various effects reported for MA-based perovskite, the roles of moisture/humidity on FA-based perovskites has not been fully studied.

In this chapter, we examine the effect of relative humidity during film preparation on the structural, optical, and electrical properties of $FAPbI_3$ thin films. Moisture strongly impacts the morphological, crystalline, and optical properties of $FAPbI_3$, and the performances of final devices. Using the low-humidity environment, the best efficiency obtained for a planar $FAPbI_3$ perovskite solar cell is 16.6% (under one-sun illumination) with stabilized maximum power output corresponding to an efficiency of 16.4%. The device performance decreases with increasing environmental humidity level. This loss in efficiency is mainly attributed to the

deterioration of the films upon humidity exposure, leading to a lower fill factor, lower recombination resistance, and shorter carrier lifetime.

5.2 Experimental

5.2.1 Synthesis of precursors solution for device fabrication

5.2.1.1 Formamidinium lead triiodide

All solvents and reagents were of analytical grade and used as received. Lead Iodide (PbI_2, 99.999%) was purchased from Alfa Aesar. Formamidinium iodide (FAI) was purchased from Lumtec. Anhydrous N,N'-dimethylformamide (DMF) and toluene were purchased from Sigma Aldrich. A 0.7M perovskite solution was prepared from stoichiometric amount of lead iodide (PbI_2) and FAI in DMF. The solution was vortexed for 30 min to dissolve PbI_2 and FAI powders in DMF, leading to a clear bright yellow solution. Finally the solution was filtered twice to remove any undissolved starting materials.

5.2.1.2 2',7,7'-tetrakis(N,N-dip-methoxyphenylamine)-9,9'-spirobifluorene solution

2',7,7'-tetrakis(N,N-dip-methoxyphenylamine)-9,9'-spirobifluorene solution abbreviated as Spiro-OMeTAD was prepared by adding 80 mg of spiro-OMeTAD, 30µl of bis(trifluoromethane)sulfonimide lithium salt stocking solution (500 mg Li-TFSI in 1 ml acetonitrile), and , 30µl of 4-tert-butylpyridine (TBP) in 1 ml chlorobenzene. The solution was vortexed for 30 min and used immediately.

5.2.2 Substrate preparation

A 1x1 inch Fluorine-doped SnO_2-coated transparent conducting glass (FTO/Glass) substrate was patterned using a 2M HCl solution and Zinc powder.[9] A c-TiO_2 compact blocking

layer was spray coated on the hot FTO glass (450°C) using 0.2 M solution of Ti(IV) bis(ethyl acetoacetate)-diisopropoxide in 1-butanol. The spraying process was repeated for 12 cycles and the substrate was subsequently annealed at 450 °C for 1 hour.[10]

5.2.3 Device fabrication

The devices were fabricated in a dry box where the humid environment was regulated by adjusting air and vapor water flows simultaneously. The humidity was measured by a digital hygrometer (±4% R.H.). The substrates and precursor solutions were exposed to control humid environment (inside the dry box) until the RH% stabilized to a certain value, typically 20 min prior to any deposition. Figure 5.1 summarizes the fabrication process of perovskite solar cell.

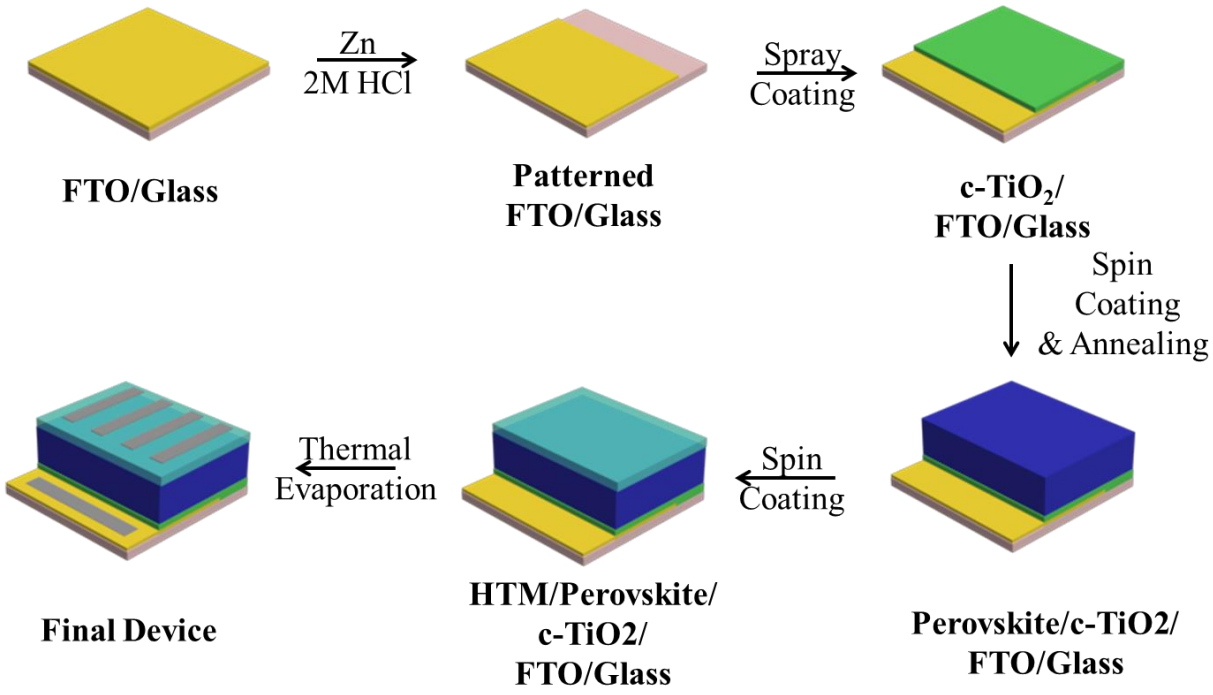

Figure 5. 1. Schematic summarizing the fabrication process of the $FAPbI_3$ perovskite solar cell.

Briefly, 100µl of perovskite solution was deposited onto the c-TiO_2/FTO by spin coating.[3] The substrate was spun at 500 rpm for 3 sec to remove excess solution. Rotation was then increased to 3500 rpm and 1 drop of toluene was added to precipitate the perovskite from the solvent exactly 2 seconds before the end of the second spin coating step. The films were dried at 5000 rpm for 30 sec.

5.3 Results and discussion

5.3.1 $FAPbI_3$ solar cell design and working process

Figure 5.2a shows a schematic of a typical FAPbI3 planar heterojunction solar cell. The substrate was subsequently annealed at 170°C for 10 min on a hot plate. The film was cooled for 1 min, before spin coating the spiro-OMeTAD solution on the warm substrate for 30 seconds at 4000 rpm. Finally, silver electrodes were thermally evaporated to evaluate the performance of the device. A diagram of the band alignment is represented in Figure 5.1b. Upon illumination, FAPbI3 absorbs the light, and electron-hole pairs are generated: electrons are injected into the conduction band of the TiO2 blocking layer and FTO/glass, whereas holes are transferred to the highest occupied molecular orbital (HOMO) of the Spiro-OMeTAD and collected by the Ag metal electrodes.[28]

5.3.2 $FAPbI_3$ thin film

Developing a high-quality perovskite thin film with uniform and dense coverage is critical to achieving good performance and reliable studies on charge-carrier dynamics in perovskite solar cells. The properties of the perovskite thin film depend strongly on the

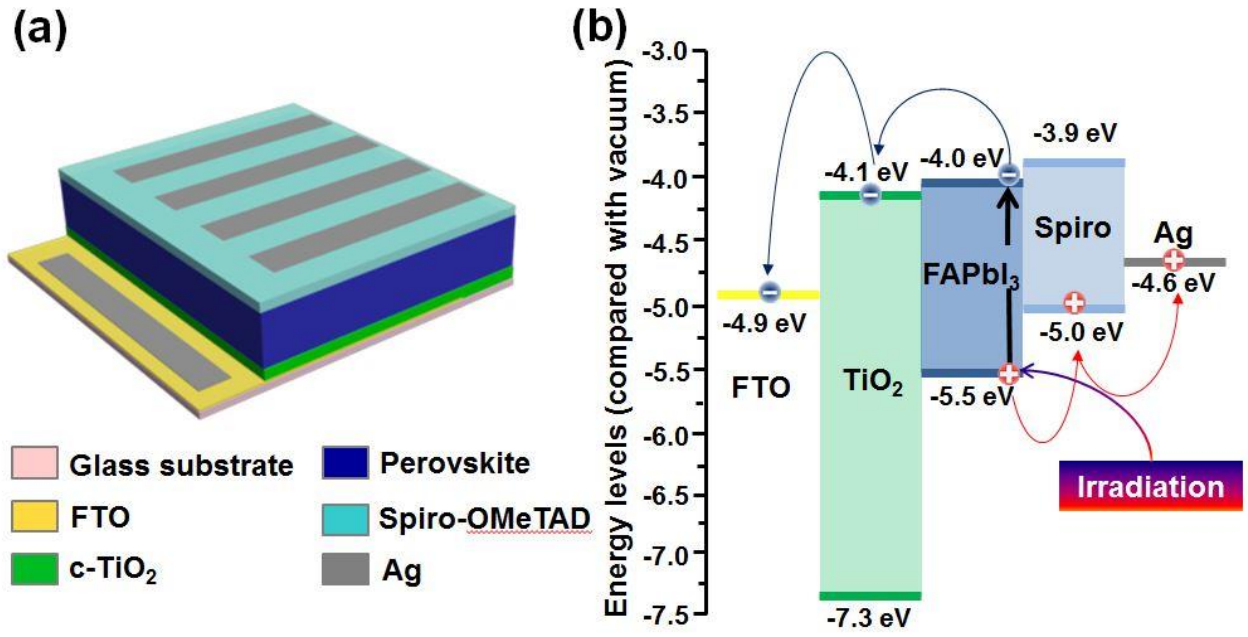

Figure 5. 2. (a) Schematic illustration of a planar heterojunction perovskite solar cell. The device has a Glass/FTO/c-TiO_2/Perovskite/Spiro-OMeTAD/Ag structure. (b) Energy-level diagram and charge transfer in TiO_2-based perovskite solar cell.

processing conditions (e.g., precursor composition, spin-coating speed, and processing environment).To understand the role of humidity on the perovskite film quality, we examined the film morphology, optical absorbance, and phase purity of the $FAPbI_3$ thin films prepared under different relative humidity (R.H.) ranging from 2% to 40% R.H. at room temperature.

5.3.2.1 Morphological characterization

Figure 5.3 shows the field-emission scanning electron microscope (FESEM) images of perovskite films prepared at various relative humidities, approximately from 2% to 40% R.H. The films prepared from 2% to 20% R.H. (Figures 5.2a–c) do not indicate the presence of any pinholes on c-TiO_2/FTO/Glass substrate. Furthermore, the grain sizes for these films remain

similar with a mixture of smaller and larger grains with diameters between 200 and 800 nm. When the relative humidity is increased to 30% (Figure 5.2d), pinholes with sizes ranging from 50 to 500 nm start to form on the film surface, covering about 13% of the surface area. When the humidity is further increased to 40% (Figure 5.2e), the coverage of the absorber material decreases to about 75% with the size of pinholes ranging between 200 nm and 1 μm. However, it is interesting to note that grain size at high humidity level increases substantially to a range of about 0.5 to 1.8 μm.

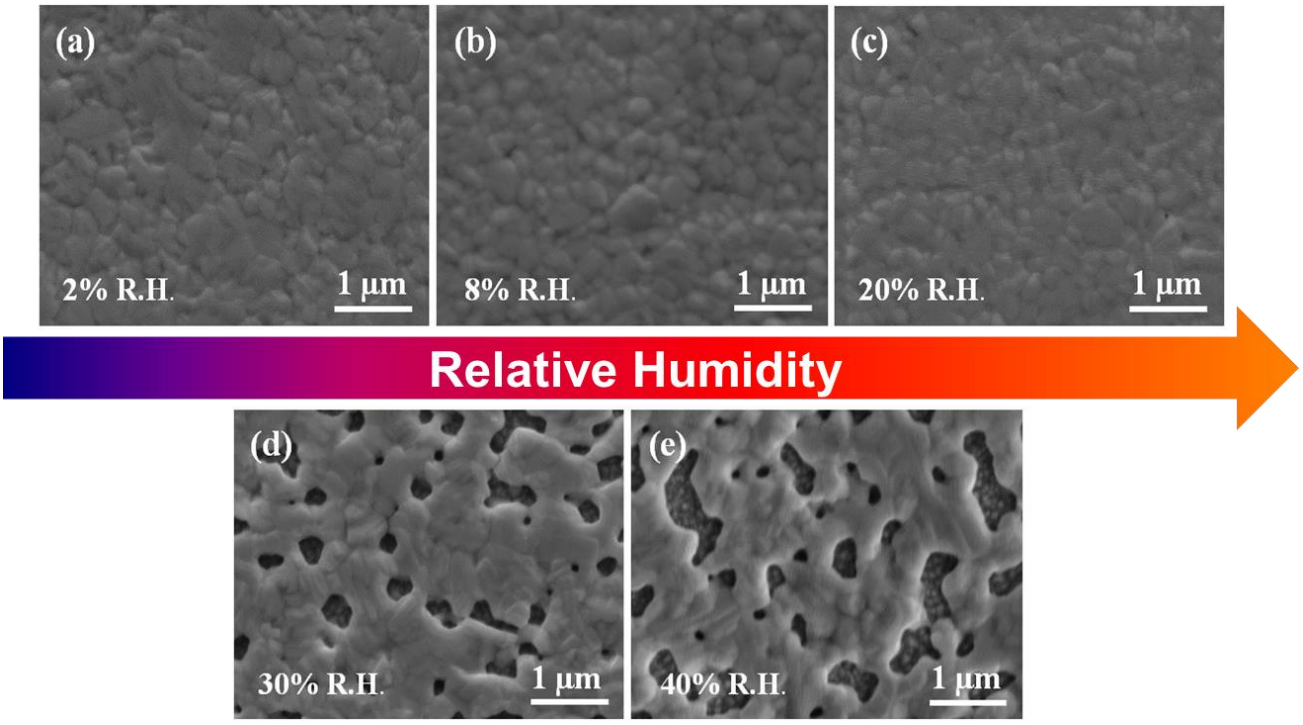

Figure 5. 3. Top-view FESEM images of perovskite thin films prepared at various relative humidities: (a) 2% R.H., (b) 8% R.H., (c) 20% R.H., (d) 30% R.H., and (e) 40% R.H.

Figure 5.4 shows the field-emission scanning electron microscope (FESEM) images of perovskite films prepared at 170 ˚C with various annealing time, from 0 min (no annealing) to 10

min. Figure 5.4a shows the presence of pinholes without annealing. The humidity, in conjunction with spin coating results in partially covered films. The annealing process slightly reduces the pinhole size since while the grains become larger with increasing time.

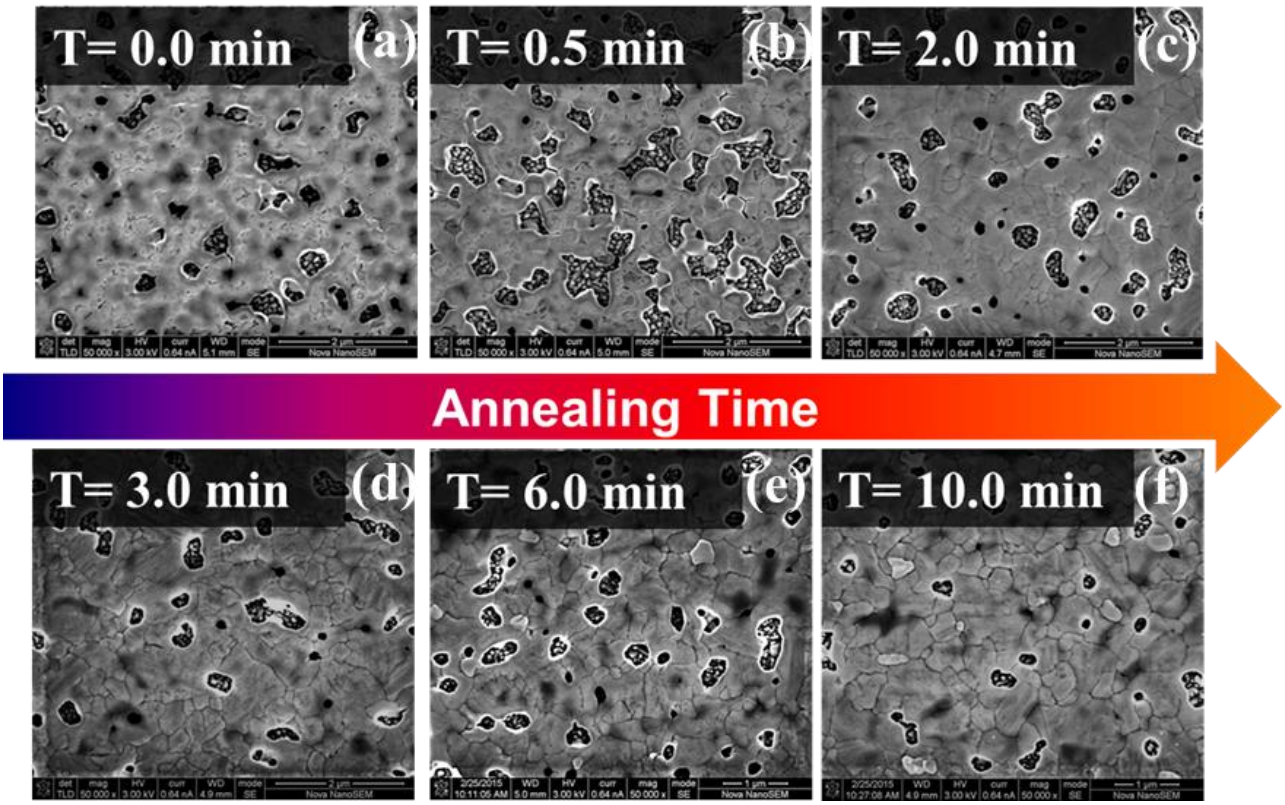

Figure 5. 4. Top-view FESEM images of perovskite thin films prepared at various annealing time: (a) 0min, (b) 0.5min, (c) 2min, (d) 3min, and (e) 6min and (f) 10min.

5.3.2.2 Crystallographic characterization

Figure 5.5 compares the X-ray diffraction (XRD) patterns of $FAPbI_3$ thin films spin-coated on the FTO/Glass substrate covered with a compact layer of TiO_2, which has the same architecture as the one used for the device fabrication. These films were prepared under relative humidities as indicated. At each humidity level, a pure $FAPbI_3$ trigonal phase (P3*m*1) is observed, which is confirmed by the presence of the main diffraction peaks (111), (120), (021),

(222), (231), (030), (240), and (333) at 13.9°, 19.7°, 24.2°, 28.1°, 31.4°, 33.7°, 40.2°, and 42.7°, respectively, which is in good agreement with literature.[18] It is interesting to note that (111) peaks near 14° show the strongest intensity at 2% R.H. With increasing humidity, the (111) peaks decreases in intensity. This observation may suggest a loss of the crystallinity of perovskites with higher humidity content, and larger disordered regions between grains. However, it is important to note that despite the high relative humidity used to fabricate the films and the morphological changes observed (Figure 5.3), there is no recrystallization of the $FAPbI_3$ films into PbI_2 or $(CH_3NH_3)_4PbI_6.2H_2O$ as mentioned in a previous $MAPbI_3$ report.[25]

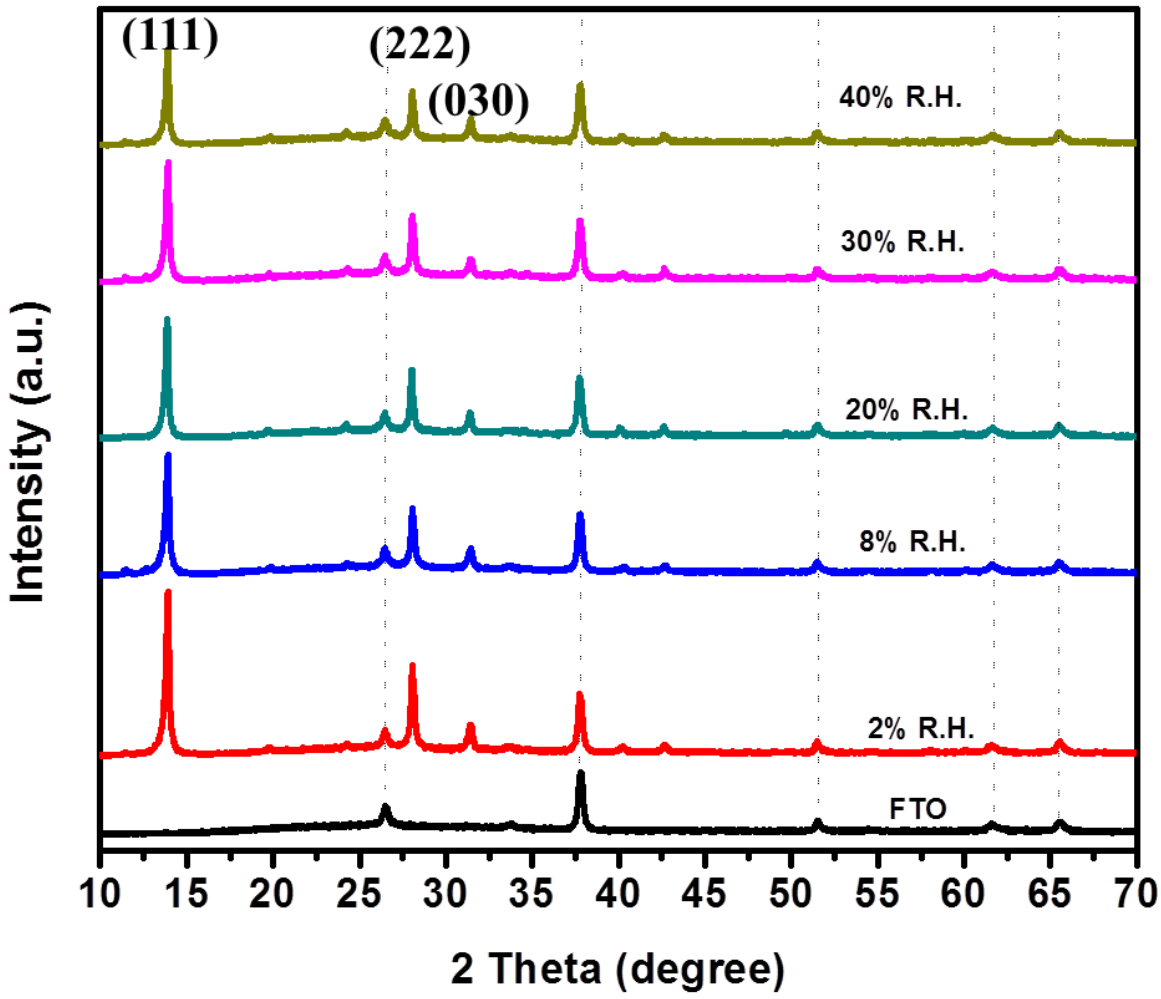

Figure 5. 5. XRD patterns of FTO/Glass (black), FAPbI3 films prepared at various relative humidities: 2% (red), 8% (blue), 20% (turquoise), 30% (pink), and 40% R.H. (gold).

5.3.2.3 Optical properties

Figure 5.6a shows the ultraviolet-visible (UV-Vis) absorption spectra of the $FAPbI_3$ thin films prepared under various humidity levels as indicated. Films exhibit a broad absorption over the whole visible and near-infrared spectrum with an absorption onset near 840 nm, which is consistent with the reported optical bandgap of about 1.47 eV for the FA-based perovskite.[7,15] The absorption increases rapidly with decreasing wavelength. There is essentially no change when the relative humidity level increases from 2% to 8%. Further increasing R.H. to 20% slightly lowers the absorption at wavelength below 700 nm, which agrees with the decrease in the XRD peak intensity, as shown in Figure 5.6. But it is noteworthy that the differences in the absorption spectra of films prepared under 2%–20% R.H. are relatively small, which is consistent with their similar film morphologies (Figure 5.3). In contrast, when the humidity level is further increased to 30%, there is a significant increase in the baseline of the absorption spectrum, indicating enhanced light scattering, which we associate with the formation of pinholes. When the film is prepared under 40% R.H., the baseline absorption increases, but also, the features of the absorption spectrum at lower wavelength change significantly compared to films prepared under lower humidity level, showing a degradation of the optical absorbance of the perovskite film. Figure 5.6b shows the direct band gap extrapolation using Tauc plots for $FAPbI_3$ films fabricated and annealed at different humidities ranging from 2% to 40%. The band gap value slightly decreases from 1.51 eV at 2% R.H. to 1.47 eV at 40% R.H.

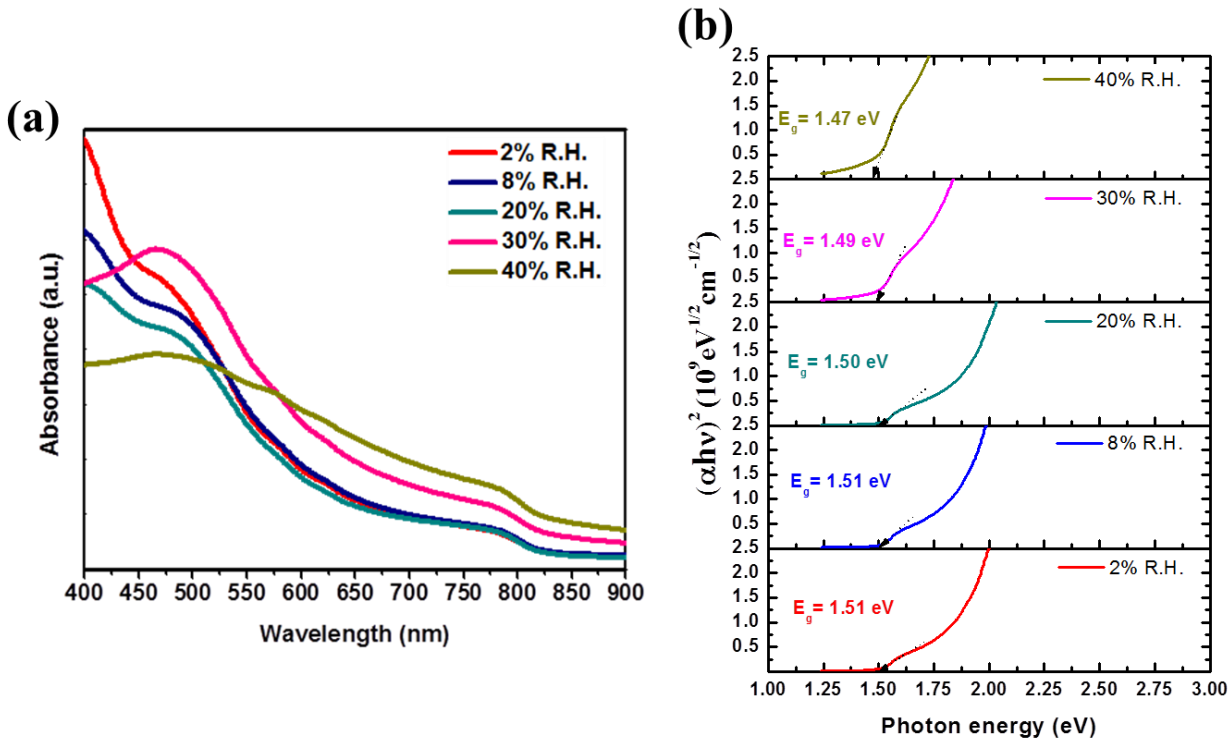

Figure 5. 6. (a) UV−Vis absorption spectra of FAPbI3 films prepared at various relative humidities: 2% (red), 8% (blue), 20% (turquoise), 30% (pink), and 40% R.H. (gold), and (b) Direct band gap extrapolation using Tauc plots for FAPbI3 films fabricated and annealed at different humidities ranging from 2% to 40%. The band gap value slightly decreases from 1.51 eV at 2% R.H. to 1.47 eV at 40% R.H.

5.3.3 $FAPbI_3$ device characterization

5.3.3.1 Photocurrent density-voltage

Figure 5.7 compares the effect of relative humidity on the photocurrent density-voltage (*JV*) curves of devices based on $FAPbI_3$ films prepared under various R.H. ranging from 2% to 40%. The measurements were conducted under 100 $mW.cm^{-2}$ (AM1.5) simulated solar irradiation. The power conversion efficiency of a typical FA-based solar cell (Figure 5.7a) can reach up to 15.2%, with standard deviation of 1.2% under 2% R.H with a short-circuit current of

22.18 mA.cm^{-2}, an open-circuit voltage of 1.04 V, and a fill factor of 0.69. These good photovoltaic parameters are attributed to the high crystallinity of the pure $FAPbI_3$ phase, as well as the smooth film surface without the presence of pinholes, due to our improved solvent engineering technique, high temperature, and short annealing time. However, the device efficiencies gradually decrease from 15.5% (2% R.H.) to 9.0% (40% R.H.). The differences in efficiency are attributed to decreasing V_{oc}, as well as fill factor, as the R.H. increases. The drop in V_{oc} is attributed to increased recombination of the charge carriers in $FAPbI_3$ due to a loss in the crystallinity of the compound, as previously observed in the XRD data (Figure 5.4).

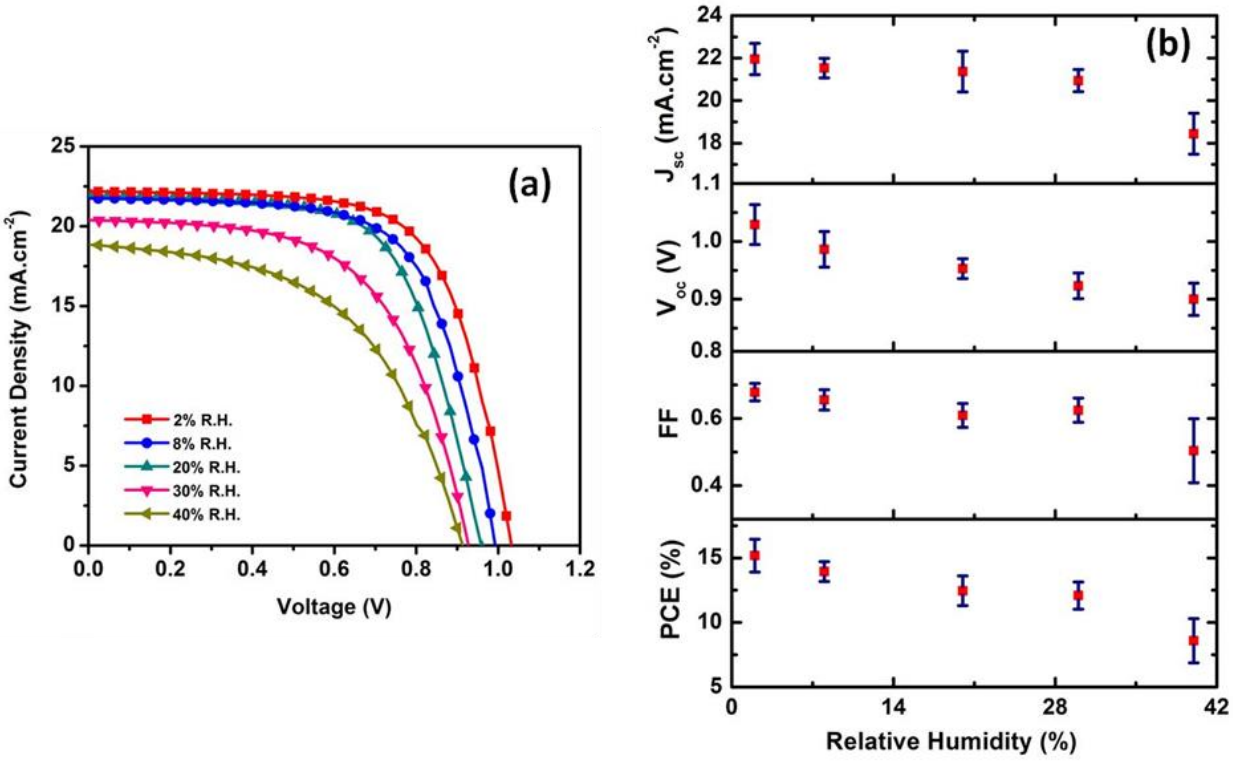

Figure 5. 7. (a) Photocurrent density−voltage (*J*–*V*) characteristics of planar perovskite solar cells based on $FAPbI_3$ films prepared under various relative humidity levels as indicated. Measurements were done under 100 mW/cm^2 AM 1.5 irradiation. (b) Statistical data for the photovoltaic parameters (i.e., short-circuit photocurrent density J_{sc}, open-circuit voltage V_{oc}, fill factor FF, and power conversion efficiency PCE) for planar perovskite solar cells based on $FAPbI_3$ prepared under various relative humidity levels.

In addition, the partial coverage (pinholes) of the perovskite thin film fabricated at higher humidity may lead to direct contact between hole transporting material (HTM) HTM and TiO_2 contact layers, forming internal shunts that lead to lower V_{oc} value. The details of the photovoltaic parameters are listed in Table 5.1. In-depth characterization of several devices was performed to test the reproducibility and accuracy of the devices. At each relative humidity, 16 devices were examined and the statistical data for the photovoltaic parameters (J_{sc}, V_{oc}, FF, and PCE) are compared in Figure 5.7b. The data showed reproducible results with relatively low standard deviations, confirming that our modified solvent engineering technique is reliable for production of standard devices.

Table 5. 1. Photovoltaic parameters of $FAPbI_3$ perovskite solar cells fabricated at various relative humidities from 2% to 40%.

Relative Humidity (%)	**J_{sc} ($mA.cm^{-2}$)**	**V_{oc} (V)**	**Fill Factor**	**Efficiency (%)**
2%	22.18	1.04	0.69	15.5
8%	21.89	0.99	0.67	14.4
20%	21.76	0.97	0.65	13.6
30%	20.39	0.93	0.59	11.1
40%	18.88	0.92	0.52	9.0

5.3.3.2 External quantum efficiency

Figure 5.8 shows the external quantum efficiency (EQE) spectrum of a typical device prepared under 8% R.H. The EQE spectrum shows the average external quantum efficiency of

about 85% between 400 and 600 nm. EQE starts decreasing to 75% until 700 nm and exhibits a characteristic $FAPbI_3$ absorption edge at about 840 nm. The integrated photocurrent density from EQE spectra (~21 $mA.cm^{-2}$) matches well with the J_{sc} value obtained from the *JV* measurements.

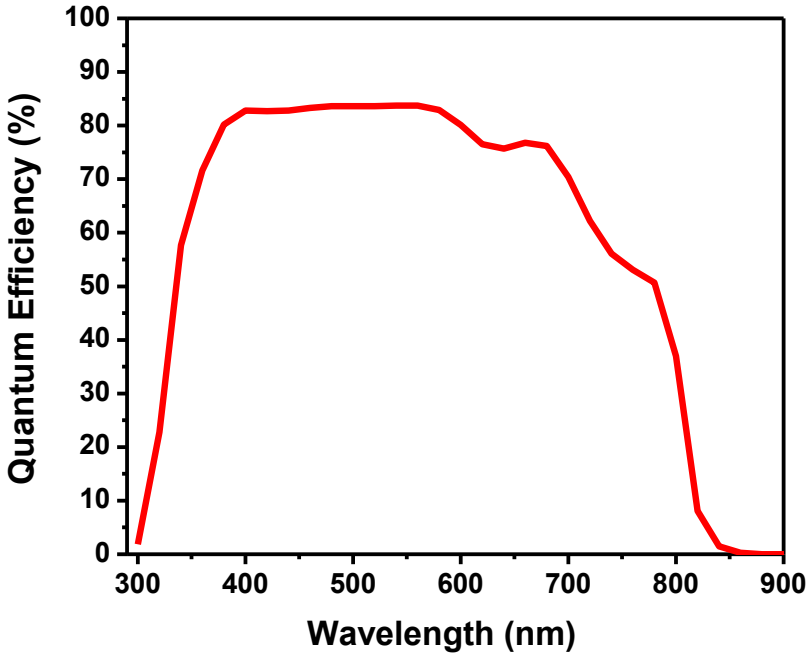

Figure 5. 8. Integrated incident photon to current efficiency (IPCE) data for a standard $FAPbI_3$ planar heterojunction device.

5.3.3.3 Champion device

Figure 5.9a shows forward and reverse *JV* curves of the best device based on $FAPbI_3$ films prepared under 2% R.H. Scan direction tests were performed to evaluate the *JV* hysteresis. Under the reverse scan (from open circuit to short circuit), the device delivers a power conversion efficiency of 16.6% with a J_{sc} of 21.43 $mA.cm^{-2}$, V_{oc} of 1.11 V, and FF of 0.70. The values for the J_{sc} and V_{oc} were almost identical between the reverse and forward (from short circuit to open circuit) scans with some hysteresis mainly in the fill factor, leading to a PCE of

14.3% under the forward scan. To verify the efficiency, Figure 5.9b shows the time-dependent photocurrent density (*J*) and PCE output measure for >300 s at the maximum power point. The *J* and PCE reach a steady state of 20 $mA.cm^{-2}$ and 16.4 %, respectively, and agree well with the *JV* curve obtained from the reverse scan.

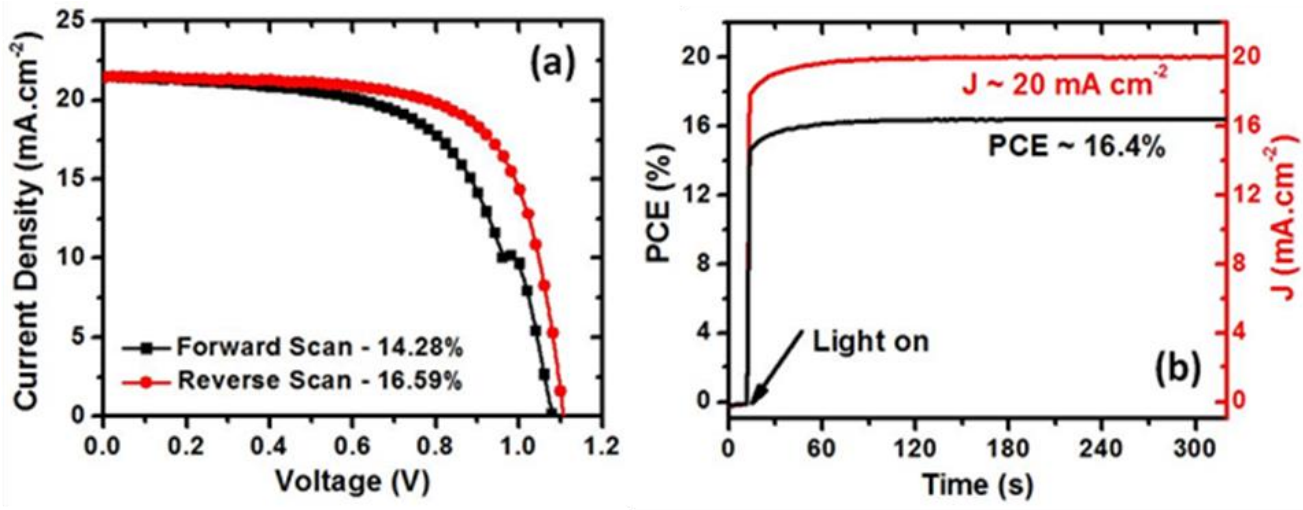

Figure 5. 9. (a) Forward and reverse J–V curves (one-sun illumination) of the best planar perovskite solar cells based on FAPbI3 films prepared under 2% R.H. (b) Steady-state PCE and photocurrent density at maximum power point as a function of time.

5.3.3.4 Impedance spectroscopy

Impedance spectroscopy is used to study the effect of R.H. on the charge-carrier recombination resistance (R_{rec}) as a function of the applied bias in the relevant voltage range (0 to 1 V) using a standard impedance model for perovskite solar cells.[29,30] Figure 5.10a shows the typical Nyquist plots of complex resistance at three different bias voltages. The impedance spectra for all three bias voltages are dominated by a large semicircle at low frequencies. This large semicircle is often attributed to the charge recombination process within the perovskite

solar cells. Figure 5.10b compares the effect of R.H. on R_{rec} as a function of applied bias voltages. At each R.H. level, R_{rec} is strongly dependent on the applied bias voltage, following approximately an exponential decrease with voltage at the relatively high voltage range (>0.4 V). When compared at a constant bias voltage (e.g., 0.8 V), R_{rec} shows minimum change when the R.H. level is increased from 2% to 8%, and then decreases by 1–2 orders of magnitude with increasing R.H. level. This trend of R_{rec} change is consistent with the changes of the device characteristics (Figures 5.7), which can be correlated to the exposure of the substrate without $FAPbI_3$ coverage at high R.H. levels. The existence of pinholes or voids likely creates defect sites causing the reduction in V_{oc} as well as FF.

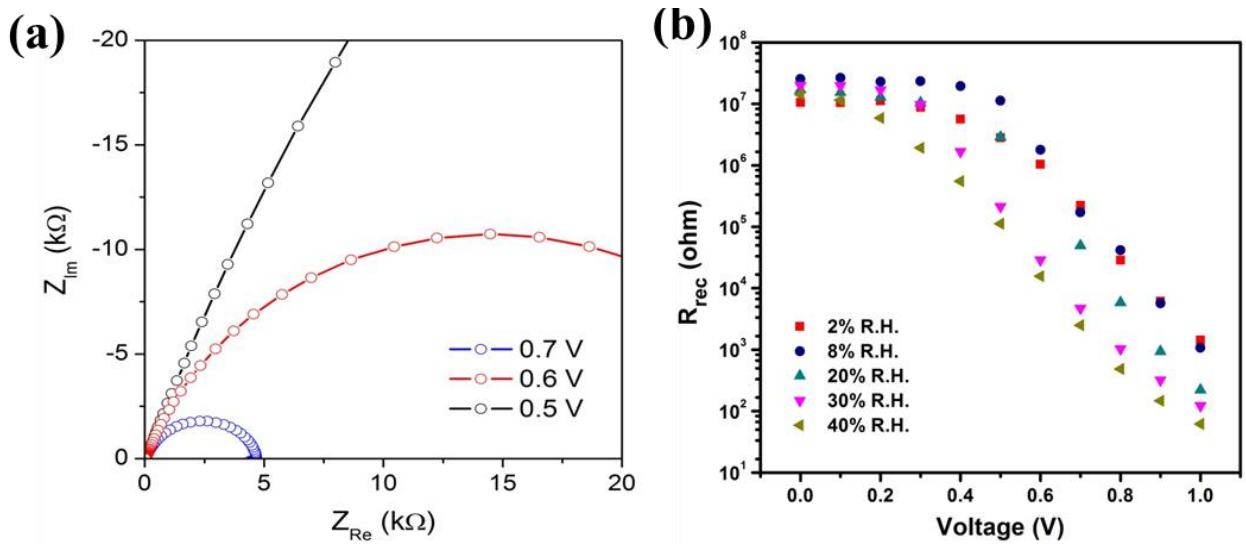

Figure 5. 10. (a) Nyquist plots of complex resistance at three different bias voltages, and (b) effect of relative humidity on the recombination resistance (R_{rec}) as a function of voltage for planar $FAPbI_3$ perovskite solar cells.

5.3.3.5 Time-resolved photoluminescence

These results are also consistent with the time-resolved photoluminescence (TRPL) measurement Figure 5.11 shows results from the TRPL study conducted for estimating the photo-generated carrier lifetimes in the FAPbI3 perovskite thin film prepared at low R.H. (~2%) are substantially longer than those prepared at relatively high R.H. (~20%).

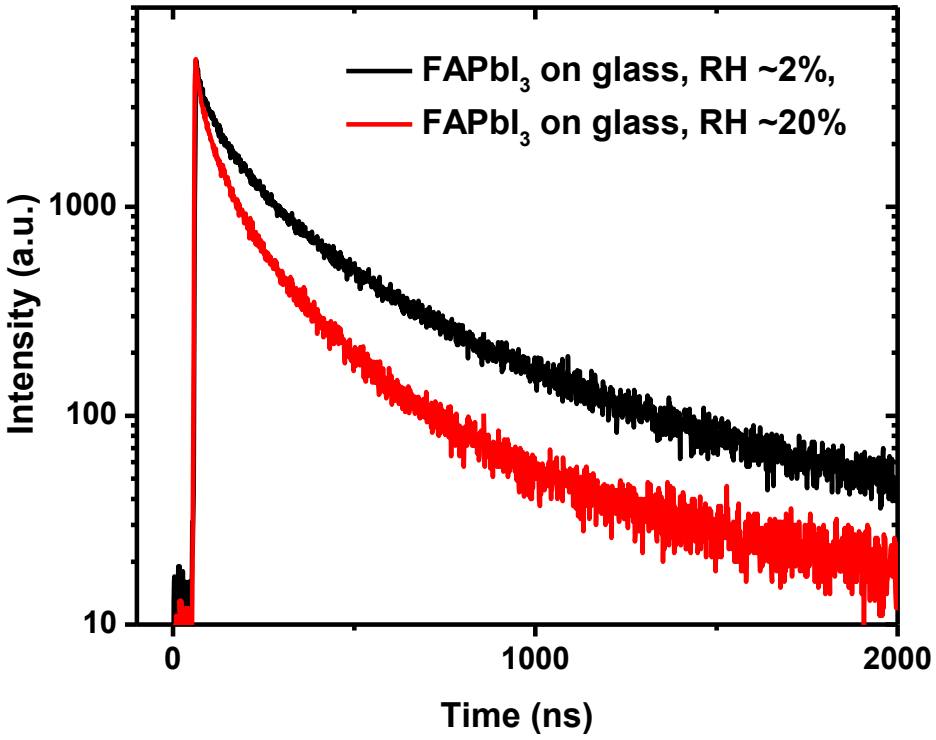

Figure 5. 11.TRPL measurements showing lifetimes for the FAPbI3 films prepared at 2 and 20% R.H. The curves were fitted to biexponential model.[4] For the 2% R.H. film, τ1 is 103 ns (75.8%) and τ2 is 522 ns (24.2%). For the 20% R.H. film, τ1 is 64.5 ns (83.8%), with a τ2 of ~352 ns (16.2%).

The TRPL curves were fitted to biexponential model. In general, the interpretation is that the fastest time constant (τ1) is associated with grain boundary/surface recombination whereas

the slower time constant (τ2) can indicate a lower bound for the bulk lifetime. Although the change in humidity did not show any major morphological changes, the change in lifetimes is substantial. For the 2%R.H. films, τ1 is 103 ns and τ2 is 522 ns. For the 40%R.H. films, τ1 is 64.5 ns, with a τ2 of ~522 ns. When τ1 is much smaller than τ2, one can estimate the surface recombination velocity (SRV) using the expression SRV=1/(α τ1), where α is the absorption coefficient.[35, 36] Using an absorption value of about 1.5×10^5 cm^{-1} (at 500 nm), we estimate a SRV of about 350 cm s^{-1}, which is substantially smaller than the conventional polycrystalline thin-film semiconductor absorbers (e.g., 10^4–10^5 cm s^{-1} for CdTe[35]). This indicates that films prepared at lower humidity maintain the preservation of the photo-generated carriers for a significantly longer duration before recombination.

5.4 Conclusions

In summary, we have fabricated $FAPbI_3$ planar heterojunction solar cells by a solvent engineering method under controlled humidity environments. In this approach, the relative humidity was controlled between about 2% and 40%, to evaluate the effect of moisture on $FAPbI_3$ thin films and device properties. The film morphology, crystallinity, and optical and electrical properties of $FAPbI_3$ differ significantly, depending on the relative humidity levels. Highly uniform and crystalline films were achieved for low relative humidity (2%), leading to 16.6%-efficiency devices with stabilized output at about 16.4%. As the humidity increases, $FAPbI_3$ films become inhomogeneous with the presence of voids, and the crystalline and optical properties are degraded. This deterioration of the films leads to lower device efficiencies (8.6% efficiency at 40% R.H.), mainly due to a loss in the V_{oc} and FF. The loss in V_{oc} with increasing humidity was consistent with the presence of the voids in the films, decrease in the

recombination resistance, and shorter carrier lifetimes. Our results indicate that moisture plays a crucial role during the fabrication of formamidinium-based perovskite solar cell. Low-humidity content leads to highest-efficiency devices, whereas increased humidity gradually degrades the properties of $FAPbI_3$ and the efficiencies of final devices.

5.5 References

(1) Gratzel, M. *Nature Materials* **2014**, *13*, 838.

(2) Green, M. A.; Ho-Baillie, A.; Snaith, H. J. *Nature Photonics* **2014**, *8*, 506.

(3) Jeon, N. J.; Noh, J. H.; Kim, Y. C.; Yang, W. S.; Ryu, S.; Seok, S. I. *Nat Mater* **2014**, *13*, 897.

(4) Jeon, N. J.; Noh, J. H.; Yang, W. S.; Kim, Y. C.; Ryu, S.; Seo, J.; Seok, S. I. *Nature* **2015**, *517*, 476.

(5) Mitzi, D. B. In *Progress in Inorganic Chemistry*; John Wiley & Sons, Inc.: 2007, p 1.

(6) Chakhmouradian, A.; Woodward, P. *Phys Chem Minerals* **2014**, *41*, 387.

(7) Eperon, G. E.; Stranks, S. D.; Menelaou, C.; Johnston, M. B.; Herz, L. M.; Snaith, H. J. *Energy & Environmental Science* **2014**, *7*, 982.

(8) Noh, J. H.; Im, S. H.; Heo, J. H.; Mandal, T. N.; Seok, S. I. *Nano Letters* **2013**, *13*, 1764.

(9) Zhao, Y.; Nardes, A. M.; Zhu, K. *The Journal of Physical Chemistry Letters* **2014**, *5*, 490.

(10) Zhao, Y.; Zhu, K. *Journal of the American Chemical Society* **2014**, *136*, 12241.

(11) Ogomi, Y.; Morita, A.; Tsukamoto, S.; Saitho, T.; Fujikawa, N.; Shen, Q.; Toyoda, T.; Yoshino, K.; Pandey, S. S.; Ma, T.; Hayase, S. *The Journal of Physical Chemistry Letters* **2014**, *5*, 1004.

(12) Boix, P. P.; Nonomura, K.; Mathews, N.; Mhaisalkar, S. G. *Materials Today* **2014**, *17*, 16.

(13) Sanchez, R. S.; Gonzalez-Pedro, V.; Lee, J.-W.; Park, N.-G.; Kang, Y. S.; Mora-Sero, I.; Bisquert, J. *The Journal of Physical Chemistry Letters* **2014**, *5*, 2357.

(14) Eperon, G. E.; Burlakov, V. M.; Goriely, A.; Snaith, H. J. *ACS Nano* **2013**, *8*, 591.

(15) Lee, J.-W.; Seol, D.-J.; Cho, A.-N.; Park, N.-G. *Advanced Materials* **2014**, *26*, 4991.

(16) Koh, T. M.; Fu, K.; Fang, Y.; Chen, S.; Sum, T. C.; Mathews, N.; Mhaisalkar, S. G.; Boix, P. P.; Baikie, T. *The Journal of Physical Chemistry C* **2013**, *118*, 16458.

(17) Lv, S.; Pang, S.; Zhou, Y.; Padture, N. P.; Hu, H.; Wang, L.; Zhou, X.; Zhu, H.; Zhang, L.; Huang, C.; Cui, G. *Physical Chemistry Chemical Physics* **2014**, *16*, 19206.

(18) Pang, S.; Hu, H.; Zhang, J.; Lv, S.; Yu, Y.; Wei, F.; Qin, T.; Xu, H.; Liu, Z.; Cui, G. *Chemistry of Materials* **2014**, *26*, 1485.

(19) Pellet, N.; Gao, P.; Gregori, G.; Yang, T.-Y.; Nazeeruddin, M. K.; Maier, J.; Grätzel, M. *Angewandte Chemie International Edition* **2014**, *53*, 3151.

(20) Lee, J.-W.; Lee, S. H.; Ko, H.-S.; Kwon, J.; Park, J. H.; Kang, S. M.; Ahn, N.; Choi, M.; Kim, J. K.; Park, N.-G. *Journal of Materials Chemistry A* **2015**.

(21) Wang, F.; Yu, H.; Xu, H.; Zhao, N. *Advanced Functional Materials* **2015**, *25*, 1120.

(22) Hanusch, F. C.; Wiesenmayer, E.; Mankel, E.; Binek, A.; Angloher, P.; Fraunhofer, C.; Giesbrecht, N.; Feckl, J. M.; Jaegermann, W.; Johrendt, D.; Bein, T.; Docampo, P. *The Journal of Physical Chemistry Letters* **2014**, *5*, 2791.

(23) Aharon, S.; Dymshits, A.; Rotem, A.; Etgar, L. *Journal of Materials Chemistry A* **2015**.

(24) Wu, X.; Yu, H.; Li, L.; Wang, F.; Xu, H.; Zhao, N. *The Journal of Physical Chemistry C* **2015**, *119*, 1253.

(25) Christians, J. A.; Miranda Herrera, P. A.; Kamat, P. V. *Journal of the American Chemical Society* **2015**, *137*, 1530.

(26) Habisreutinger, S. N.; Leijtens, T.; Eperon, G. E.; Stranks, S. D.; Nicholas, R. J.; Snaith, H. J. *Nano Letters* **2014**, *14*, 5561.

(27) You, J.; Yang, Y.; Hong, Z.; Song, T.-B.; Meng, L.; Liu, Y.; Jiang, C.; Zhou, H.; Chang, W.-H.; Li, G.; Yang, Y. *Applied Physics Letters* **2014**, *105*, 183902.

(28) Etgar, L.; Gao, P.; Xue, Z.; Peng, Q.; Chandiran, A. K.; Liu, B.; Nazeeruddin, M. K.; Grätzel, M. *Journal of the American Chemical Society* **2012**, *134*, 17396.

(29) Juarez-Perez, E. J.; Wuβler, M.; Fabregat-Santiago, F.; Lakus-Wollny, K.; Mankel, E.; Mayer, T.; Jaegermann, W.; Mora-Sero, I. *The Journal of Physical Chemistry Letters* **2014**, *5*, 680.

(30) Christians, J. A.; Fung, R. C. M.; Kamat, P. V. *Journal of the American Chemical Society* **2014**, *136*, 758.

Chapter 6 *In-situ* investigation of the role of temperature on the formation of higher efficiency perovskite solar cells*

6.1 Introduction

The development and implementation of new photovoltaic (PV) materials are intertwined with major technological achievements in energy and semiconductor device fabrication.[1-3] Today's photovoltaics and portable electronic devices have similar requirements for energy: they must be highly efficient (> 15 %), have a large capacity for long-term manufacturing, extended for long lifetimes, and be environmentally friendly.[2-7] Perovskite-based solar cells (PSCs) are attractive PV materials due to their impressive properties as light harvesters, high device efficiencies, and low-cost, industry-scalable processing.[2-11] However, the materials basis needed to underpin the dynamical processes that occur during processing and their subsequent device applications is currently limited in the literature.[9,12-16] Fundamental studies are urgently needed to understand the relationships between the microstructural modification and resulting properties as a function of the processing environment.

Perovskite-based solar cells performance would greatly benefit from direct observation of the synthesis process, especially as the range of perovskite-based materials expands and various Edisonian recipes are devised for fabrication.[6,17,18] Insights into the mechanisms for perovskite formation from the inorganic and organic components are still generally lacking. [6,17] It has been widely reported that PSCs performance varies with time, temperature, humidity, and synthetic conditions.[14,19-21]

*This chapter was adapted from: Wozny, S.; Aguiar, J.; Holesinger, T.; Aoki, T.; Patel, M.; Yang, M.; Zhou, W.; Zhu, K.; and Al-Jassim, M.; *In-situ* investigation of the role of temperature on the formation of higher efficiency perovskite solar cells *Submitted*

Hence, there is a tremendous need for research on the fundamental formation mechanisms and environmental influences regarding these new PV materials. Understanding the related phase and structural equilibria is required to minimize the physical, electrical, and chemical barriers to higher efficiencies across several cell processes in the community.[15,18,20,22-27]

To address these challenges,[28] we undertook an *in-situ* growth study using (scanning) transmission electron microscopy (S/TEM) for direct observation of the synthesis and formation pathways associated with $FAPbI_3$ (FA-based perovskite). Thin perovskite films were fabricated from FAI/PbI_2 precursors solution on titania-coated Si_3N_4 chips that were placed in a specialized *in-situ* gas S/TEM hot stage that allowed for gas flow around the specimen at atmospheric pressures.[29] We specifically show that (i) optimal processing and annealing of $FAPbI_3$ at 175° C measured inside the *in-situ* gas cell is directly related to the mobility and subsequent intergranular diffusion of lead at grain boundaries, and (ii) about this temperature a partially reversible process occurs involving the exchange of lead at grain boundaries. We also show that (iii) beyond 175° C, coarse particle nucleation and growth into individual nanometer precipitates occurs. These meta-stable precipitates are pinned at grain boundaries and grain boundary related triple junctions, they can only be partially reincorporated into the material following a longer anneal at 175° C. Furthermore there is direct evidence (iv) of the adsorption of hydrogen at the interface regions, owing to the idea that there is a direct ionic exchange of presumably OH^-, H^+, and FA^+ ions under thermal cycling. This potentially leads to hydrolysis that compromises the structural integrity of the trigonal perovskite framework. Taken together, this works identifies key aspects associated with the $FAPbI_3$ formation process and the structure-property links between measured device performance and PSCs process history leading to improvements upon the current state of FA-based PSCs.

6.2 Experimental

In this study, the *in-situ* S/TEM approach has been used to directly visualize the stages of crystallization, nucleation, and growth of $FAPbI_3$ using the commercially available Hummingbird Scientific *in-situ* gas system.

6.2.1 *In-situ* gas experiment design

The *in-situ* gas cell is comprised of a silicon microchip and silicon nitride viewing membrane that forms a viewing port. A Schematic of the experimental design is shown in Figure 6.1. The cross-section of the differentially pumped cell in Figure 6.1a depicts how the electron beam interacts through the silicon nitride (Si_xN_y) windows and how elastically scattered electrons are collected for bright field (BF) and annular dark field (ADF) atomic contrast STEM imaging with nearly a 1.4 Å probe. For our experiments, 25 nm thick silicon nitride windows were used. Silicon nitride (Si_3N_4) microchip spacers and standard windows were both prepared first by spray coating compact titania on the hot SiN microchips (450°C) using 0.2 M solution of Ti(IV) bis(ethyl acetoacetate)-diisopropoxide in 1-butanol and subsequently annealed in air at 450 °C for 1 hour (Figure 6.1c1). Following the annealing, a 30 minutes ultraviolet (UV) treatment was performed to roughen the active surface hour (Figure 6.1c2). A 0.7M perovskite solution was prepared from stoichiometric amount of lead iodide (PbI_2) and FAI in DMF and immediately deposited on the surface of the microchip with the help of a micropipette hour (Figure 6.1c3). Optical imaging confirmed that the presence of perovskite suspended over the hole was intact with no visible ruptures or cracks. This approach was quite effective, with more than 80% of dropping attempts yielding perovskite solution after SEM and optical inspection. The silicon nitride spacer chip thereby was made up of the following layering:

perovskite/compact titania/amorphous silicon nitride. The treated chip was then placed into the Hummingbird Scientific *in-situ* heated gas holder shown in Figure 6.1b. A calibrated silicon heating chip with a ±3º C certainty was then placed face-to-face with the treated silicon nitride spacer. Once positioned into the holder, the system was sealed using O-ring seals, a cover plate,

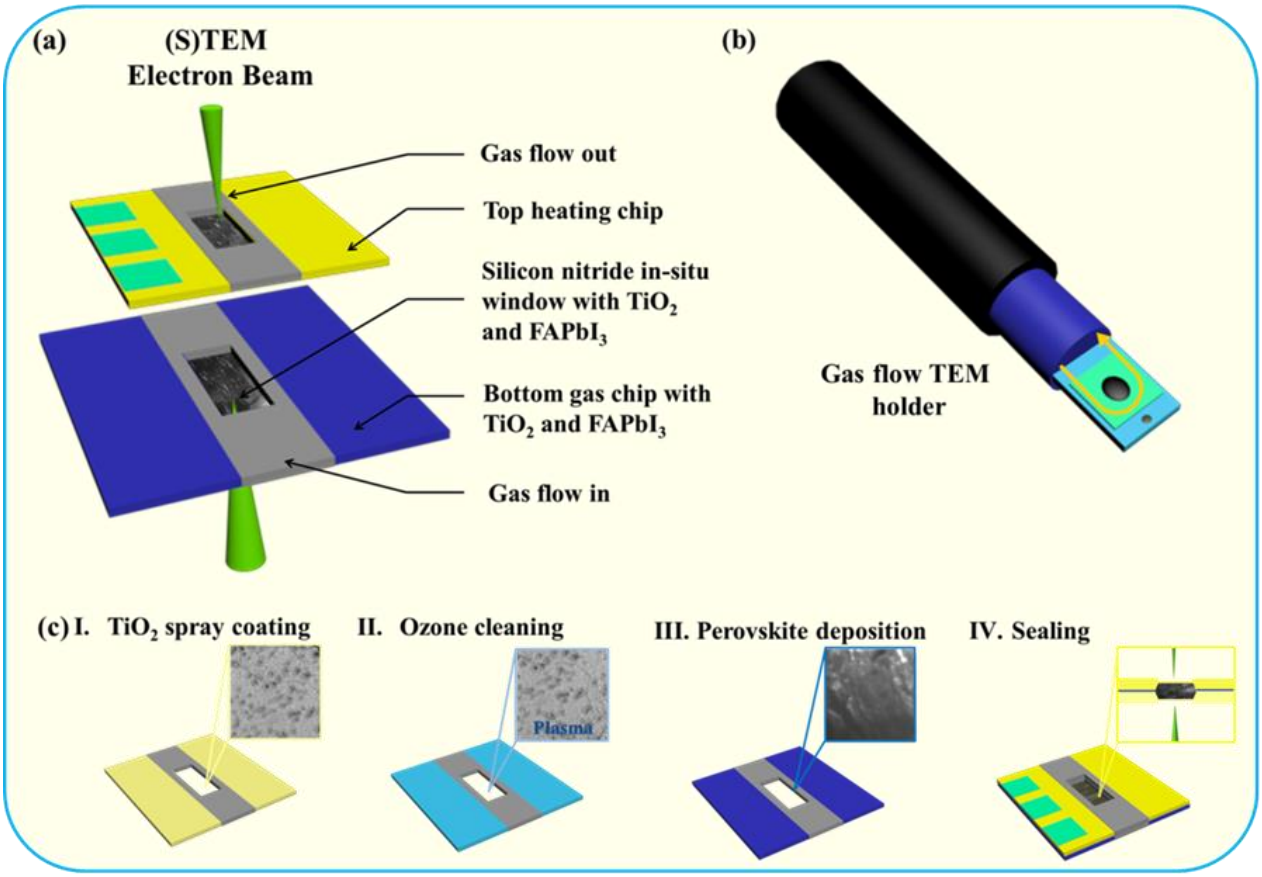

Figure 6. 1. Schematic of the experimental design: a) Schematic of the heated in-situ gas cell used for the controlled temperature study of FA-based PSCs inside with heating capability from 50°C to 225°C while flowing inert argon gas, b) Schematic of the gas flow holder, and (c) schematic of the step by step sealing of the silicon nitride microchips.

retention clip, and then secured with a single setscrew. The system was then leak checked to ensure high vacuum could be attained using a dry pump vacuum station. Following leak testing,

argon gas was also delivered to the system to check the vacuum seals under pressure. The system was then placed in a transmission electron microscope. Before observation, argon gas was delivered to the gas cell using hard metallic tubing to deliver and flush the cell for 30 min prior to heating and transmission electron microscopy. During this time the cell was checked for leaks. The *in-situ* S/TEM conditions were then chosen to generate a comparative study to fabricating PSCs based solar cells. Inert argon gas was then continually flowed until observation and initial heating. During observation, inert argon gas was continually flowed at 0.1 cm^3 min^{-1} and the temperature was allowed to be ramped and held at various temperatures between 50 ºC and 225 ºC.

6.2.2 Analytical materials characterization and transmission electron microscopy

6.2.2.1 *In-situ* (scanning) transmission electron microscopy

Simultaneously with the *in-situ* heating gas experiments, bright field (BF), annular dark field (ADF), selected area electron diffraction (SAED), and transmission electron micrographs were recorded using a Cs aberration-corrected FEI Titan S/TEM operated at 300 kV with a 4350 V extraction voltage and FEI Tecnai at 300 kV. Prior to observation the specialized *in- situ* gas holder was initially purged and filled internally. Observation of the material was performed while flowing argon gas (0.1 cm^3 min^{-1}). The ADF and BF STEM images were collected on the Cs aberration-corrected FEI Titan S/TEM operated at 300 kV using a Fischione model 3000 high angle annular dark field STEM detector and the BF STEM images were acquired using Gatan GIF camera using Gatan Digital Micrograph software. The following imaging conditions were used for ADF STEM imaging: 40kx magnification, -0.050 um defocus, 70 mm final probe forming condenser aperature, 100 mm nominal camera length, roughly 1.6 Å probe diameter, 86

pA probe current, 42.9 mrad convergence semi-angle and 55–330 mrad inner and outer collection semi-angle, an image size of 2048 x 2048 pixels, 871 pm x 871 pm pixel size, sample 1.78 μm x 1.78 μm area, 1 μs pixel dwell time, and with a 5.64 s frame time was used. Images were time stamped and recorded initially, and then stacked to form movie-like snapshots.

6.2.2.2 *In-situ* transmission electron microscopy for selected area electron diffraction

Polycrystalline diffraction ring patterns were collected using the same temperature profiles used for the *in-situ* scanning transmission electron microscopy. The nominal magnification was kept above 20 kx and 330 mm camera length on LaB_6 equipped FEI Tecnai.

6.2.2.3 Low accelerating voltage scanning transmission electron microscopy

Energy filtered aberration corrected high resolution STEM imaging was performed using monochromated Nion Ultra STEM equipped with a cold-field emission gun as the electron source and capable of spherical aberration correction of the third and fifth order aberrations. The STEM was operated at 60 kV and less than 10 pA beam current, which is below the knock-off damage of most carbon-based materials, including graphene. Low (BF), medium (MAADF), and high angle annular dark field (HAADF) STEM 1024 x 1024 pixel images were acquired with a convergence of 30 mrad and a collection semi-angle of 50-200 mrad with a 64 us dwell time to sample a 20 nm x 20 nm area. Multiple raw images were collected, cross correlated, and summed over a period of 5 mins to minimize beam dose. Prior to STEM, the perovskite specimens were annealed at 170ºC for 10 mins and then placed in a dedicated double tilt that was baked under vacuum at 160ºC for 8 hours.

6.2.3 High resolution valence electron energy loss spectroscopy

All valence electron energy loss spectra (VEELS) were taken in Scanning Transmission Electron Microscopy (STEM) mode. Ångström sized probes were used with Full-Width Half-Maxima (FWHM) of the ZLP ranging nearly 20 meV for 1s spectrum acquisitions. The microscope used for this study was specifically chosen to capture the valence nature of perovskite materials. The cold Field Emission Gun (FEG) of the Nion UltraSTEM was operated at 60 kV and 40 kV acceleration voltages with a 30 mrad probe convergence and 45 mrad collection angle at 60 kV. These conditions provide the best native energy spread of nearly 10-20 meV, based on the zero-loss peak FWHM, measured with 0.02 eV/pixel dispersion through a large solid acceptance angle into the spectrometer which was obtained with a reduced extraction voltage resulting in a probe current of about 8 pA. For imaging, a 30mrad convergence semi angle and 30 mrad /15mrad (lawless) EELS collection angles was used. VEELS collection was performed with a 12mrad convergence semi angle and 15mrad EELS collection angle.

Gentle beam conditions and multiple frame acquisition were performed following the routines and discussions in the open literature[30-32]. Beam focusing was further checked to assure proper alignment into the spectrometer aperture opening. Spectra were then analyzed and processed to subtract residual background associated with sampling on a silicon nitride substrate. To perform the subtraction, several raw silicon nitride, vacuum zero loss, and dark count reference VEELS profiles were collected at the same time of collection. The scaled zero-loss peak subtraction routine outlined in Aguiar *et al.* was then applied to resolve subtracted spectra profiles[33]. Subtraction of the silicon nitride signal was then performed via the same technique, where the silicon nitride VEELS subtracted profiles where fit against collected perovskite VEELS profiles.

6.2.4 Chemical spectral imaging

Complementary, composite spectral imaging using STEM-based energy dispersive x-ray spectroscopy was performed on an as-completed perovskite film in planar view on silicon nitride. To resolve the final chemistry, the perovskite sample was loaded on a single tilt low background holder and placed in the aberration corrected FEI Titan operated and a significant monochromated defocus was used to reduce the beam current. A host of composite chemical images, where then performed including both line and two-dimensional line scans.

6.2.5 *In-Situ* X-Ray diffraction

Due to the hygroscopic nature of the as-synthesized $FAPbI_3$ it was difficult to identify the phases evolved during the synthesis process. Thus, *in-situ* high temperature XRD was performed using an Anton Parr HTK 1200N oven heated stage mounted on the Panalytical Empyrean XRD system. The high temperature stage is mounted on a z-stage to allow for automatic sample height adjustment during the high temperature cycle in order to account for the thermal expansion of the material. Thin film of precursors (FAI/PbI_2) deposited on a compact titania/FTO Glass substrate were mounted on an Al_2O_3 sample holder and heated from room temperature (25°C) to 225°C in air with a heating rate of 30°C/min. XRD measurements were performed in conventional 2θ-ω configuration since the films were thick enough to prevent the x-rays from interacting with the substrate. The measurements were performed using Cu-Kα x-rays and an incident beam configuration that comprised of an elliptical focusing mirror with a 1/16° divergence slit, a beam mask of 4mm and 0.04° soller slits. The diffracted x-rays were detected using a position sensitive PIXcel^{3D} detector in a linear 1D scanning mode capable of simultaneously collecting data over 3.35° region. The data was collected in the 2θ range of 10°

to 70° with a step size of 0.013° and a step time of 48.2 sec/step which resulted in a total collection time of 15 min for these XRD patterns. In order to study the dynamical evolution of phases in the film, XRD data was also collected with very short step times of 18.9 sec/step, which resulted in a total collection time of 6 min for these XRD patterns.

6.2.6 Device fabrication and characterization

Parallel to the *in-situ* studies perovskite solar cell devices were prepared by spray coating c-TiO_2 compact blocking layer on a pre-patterned 1x1 inch Fluorine-doped SnO_2-coated transparent conducting glass (FTO/Glass) substrate. [10] The perovskite thin films were spin coated from a 0. 7M solution of lead iodide (PbI_2) and formamidinium (FAI) in N,N'-dimethylformamide (DMF). The substrate was subsequently annealed with temperatures ranging from 150ºC to 225ºC for 10 min.[21] The film was cooled for 1 min, before spin coating the 2,2',7,7'-tetrakis(N,N-dip-methoxyphenylamine)-9,9'-spirobifluorene (spiro-OMeTAD) solution on the warm substrate for 30 seconds at 4000 rpm. Finally, silver electrodes were thermally evaporated to evaluate the performance of the device.[21] The photocurrent−voltage (J−V) characteristic of $FAPbI_3$ perovskite solar cells were measured with a Keithley 2400 source meter connected to a Oriel Sol3A class AAA solar simulator under simulated AM 1.5G illumination (light irradiation of 100 $mW.cm^{-2}$). Impedance spectroscopy (IS) on the PSCs was carried out using a PARSTAT 2273 workstation (Princeton Applied Research) with the frequency range of 0.1 Hz−100 kHz and the modulation amplitude of 10 mV. The IS spectra were analyzed using ZView 2.9c software (Scribner Associates).

6.3 Results

6.3.1 *In-situ* observation of PSC formation

We performed *in-situ* high-resolution transmission electron microscopy under both imaging and diffraction conditions to track the effects of thermal processing on the structure and morphology associated with FA-based PSCs. Our *in-situ* heating experiments are focused around 175ºC based on literature reports of this temperature figuring prominently in device fabrication. We then work with three successive excursions from this base temperature to examine, and in some cases, exaggerate the effects of higher temperatures on structure. The effects of thermal cycling on the $FAPbI_3$ thin film are shown in Figure 6.2 where the series of S/TEM plan-view images, provides snapshots of the microstructure at specific temperatures and times consistent with the temperature profile from 50°C to 225°C, while purified inert argon gas was flowing at 0.5 cm^3/min. as shown in Figure 6.3. Note that the current *in-situ* holder setup does not allow for controlled ramp rates and temperature changes occur within a few seconds. Within each S/TEM image, the contrast is directly related to the atomic number of the material, where the bright contrasted regions consist of lead-containing rich regions while the darker regions are FAI precursor or $FAPbI_3$ perovskite. Sequential changes in the distribution of the lead-containing species are resolved by observing the differences in image contrast. Starting at room temperature (25°C, Figure 6.2a), the material is polycrystalline and $FAPbI_3$ has not yet formed. Raising the temperature to 50°C (Figure 6.2b) and then 150°C (Figure 6.2c), with 10 minutes dwells at each temperatures, we observe a slight coarsening of the grain morphology. The initial material is

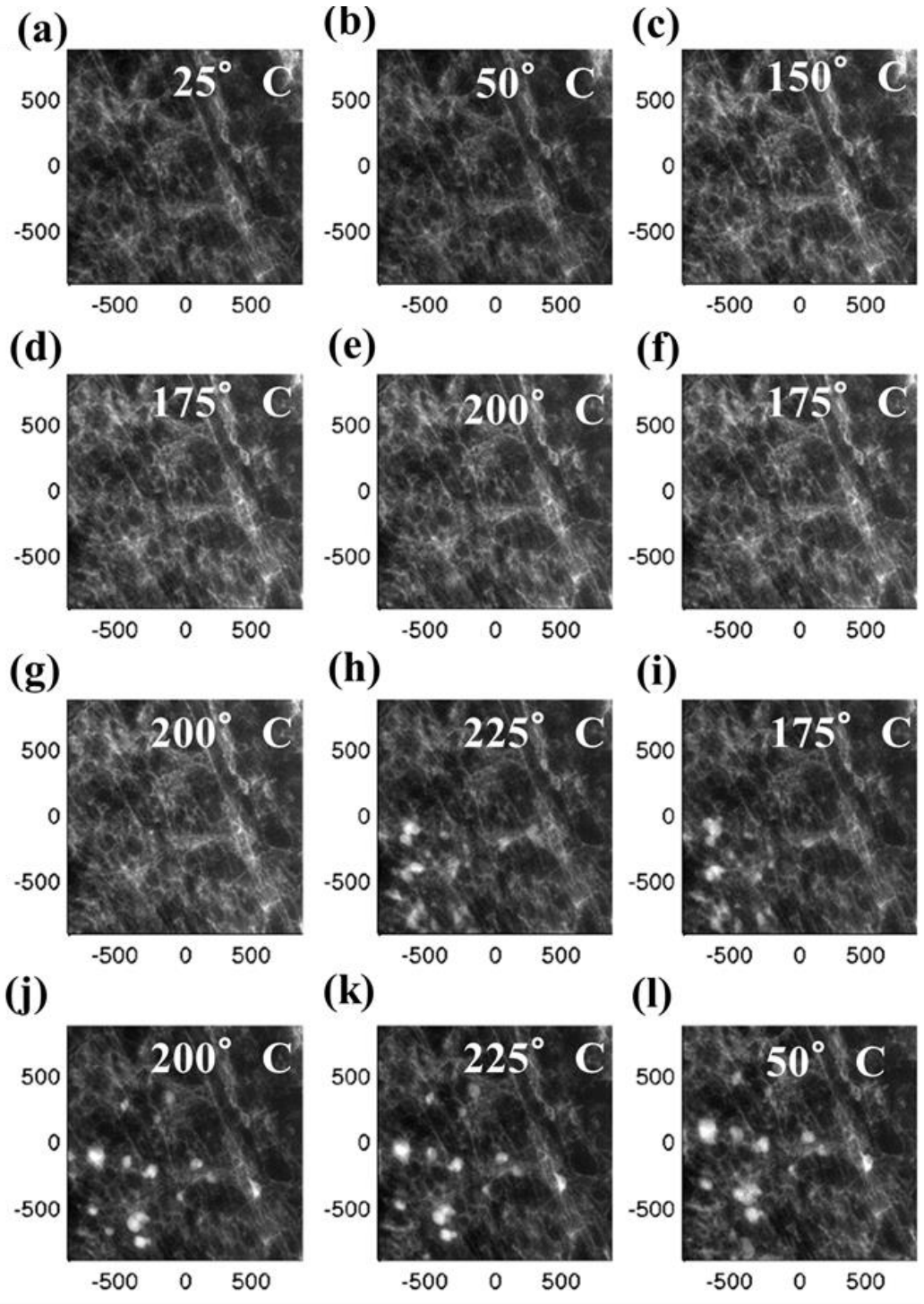

Figure 6. 2. To resolve the evolving microstructure and evolution of $FAPbI_3$ we performed a controlled temperature study of FA-based PSC inside a heated *in-situ* gas cell from 50°C to 225°C while flowing inert argon gas. To track the microstructure atomic contrast STEM plane-view imaging was performed over a specific temperature profile which is shown in Figure 6.3.

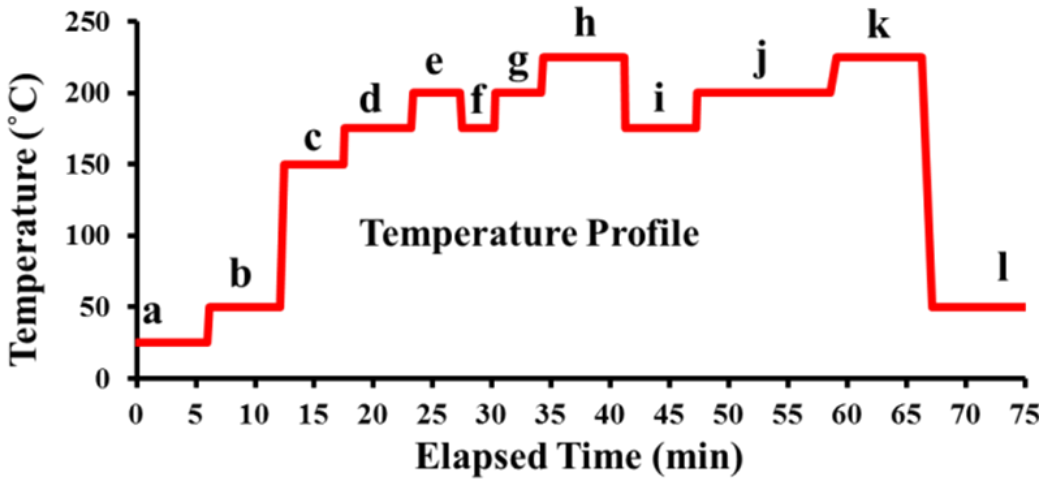

Figure 6. 3. shows the specific temperature profile used to resolve the evolving microstructure of $FAPbI_3$ inside a heated *in-situ* gas cell from 50°C to 225°C while flowing inert argon gas.

converted into $FAPbI_3$ between these temperatures based diffraction data. On raising the temperature to 175°C (Figure 6.2d), we observe the start of lead iodide (PbI_2) segregation to the boundaries. A further increase in temperature to 200°C (Figure 6.2e), results in the distinct formation of lead-containing particles along the boundaries. Dropping the temperature to 175°C (Figure 6.2f) allows then for lead to reincorporate into the perovskite grain boundaries. The observed improvement in uniformity along the grain boundaries is based on comparing the initial image contrast starting at 25°C against the increasing outlining grain contrast observed in subsequent images. At this point from the perspective of device performance (see below), the grain morphology is the most uniform following the sequential drop to 175°C. However for the purposes of this study, we carried out the *in-situ* experiment further, to demonstrate the partial reversibility and segregation of the lead-containing species. Sequentially raising the temperature again from 175°C, to 200°C (Figure 6.2g) and finally to 225 °C (Figure 6.2h), we observe additional, larger lead containing particles at grain boundaries. At this point, a subsequent drop

and anneal at 175 °C for 10 minutes (Figure 6.2i), shows a gradual decrease, but incomplete reduction in the size of these large particles. The formation / dissolution of the lead-containing particles is only reversible up to a point. After this second anneal at 175 °C, we again increased the temperature to 200°C (Figure 6.2j) followed by 225°C (Figure 6.2k) to further demonstrate that the lead-containing species is still mobile and even more relatively large and stable lead-containing particles have formed. Completing the experiment, the temperature of the cell was dropped to 50°C (Figure 6.2l) locking in the high temperature microstructure.

Figure 6.4 is a complementary structural timeline focused on the formation of $FAPbI_3$ by collecting selected area electron diffraction (SAED) and performing a background subtracted azimuthal integration as discussed in detail by Gammer *et al*.[34] The series tracks the phase evolution as function of increasing temperature under the same heated inert gas environmental conditions. The finite time needed to collect an x-ray diffraction pattern does add some difficulty in tracking the microstructural changes during sampling of the controlled *in-situ* growth. However we are able to make the following observations:

(*i*) By 160 °C, the FAI and PbI_2 are crystallized into perovskite, at which point the peaks identified as PbI_2, silicon nitride, or perovskite are indeed the precursor material.

(*ii*) Beyond 160 °C, there is a shift in the profiles towards lower d-spacing.

(*iii*) At the elevated temperatures, the profiles continue without significant alternation, until eventually at 225 °C we observe a significant presence of the (012) (2.58 Å) peak related to corresponding PbI_2 phase. We believe beyond 175 °C, the lead iodide starts to segregate out, as observed in Figure 6.2. Together these consecutive snapshots form the basis of our study on the evolution on FA-based PSCs using S/TEM and complementary SAED.

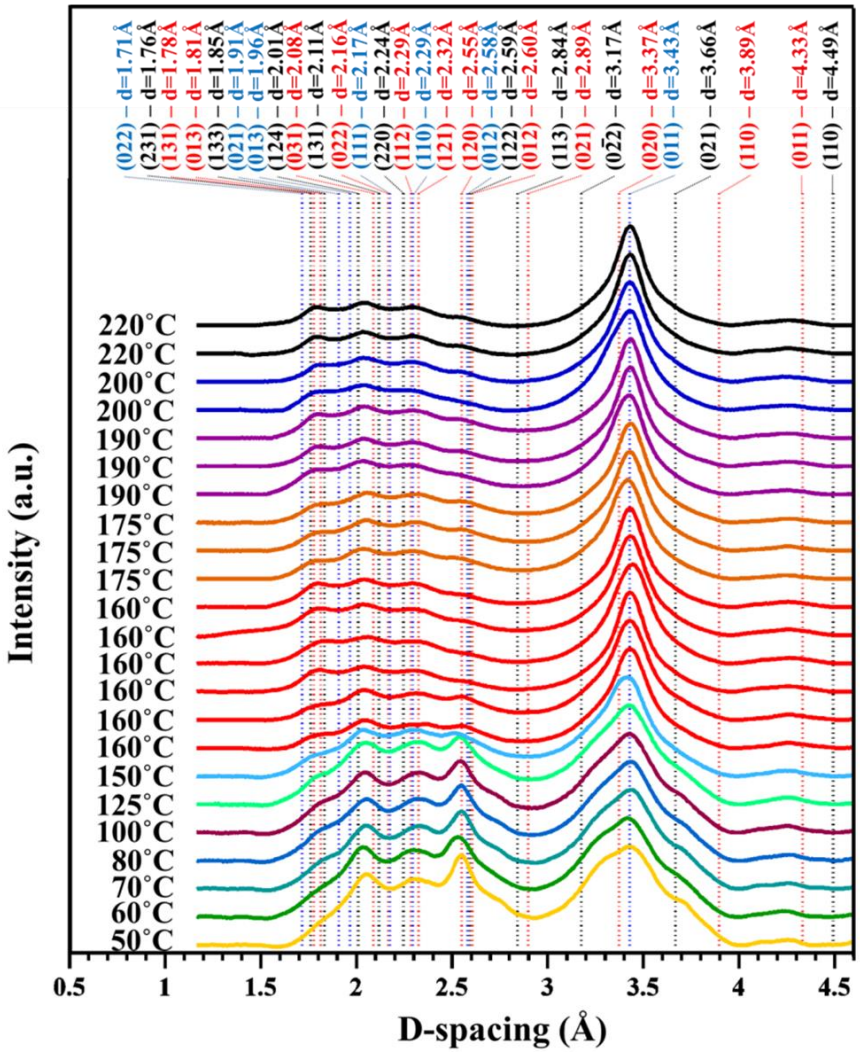

Figure 6. 4.a) To resolve the evolving microstructure and evolution of $FAPbI_3$ we performed a controlled temperature study of FA-based PSC inside a heated *in-situ* gas cell from 50°C to 225°C while flowing inert argon gas. Consistent with *in-situ* STEM imaging, we performed a series of repeated experiments, including collecting selected area electron diffraction (SAED) polycrystalline ring patterns in nanodiffraction mode for the same experimental conditions. The result is a temperature resolve azimuthal projected line profile based on collecting polycrystalline ring patterns, subtracting the background, and projecting onto a 2-dimensional angular resolved plot. The profiles are further indexed against the colored lines representing crystallographic lattice spacings corresponding to PbI_2 (blue), the perovskite (black) and the Si_3N_4 (red) microchip. These series of results track the structure and chemistry of the formation of FA-based perovskite material forming the basis of our study.

6.3.2 Detailed Structure and Composition of Polycrystalline $FAPbI_3$ PSC Annealed at 175°C

Figure 6.5 is a static image of the as-grown polycrystalline and 175°C annealed perovskite material. Under the high-resolution kinematic conditions, the interplay between atomic structure and chemistry is elucidated through a high resolution point-resolved valence electron energy loss spectroscopy (VEELS) scan traversing a grain boundary. Figure 6.5a is the raw normalized VEELS spectral scan that characterizes the low loss region of the electron energy-loss spectrum (0-35 eV), where features due to optical modes, valence band transitions, OH^-, and H^+ ions can be detected.[35-37] The projected VEELS STEM-based spectral scan is the result of a horizontally summed and averaged 2-dimensional image over the grain boundary indicated in Figure 6.5b (STEM Images). The bright grain has been oriented close to a neighboring zone-axes. To further help identify the individual spectral features the linescan we followed a modified linear-least squares routine to subtract both the zero-loss and background VEELS signal associated with the silicon nitride substrate as discussed in detail elsewhere by Aguiar *et al.*[33] Following this background subtraction, we identify three specific electronic energy loss regimes for comparison of the signals from the grain interior and boundary regions. Figure 5c is a comparison of the VEELS spectra from the collected grain interior and boundary regions extending from 0 eV to 35 eV. This residual spectral comparison contains the band-edge onset associated with PbI_2 at roughly 2.36 eV, the OH^- spectral feature at 6.2 eV, discussed in detail by Bradley *et al.* [38], and the hydrogen 1*s* and lead ionization thresholds. In addition, the elemental bonding state differences are also resolved within their corresponding spectral shapes and characters. From lower to higher energy loss we will now discuss each of the spectral

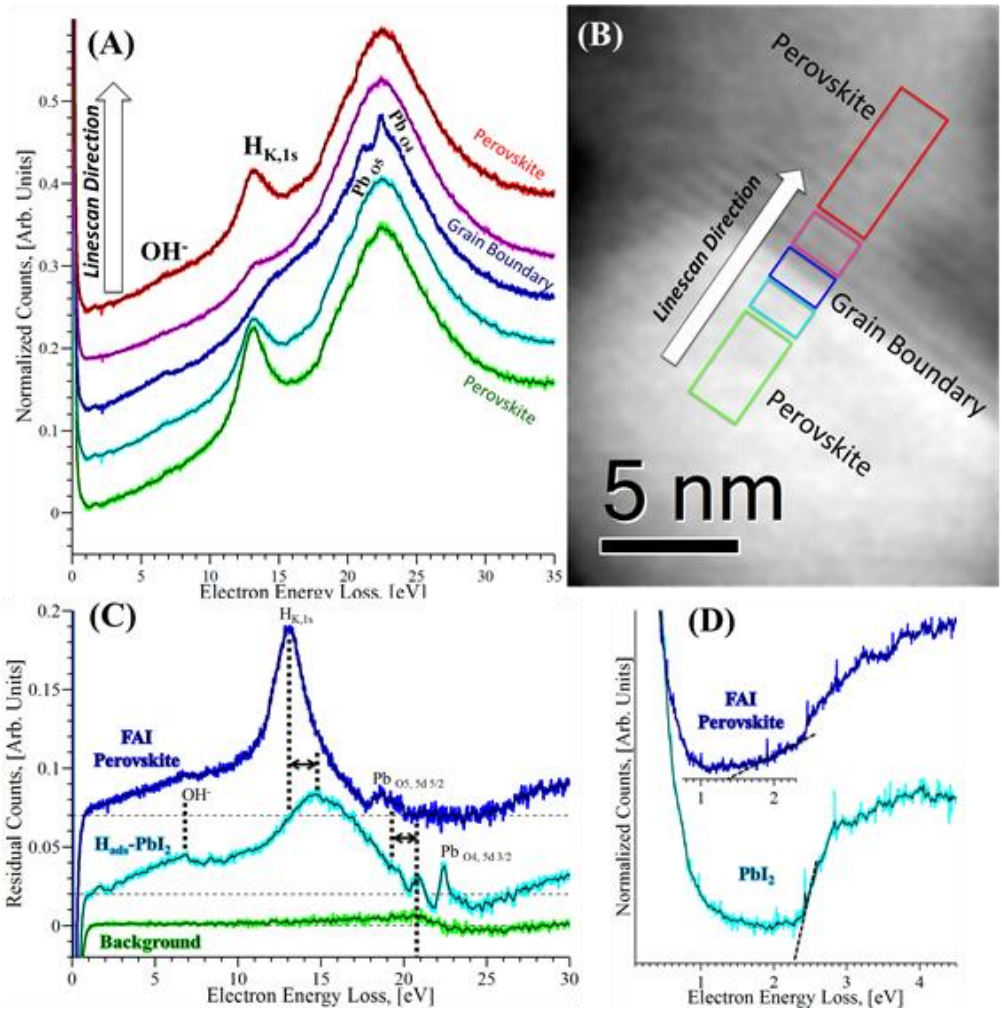

Figure 6. 5. Tracking *in-situ* studies, static imaging of an representative as-grown perovskite device material anneal at 175°C for 10 minutes was imaged with higher resolution aberration corrected gentle STEM and (a) profiled across a grain with point resolved energy filtered valence electronic energy loss spectroscopy (VEELS) spectral imaging at 60 kV. b) Under these imaging conditions, a highly polycrystalline sample was thereby oriented to a nearly kinematic condition and high resolution VEELS (HR-VEELS) line profiling was performed near and at a grain boundary. c) Following analyses of the collected raw VEELS profiles was processed to subtract the residual background from the supporting silicon nitride substrate, resolving and comparing the presence of carbon, hydrogen, OH-, and lead between the perovskite grain interior and boundary region. d) Higher resolution aloof beam VEELS confirms PbI_2 as an identified segregated species, as well as perovskite, in line with the *in-situ* observations.

features in detail. Figure 6.5d is a higher resolution aloof comparison of the valence structure between 0 eV and 4.5 eV. It clearly identifies both the subtle yet sharp band-edge onset at 2.36 eV associated with PbI_2 and the onset of the valence band of perovskite at roughly 1.4 eV based on extending fit to VEEL spectra, with a significant broadening up to band-edge onset of PbI_2. Each of these spectra were acquired under aloof beam conditions at 40 kV, where the energy resolution is measured to be 10 meV or better[39]. The band gap associated with perovskite has been measured reported to be roughly 1.5 eV with UV, however looking closer in these reports there is significant edge tailing to lower energy, which is consistent with the current aloof beam VEELS profiles [21].

Nearby at roughly 6.2 eV, we also resolve the presence of the hydroxyl group (OH^-) segregated to the boundary region. The OH^- spectral feature is broadened, which would be expected from a multiple bonding state configuration. At slightly higher energy loss we can compare the resolved H_K^{1s} ionization edge profiles which show a narrower peak within the perovskite domain compared to the boundary. The difference in hydrogenic profile can be attributed to the presence of a strong singlet bonding state within the perovskite interior. Given the electronic open shell configuration of hydrogen and presumed differences in atomic ordering at the boundary, several free-surfaces like bonding configurations are possible including the effects discussed associated the broadened OH^- profile and shift in the H_K^{1s} ionization edge profile. The third region of interest resolved in Figure 6.5 extends from 17 eV to 30 eV and contains a comparison of the bonding state associated with lead between the grain interior and boundary. At the boundary, we resolve the presence of both the Pb_{O5} and Pb_{O4} ionization edges, which suggests a split bonding state, presumably due to the presence of oxygen. The spectra from the grain interior of the perovskite shows only the Pb_{O5} ionization edge, suggesting a singlet

bonding state with neighboring iodine. The singlet peak is expected, where the lead is coordinated in tetrahedron with iodine within $FAPbI_3$. Hence, the results from the VEELS profiling clearly show the differences in the chemical nature of the polycrystalline perovskite. These differences between the grain boundary and grain interiors provide a mechanistic view of how the material equilibrates as a polycrystal as discussed at length below.

Figure 6.6 is a resultant composite STEM-based EDS chemical images of our annealed PSC films. The chemical imaging provides a final snapshot of one of our reacted and annealed perovskite thin-films. This material is a planar view perspective of a thick textured perovskite film grown on compact titania and silicon nitride microchip.

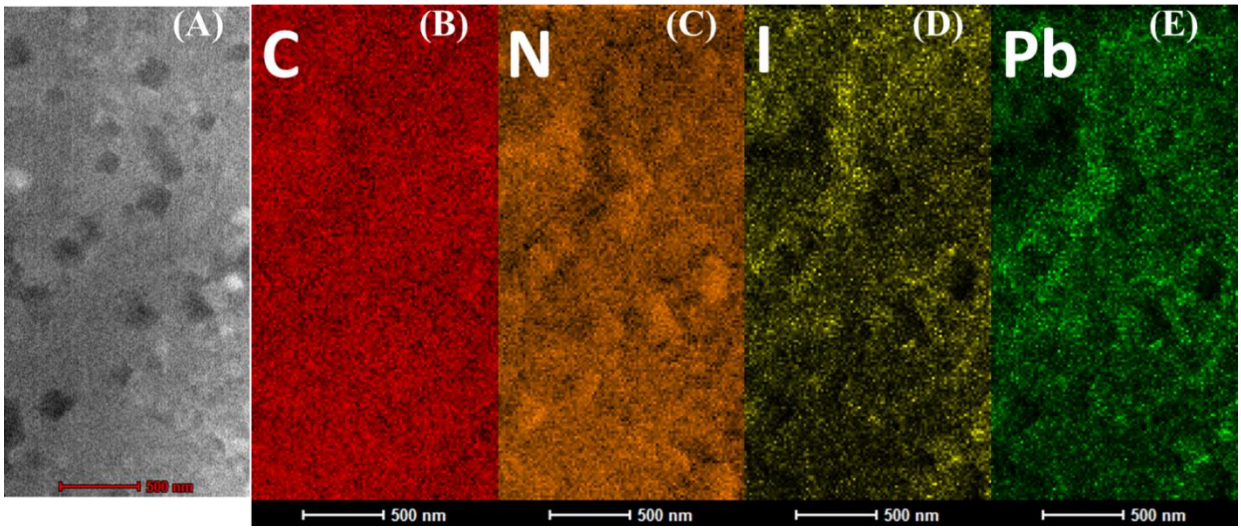

Figure 6. 6. a) Complementary, use of STEM-based EDS imaging and (b-d) chemical imaging provides a final snapshot of one of our annealed perovskite thin-films. From our post-chemical analyses we are able to qualitatively image b) C-*K*, c) N-*K*, d) I-*L*, and e) Pb-*M* x-ray lines, where quantitatively it is difficult to detect individual grains due to the mixed morphology of the as grown thick annealed perovskite layer, as mentioned previously.

The white and dark contrast corresponds to a final convolution of the deposited thick film texture (where HAADF is also sensitive to mass thickness variation) as well as the presence of perovskite and PbI_2. From our post-chemical analyses we are able to qualitatively image b) C-*K*, c) N-*K*, d) I-*L*, and e) Pb-*M* x-ray lines, where quantitatively it is difficult to detect individual grains due to the mixed morphology of the as grown thick annealed perovskite layer, as mentioned previously. Cross-sectional TEM imaging is also not possible.

6.3.3 Optimized device processing and performance

FA-based PSCs were fabricated and optimized based on the observed microstructural development from *in-situ* work. Figure 6.7 compares the effect of temperature on the photocurrent density-voltage (*JV*) curves of FA-based devices. Device measurements were conducted under 100 $mW.cm^{-2}$ (AM1.5) simulated solar irradiation. Figure 6.7a are the measured *JV* curves of FA-based devices prepared with annealing temperatures of 150 °C, 175 °C, 200 °C, and 225 °C, respectively.

In addition, the impedance measurements are shown in Figures 6.7b and 6.7c, as a function of the applied bias on the charge-carrier recombination resistance (R_{rec}). Based on the device measurements, we clearly observe a trend where the properties are optimized for the device annealed device at 175 °C. It clearly shows the highest efficiency, current, and voltage suggesting a uniform crystallization of the FA-based perovskite material confirmed in Figure 6.8 through *in-situ* high temperature XRD.

Upon increasing the temperature to 150°C the precursors react to form the $FAPbI_3$ perovskite phase. A phase separated PbI_2 phase is then observed at 175°C, which

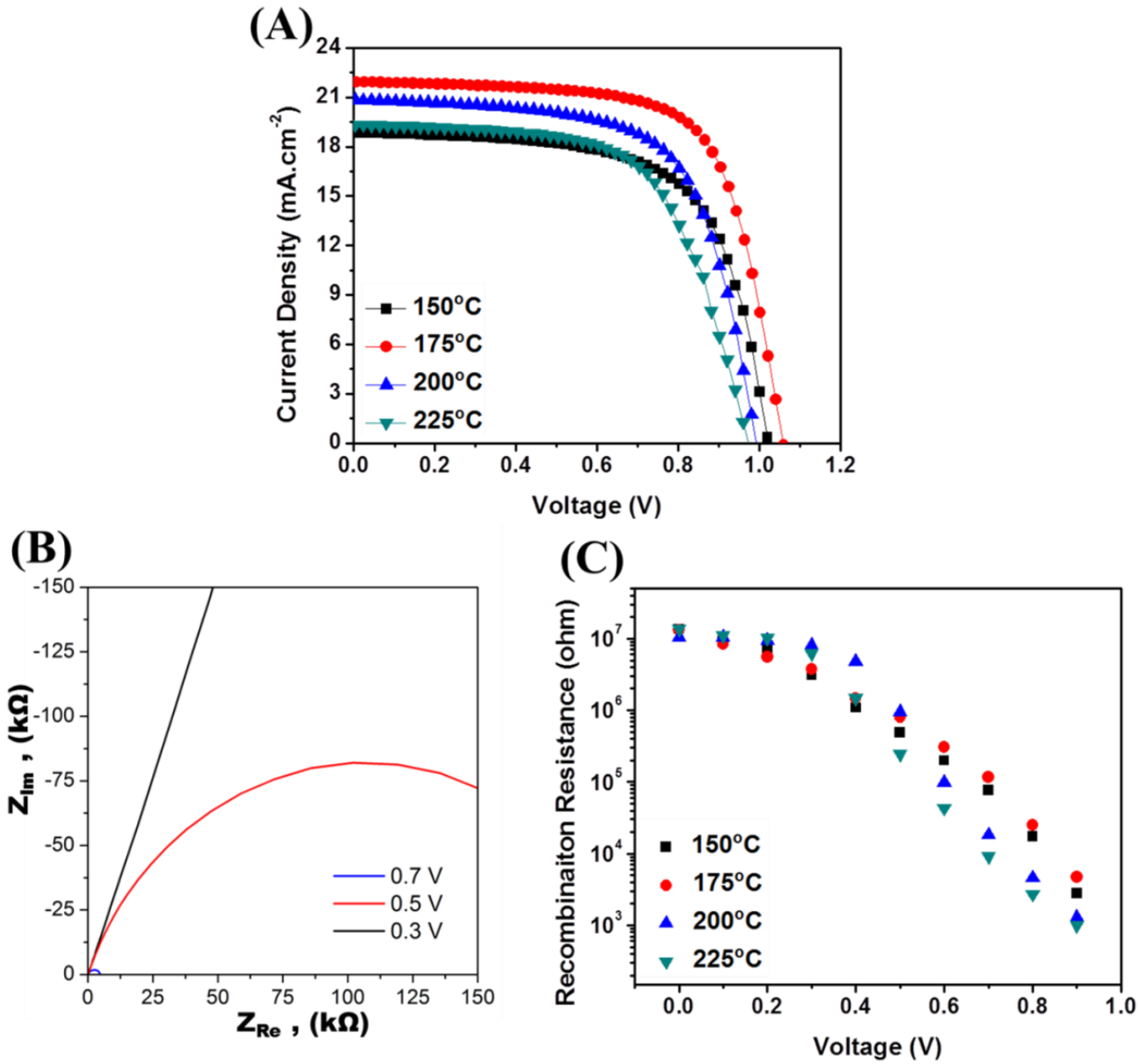

Figure 6. 7. a) Photocurrent density−voltage (*J*–*V*) characteristics of planar perovskite solar cells based on $FAPbI_3$ films prepared at various annealing temperature as indicated. Measurements were done under 100 mW/cm^2 AM 1.5 irradiation. b) Typical Nyquist plots of complex resistance at three different bias voltages. c) Effect of annealing temperature on the recombination resistance (R_{rec}) as a function of voltage for planar $FAPbI_3$ perovskite solar cells. c) Time measurements.

increases with increasing temperature. No evidence for the segregation of PbI_2 was observed at temperatures below 175°C.

XRD patterns were collected at temperatures of 25, 50, 150, 160, 175, 200 and 225°C. However for the purpose of simplicity, XRD patterns in Figure 6.8 are shown only for 25, 150, 175 and 200°C. The XRD data collected at 25°C shows peaks originating only from the precursor

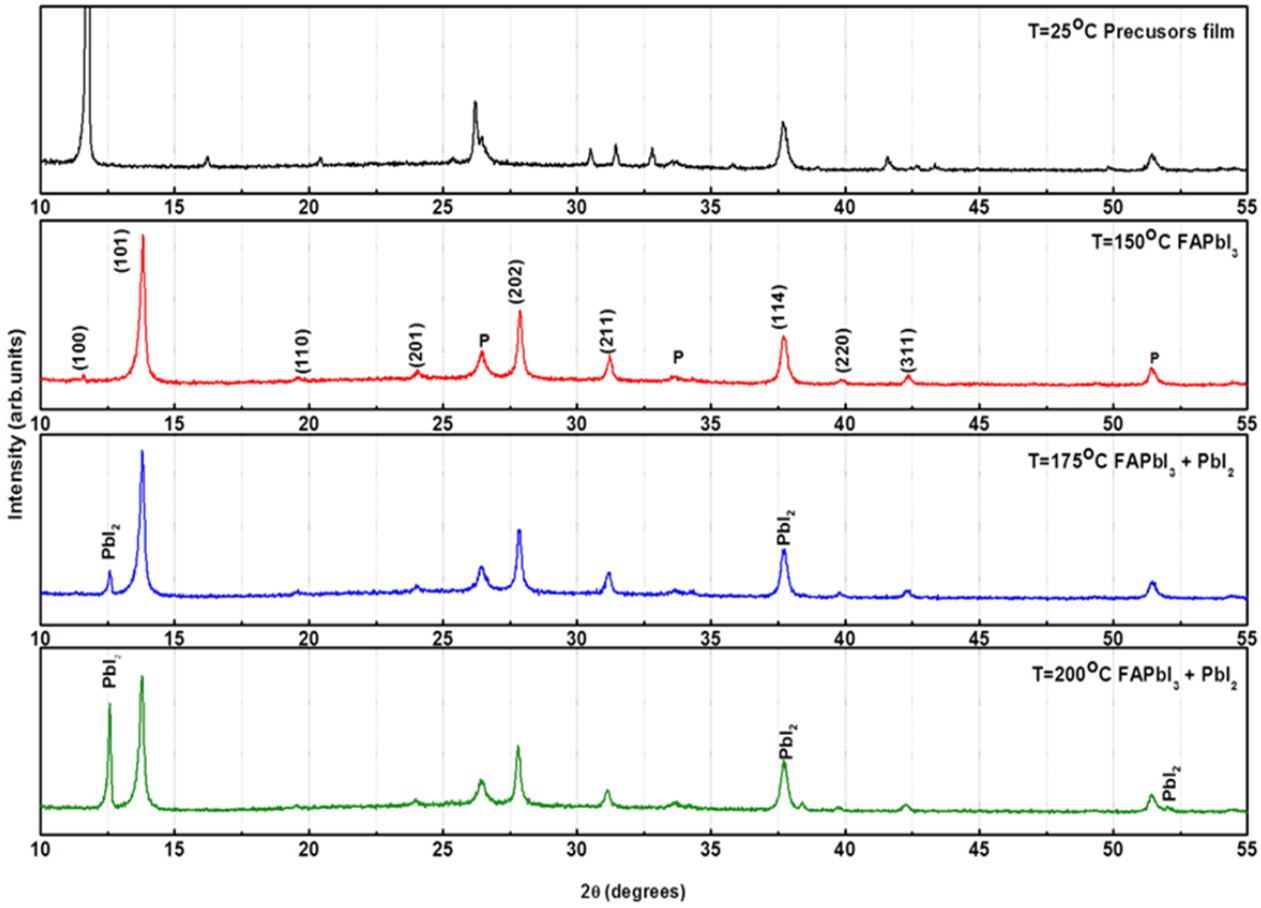

Figure 6. 8. *In-situ* grazing incidence high resolution XRD confirms the material microstructure for the generated devices as function of temperature starting with the precursor material. The perovskite peaks are labeled and the p label identifies precursor peaks at 26.45°, 33.64°, and 51.41°.

The PbI_2 phase can be indexed to a $CaCl_2$ type crystal structure belonging to the R-3m space group, while the $FAPbI_3$ phase could be indexed to a perovskite phase type crystal structure belonging to the P3m1 space group. Remnant precursor peaks labeled as P were also observed in the XRD pattern collected at 150 °C, similar to that observed in the TEM measurements.

6.4 Discussion

Our characterization of perovskite polycrystalline samples has revealed three interesting and surprising features. First, the preference for a 175˚C annealing temperature suggested in the literature is directly connected to the resultant polycrystalline microstructure, where a lead-containing species is concentrated at the boundaries and the $FAPbI_3$ perovskite is within the grain interiors. Second, with a change in temperature beyond 175ºC the lead-containing species is mobile leading to the eventual nucleation and growth of lead-containing particles that degrade the performance of the device. Third, the presence of elemental uniformity concentrated at grain boundaries is thereby the preferred device morphology. We suggest this is the preferred configuration to enhance grain-boundary mediated charge transport. Here, we will discuss the possible origins for these specific behaviors and their implications on overall cell performance, transport, and suggest a tailored growth strategy to improve upon the device efficiency associated FA-based PSCs.

6.4.1 Effect of temperature and annealing time

The $FAPbI_3$ films are comprised of various differently oriented domains, making up a polycrystalline material with varying grain sizes ranging from micron to nanometer size. One of

the key observations from the experimental studies is that we (i) show that superior processing of $FAPbI_3$ annealing at 175° C is directly related to the mobility and segregation of lead at boundaries. *JV* curves reveal that the device performances are strongly correlated and influenced by the annealing temperature; where a change of ± 10 ºC will impact both the short circuit current (J_{sc}) and open circuit voltage (V_{oc}) significantly. For a 10 minute standard annealing time, we measured the device characteristics as a function of temperature and report the results in Table 6.1. At 150°C, the *JV* curve shows that the device can reach efficiencies up to 12.6%. In correlation with the S/TEM observation, it is clear that PbI_2 and FAI are not yet fully crystallized into $FAPbI_3$, leading to a reduced efficiency due to an unfinished crystallization process. However, when the temperature is increased to 175°C, an improvement can be seen in the *JV* curves both from the J_{sc}, V_{oc} and Fill Factor (FF), leading to efficiencies of 16.1%. When the temperature is further increased to 200°C and 225°C, the degradation of the $FAPbI_3$ perovskite is initiated. This is strongly correlated to the microscopy, where PbI_2 start migrating toward the grain boundaries to form points of nucleation till subsequent particle growth and coarsening into individual nanometer precipitates. This degradation leads to loss in key device parameters: J_{sc}, V_{oc} and Fill Factor which directly impacts the efficiencies of the PSCs. Furthermore, in Figure 6.3 we highlighted a repeated temperature sequence, where the temperature was stepped in a repeated sequence (from 175 ºC, 200 ºC, 175 ºC, to 200 ºC) in Figure 6.2 and we observed PbI_2 precipitation in, along, and out of the boundaries. (ii) Based on this leading observation, we have shown a partially reversible process occurs that involves the exchange of lead at grain boundaries, further confirmed in Figure 6.5. Figure 6.4 further resolves formation and crystallization of the perovskite material from precursor material as well as the evolving presence of PbI_2 at temperatures using complementary SAED and *in-situ* XRD profiling.[34]

Impedance spectroscopy was further used to study the effect of temperature on the charge-carrier recombination resistance (R_{rec}) as a function of the applied bias in the relevant voltage range (0 to 1 V) using a standard impedance model for perovskite solar cells.[40] Figure 6.7b shows the typical Nyquist plots of complex resistance at three different bias voltages. The impedance spectra for all three bias voltages are dominated by a large semicircle at low frequencies.

Table 6. 1. Measured device characteristics as a function of annealing temperature for a fixed time interval of 10 minutes.

Temperature (°C)	**J_{sc} (mA/cm^2)**	**V_{oc} (V)**	**FF (%)**	**η (%)**
150°C	18.9	1.02	65	12.6
175°C	22.0	1.06	69	16.1
200°C	20.9	0.99	65	13.5
225°C	19.3	0.97	63	11.9

This large semicircle is often attributed to the charge recombination process within the perovskite solar cells. Figure 6.7c compares the effect of temperature on R_{rec} as a function of applied bias voltages. At each temperature, R_{rec} is strongly dependent on the applied bias voltage, following approximately an exponential decrease with voltage at the relatively high voltage range (>0.3 V). When compared at a constant bias voltage (e.g., 0.7 V), R_{rec} shows minimum change when the temperature is increased from 150°C to 175°C, and then decreases by 1–2

orders of magnitude with increasing temperature. This trend of R_{rec} change is consistent with the changes of the device characteristics (Figures 6.7a), which can be correlated to the mobility of PbI_2 in the $FAPbI_3$ grains. The existence of a PbI_2 nucleation site or particles at higher temperature likely creates defect sites causing the reduction in V_{oc} as well as FF, and departs from the uniform phase purity depicted in the *in-situ* high temperature XRD profile (Figure 6.8).

Table 6. 2. Measured device characteristics as function of annealing time. 175˚C was used as annealing temperature.

Time (min)	**J_{sc} (mA/cm^2)**	**V_{oc} (V)**	**FF (%)**	**η (%)**
5	20.9	1.02	59	12.5
10	22.0	1.06	69	16.1
20	21.2	1.02	51	11.0
40	16.6	0.98	50	8.1

With increasing annealing time, the efficiency of the device escalates to eventually a performance plateau. The trend in device efficiency is depicted in Table 6.2. Between 10 to 15 minutes of total annealing time, our highest efficiency devices are achieved, which is attributable to the formation of a highly crystalline and uniform $FAPbI_3$ layer in the device. Furthermore cycling annealing time and temperature below 175 °C, leads to presumably the enhancement of perovskite crystallinity and leading observation of the gradual redistribution of lead-containing species along the grain boundaries, leading to an increase in the efficiency of the device due to

the increasing the ability to mobilize generated charge carriers within the grain interiors. Beyond 175 °C in the one-step process, the efficiency drops presuming because the material dissociates and the lead evolves from the grain interiors.

6.4.2 Structure and chemistry of FA-based perovskites

Revealing the structure and chemistry associated with FA-based perovskites, we performed high-resolution microscopy and VEELS. Figure 6.5a is the collected STEM-based VEELS profiles collected across a planar grain boundary depicted in Figure 6.5b using gentle STEM at 60 kV. Based on the raw collected profiles we resolve the inhomogeneity associated within the material, containing FA-based perovskite and PbI_2. The corresponding subtracted VEELS profiles shown in Figure 6.5c-d reveal the presence H^+ and OH^- ions, with differences in the bonding nature associated with lead, and hydrogen between the grain interiors and interface. Several scenarios are possible for explaining the measureable differences in the bonding nature based on the collected VEELS line profiles. Lead is bonded in the grain interior with iodine in a tetrahedral configuration, leading to a final singlet bonding configuration, reported a singlet ionization peak. Compared to the boundary, the binding energy associated with lead is consequently shifted by nearly 2 eV and there is a measureable difference in the corresponding spectral character. A doublet peak associated with lead is also resolved at the boundary. Presumably, at the boundary there is a greater degree of hybridization and several possible bonding configurations, that lead to a potentially different orbital overlap with the lead 5*d* unoccupied states, as well as the effect of neighboring residual oxygen containing species. The relative peak positions in the valence spectrum are also potentially perturbed by the formation of other stable molecules (e.g., H-PbI_2), which leads to an increase in the binding energy due to

charge screening of the interface core. [41] Below the lead ionization thresholds (< 20 eV), we further verify the presence of PbI_2 localized at the boundary by measuring a local band gap of 2.36 eV in Figure 6.5d, in agreement with reported literature values. [42,43]

Concerning measuring hydrogen, the measureable differences in the VEELS spectral character is directly associated with several structural and electronic differences. The presence of charge screening at the interface compared to the grain interior is known to lead to measureable differences in the spectral shape as well differences in the bonding configuration between the interface and grain interior. Furthermore, in addition to the several bonding configurations associated with hydrogen there is also a given the migration of lead, presumably containing both hydrogenated and hydroxide surface terminating species, allowing for an even greater number of bonding states to be possible. We thereby attribute the variations in the VEEL spectra to these similar effects because, in addition to grain chemistry, the grain boundaries almost certainly contain hydrogenated lead, radical ions, and possibly other species (e.g., carbon compounds) that migrate into these open surfaces. These effects presumably all contribute to the broadening of the hydrogen feature measured at the boundary. Based on these series of defining results, we are able to provide a vital fundamental perspective into not only the atomic structure associated with annealed FA-based perovskite, but the local chemistry and electronic structure associated with the interior morphology of this complex polycrystalline inorganic-organic hybrid material.

6.4.3 Temperature dependent chemical equilibria

Given the above results, possible scenarios, and explanations, FA-based perovskite materials evolve with temperature not only due to the mobility of lead, but the role of hydrogen ions. The presence of a lead complex at $FAPbI_3$ grain boundaries results in an altered local

electronic environment at interfaces, which is otherwise distinct from the surrounding bulk material. At the grain boundaries there is direct evidence of the adsorption of hydrogen and lead, owing to the idea: (i) there is a direct exchange of H^+ and FA^+ cations under thermal cycling, leading to a degradation of the structural integrity of the trigonal perovskite framework, also suggested in similar studies.[16,44]

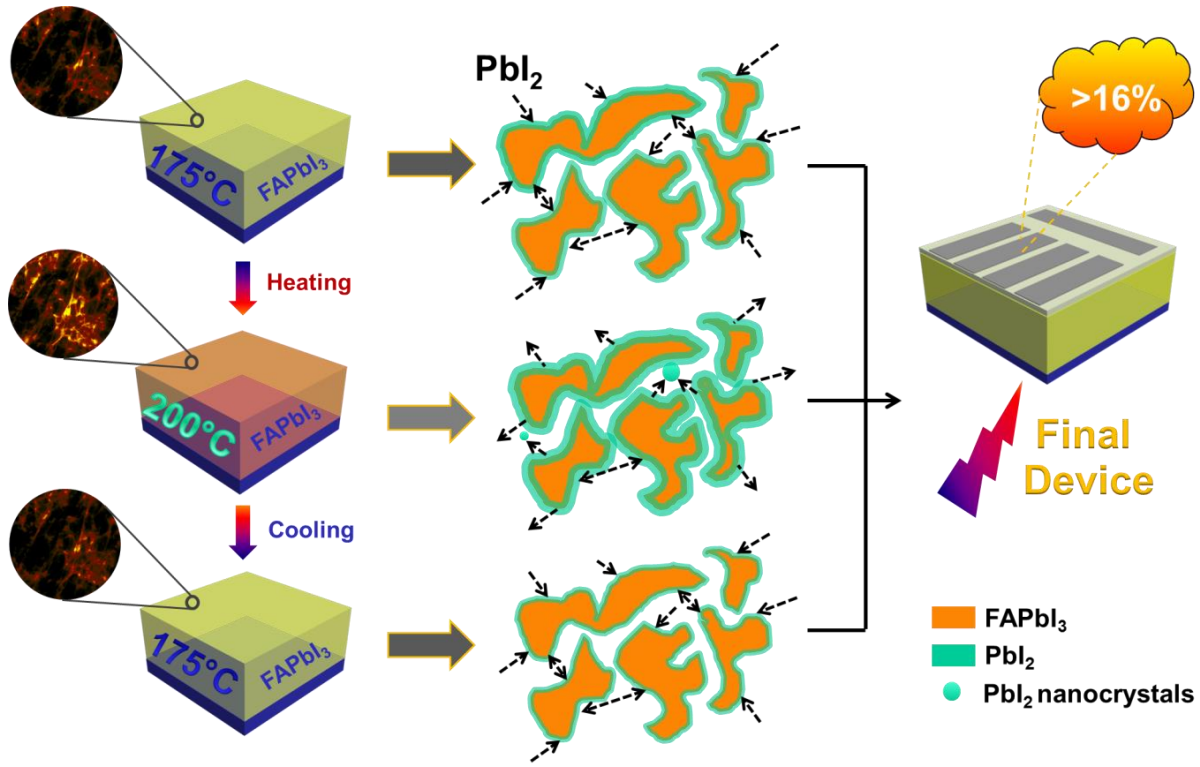

Figure 6. 9. In summary, the use of *in-situ* S/TEM provides the level of detail to resolve the detailed mobility of lead to and from PSCs grain boundaries that ultimately degrades the measured performance associated with these FAI-based PSC photovoltaics.

In particular, the degree of intermixing between the PbI_2 and FA depends significantly on the processing conditions. (ii) upon heating, $FAPbI_3$ can dissociate into FA^+, HI and PbI_2 or its

ionic version (PbI_3^-, PbI_4^-, PbI_6^-), where ionic lead iodide can be hydrolyzed, reacts with neighboring site-specific residual O to form PbI(OH) crystals. However PbI(OH) crystals cannot undergo a reversible crystallization process, leading to a permanent degradation of $FAPbI_3$ domain interior. (iii) The reaction of PbI_2 with HI may also lead to the formation of $HPbI_3$ precursor material (iv) upon cooling, via the FA cation reacting with PbI_2 species ($HPbI_3$, PbI_3^-, PbI_4^-, PbI_6^-) and recrystallizing the $FAPbI_3$ perovskite. In line with these ideas we have summarized in Figure 6.9, the preferred pathway to a higher efficiency FA-based PSC through sequential annealing leading to the eventual redistribution of lead and hydrogen for FA-based perovskites. In particular, the degree of intermixing between the lead iodide and FA depends significantly on the processing conditions. In line with this idea and the main conclusion of our study is the influence of temperature on measured device properties is directly linked with the microstructure of FA-based PSCs, where the distribution of chemical species importantly affects the final measured device efficiency.

6.5 Conclusions

A systematic experimental investigation of the structure, chemistry, and electro-optical properties of polycrystalline $FAPbI_3$ PSCs was reported. The goal was to understand the complex relationship between temperature, segregation, valence structure, and carrier kinetics in an otherwise complex FA-based polycrystalline PSCs photovoltaic following external heating by combining the latest advances in *in-situ* materials characterization.

Our results demonstrate that with sufficient heating and annealing temperature, we can directly influence the fundamental microstructure and chemistry. The morphology and formation process of perovskite films fabricated from FAI/PbI_2 precursors on compact titania with *in-situ*

S/TEM show that the superior processing of $FAPbI_3$ annealing at 175° C is directly related to the mobility and segregation of lead compounds and related hydrogen species at crucial grain boundaries.

The second important observation is that we can adjust the distribution of lead decorating the grain boundary interiors and demonstrate this is as a partially reversible process. We have shown at temperature that a partially reversible process occurs involving the exchange of a lead containing species at the grain boundaries, which are only partially reversible if they become nucleated and coarsened into stable precipitates. In line with these observation is direct evidence of the adsorption of hydrogen at these specific interface regions, owing to the idea there is direct ionic exchange of presumably OH^- , H^+ , and FA^+ ions under thermal cycling, leading to the evolution and formation of the PSC framework.

Based on the culmination of our cross-scale and cross-platform results, we conclude our results to support the idea that providing direct snapshots into the mobility of elements making up PSCs offers the necessary level of materials insight to directly improve upon the future of PSCs to meet future higher efficiency goals. Taken together, this coupled fundamental and device study demonstrates the necessary understanding of $FAPbI_3$ crystallization formation mechanisms and provides vital links between measured microstructure and device performance as function of final annealing temperature to improve upon the current state of FA-based PSCs.

6.6 References

(1) Sawin, J. L.; Sverrisson, F. *Renewable 2014 Global Status Report*, 2014.

(2) Green, M. A.; Ho-Baillie, A.; Snaith, H. J. *Nat Photon* **2014**, *8*, 506.

(3) Jeon, N. J.; Noh, J. H.; Yang, W. S.; Kim, Y. C.; Ryu, S.; Seo, J.; Seok, S. I. *Nature* **2015**, *517*, 476.

(4) Gratzel, M. *Nat Mater* **2014**, *13*, 838.

(5) Pellet, N.; Gao, P.; Gregori, G.; Yang, T.-Y.; Nazeeruddin, M. K.; Maier, J.; Grätzel, M. *Angewandte Chemie International Edition* **2014**, *53*, 3151.

(6) Boix, P. P.; Nonomura, K.; Mathews, N.; Mhaisalkar, S. G. *Materials Today* **2014**, *17*, 16.

(7) Mitzi, D. B. In *Progress in Inorganic Chemistry*; John Wiley & Sons, Inc.: 2007, p 1.

(8) Eperon, G. E.; Stranks, S. D.; Menelaou, C.; Johnston, M. B.; Herz, L. M.; Snaith, H. J. *Energy & Environmental Science* **2014**, *7*, 982.

(9) Burschka, J.; Pellet, N.; Moon, S.-J.; Humphry-Baker, R.; Gao, P.; Nazeeruddin, M. K.; Gratzel, M. *Nature* **2013**, *499*, 316.

(10) Zhao, Y.; Zhu, K. *Journal of the American Chemical Society* **2014**, *136*, 12241.

(11) Zhao, Y.; Zhu, K. *The Journal of Physical Chemistry C* **2014**, *118*, 9412.

(12) Mei, A.; Li, X.; Liu, L.; Ku, Z.; Liu, T.; Rong, Y.; Xu, M.; Hu, M.; Chen, J.; Yang, Y.; Grätzel, M.; Han, H. *Science* **2014**, *345*, 295.

(13) Niu, G.; Li, W.; Meng, F.; Wang, L.; Dong, H.; Qiu, Y. *Journal of Materials Chemistry A* **2014**, *2*, 705.

(14) You, J.; Yang, Y.; Hong, Z.; Song, T.-B.; Meng, L.; Liu, Y.; Jiang, C.; Zhou, H.; Chang, W.-H.; Li, G.; Yang, Y. *Applied Physics Letters* **2014**, *105*, 183902.

(15) Christians, J. A.; Miranda Herrera, P. A.; Kamat, P. V. *Journal of the American Chemical Society* **2015**, *137*, 1530.

(16) Wang, F.; Yu, H.; Xu, H.; Zhao, N. *Advanced Functional Materials* **2015**, *25*, 1120.

(17) Hoke, E. T.; Slotcavage, D. J.; Dohner, E. R.; Bowring, A. R.; Karunadasa, H. I.; McGehee, M. D. *Chemical Science* **2015**, *6*, 613.

(18) Niu, G.; Guo, X.; Wang, L. *Journal of Materials Chemistry A* **2015**.

(19) Aharon, S.; Dymshits, A.; Rotem, A.; Etgar, L. *Journal of Materials Chemistry A* **2015**.

(20) Dualeh, A.; Gao, P.; Seok, S. I.; Nazeeruddin, M. K.; Grätzel, M. *Chemistry of Materials* **2014**, *26*, 6160.

(21) Wozny, S.; Yang, M.; Nardes, A. M.; Mercado, C. C.; Ferrere, S.; Reese, M. O.; Zhou, W.; Zhu, K. *Chemistry of Materials* **2015**.

(22) Habisreutinger, S. N.; Leijtens, T.; Eperon, G. E.; Stranks, S. D.; Nicholas, R. J.; Snaith, H. J. *Nano Letters* **2014**, *14*, 5561.

(23) Ramos, F. J.; Cortes, D.; Aguirre, A.; Castano, F. J.; Ahmad, S. In *Photovoltaic Specialist Conference (PVSC), 2014 IEEE 40th* 2014, p 2584.

(24) Pisoni, A.; Jaćimović, J.; Barišić, O. S.; Spina, M.; Gaál, R.; Forró, L.; Horváth, E. *The Journal of Physical Chemistry Letters* **2014**, *5*, 2488.

(25) Ito, S.; Tanaka, S.; Manabe, K.; Nishino, H. *The Journal of Physical Chemistry C* **2014**, *118*, 16995.

(26) Li, W.; Dong, H.; Wang, L.; Li, N.; Guo, X.; Li, J.; Qiu, Y. *Journal of Materials Chemistry A* **2014**, *2*, 13587.

(27) Chander, N.; Khan, A. F.; Chandrasekhar, P. S.; Thouti, E.; Swami, S. K.; Dutta, V.; Komarala, V. K. *Applied Physics Letters* **2014**, *105*, 033904.

(28) Hansen, T. W.; Wagner, J. B.; Hansen, P. L.; Dahl, S.; Topsøe, H.; Jacobsen, C. J. H. *Science* **2001**, *294*, 1508.

(29) Alsem, D.; Salmon, N. J.; Unocic, R. R.; Veith, G. M.; More, K. L. *Microscopy and Microanalysis* **2012**, *18*, 1158.

(30) Egerton, R. F.; Takeuchi, M. *Applied Physics Letters* **1999**, *75*, 1884.

(31) Krivanek, O. L.; Chisholm, M. F.; Nicolosi, V.; Pennycook, T. J.; Corbin, G. J.; Dellby, N.; Murfitt, M. F.; Own, C. S.; Szilagyi, Z. S.; Oxley, M. P.; Pantelides, S. T.; Pennycook, S. J. *Nature* **2010**, *464*, 571.

(32) Zobelli, A.; Gloter, A.; Ewels, C. P.; Seifert, G.; Colliex, C. *Physical Review B* **2007**, *75*, 245402.

(33) Aguiar, J. A.; Reed, B. W.; Ramasse, Q. M.; Erni, R.; Browning, N. D. *Ultramicroscopy* **2013**, *124*, 130

(34) Gammer, C.; Mangler, C.; Rentenberger, C.; Karnthaler, H. P. *Scripta Materialia* **2010**, *63*, 312.

(35) Leapman, R. D.; Sun, S. *Ultramicroscopy* **1995**, *59*, 71.

(36) Yin, J. S.; Wang, Z. L. *Applied Physics Letters* **1999**, *74*, 2629.

(37) Hojou, K.; Furuno, S.; Kushita, K. N.; Sasajima, N.; Izui, K. *Nuclear Instruments and Methods in Physics Research Section B: Beam Interactions with Materials and Atoms* **1998**, *141*, 148.

(38) Bradley, J. P.; Ishii, H. A.; Gillis-Davis, J. J.; Ciston, J.; Nielsen, M. H.; Bechtel, H. A.; Martin, M. C. *Proceedings of the National Academy of Sciences* **2014**, *111*, 1732.

(39) Garcia de Abajo, F. J.; Howie, A. *Inst. Phys. Conf. Ser.* **1999**, *161*.

(40) Juarez-Perez, E. J.; Wuβler, M.; Fabregat-Santiago, F.; Lakus-Wollny, K.; Mankel, E.; Mayer, T.; Jaegermann, W.; Mora-Sero, I. *The Journal of Physical Chemistry Letters* **2014**, *5*, 680.

(41) Pedesseau, L.; Even, J.; Katan, C.; Raouafi, F.; Wei, Y.; Deleporte, E.; Jancu, J. M. *Thin Solid Films* **2013**, *541*, 9.

(42) Bordas, J.; Robertson, J.; Jakobsson, A. *Journal of Physics C: Solid State Physics* **1978**, *11*, 2607.

(43) Scrocco, M. *Journal of Electron Spectroscopy and Related Phenomena* **1989**, *48*, 363.

(44) Jeon, N. J.; Noh, J. H.; Kim, Y. C.; Yang, W. S.; Ryu, S.; Seok, S. I. *Nat Mater* **2014**, *13*, 897.

Chapter 7 Concluding Remarks

The energy crisis of the 21st century, accentuated by the greenhouse effect, is leading to a focus on alternative energies sources to fulfil the perpetual demand for energy. Renewable energies, which account so far for 20 % of the worldwide energy production, are viable solutions compare to polluting fossil fuel. Among them, solar cells offer the promises of clean, abundant and low cost energy production. Currently, the development and implementation of new photovoltaic (PV) materials continues to be intertwined with major technological achievements in energy and semiconductor device fabrication. Today's photovoltaics and portable electronic devices have similar requirements for energy: where they must be highly efficient (> 15 %), have a large capacity for long-term manufacturing, extend for long lifetimes, and be environmentally friendly. The current commercial solar cell technologies (1st and 2nd generation), despite high power conversion efficiencies and long term stability, suffer from precursor materials scarcity and expensive manufacturing processes. The emerging materials studied in this thesis (CZTS and Perovskite) may provide a viable alternative to current market technology.

It was demonstrated that CZTS absorber materials can be synthesized by vacuum (PLD) and non-vacuum techniques (hot injection synthesis), with different morphologies (bulk, nanocrystals, etc.). The nanostructures were integrated in workable nanostructured and dye-sensitized solar cells, making CZTS suitable for achieving low cost and environmentally friendly photovoltaic devices.

On another hand, perovskite-based solar cells are attractive photovoltaic materials due to their impressive properties as light harvesters, their subsequent high device efficiencies (16.6%), and their low-cost industrially scalable process. However, these new materials are extremely

sensitive to their processing environment, which can tremendously impact the final device power conversion efficiency. Additionally, the long term stability of these new perovskite solar cells is hindered by a rapid degradation of the compound under atmospheric pressure in the presence of air. The *in-situ* scanning transmission electron microscope study on the crystallization and degradation of the compound provided a deeper understanding of the fundamental microstructure, and showed a possible degradation mechanism for formamidinium lead triiodide solar cells in the presence of oxygen. Overall, this work gave us a deeper understanding of emerging absorber materials, namely perovskite. Ultimately, we conclude that providing fundamental study of our absorber materials trough *in-situ* techniques offers the necessary level of materials insight to directly improve upon the device fabrication process to meet future higher efficiency goals.

Vita

Sarah Wozny was born in Brive-La-Gaillarde, France. In 2007, she was admitted at the University of Poitiers, Poitiers, France, for a Diplôme Universitaire de Technologie in Chemistry. She graduated in 2009, and finished her undergraduate studies at Heriot-Watt University, Edinburgh, Scotland, where she obtained a Bachelor of Science in Chemistry with Materials. In 2010, she joined the Chemistry graduate program and the Advanced Materials Research Institute (AMRI) at the University of New Orleans, New Orleans, LA, USA. She pursued research in Dr. Weilie Zhou's group and obtained a Master's degree in Materials Chemistry in spring 2014. During her time at the University of New Orleans, Sarah worked as a visiting scholar at the South-East University-FEI-Nano Pico center, Nanjing, China and at the National Renewable Energy Laboratory, Golden, CO, USA. She is pursuing a Ph.D. in Materials Chemistry, with a focus on photovoltaic research.